FEL STUDIES OF COMPLEX METAL NANOPARTICLES AND THEIR STRUCTURAL DYNAMICS

Dissertation
zur Erlangung des Doktorgrades
an der Fakultät für Mathematik, Informatik und Naturwissenschaften
Fachbereich Physik
der Universitat Hamburg

vorgelegt von
SHARATH SASIKUMAR

Hamburg
2025

Gutachter/innen der Dissertation:	Dr. Michael Martins
	Dr. Tommaso Mazza
Zusammensetzung der Prüfungskommission:	Prof. Dr. Daniela Pfannkuche
	Dr. Tommaso Mazza
	Prof. Paolo Piseri
	Dr. Michael Martins
	Prof. Dr. Markus Ilchen
Vorsitzende/r der Prüfungskommission:	Prof. Dr. Daniela Pfannkuche
Datum der Disputation:	10.02.2026
Vorsitzender des Fach-Promotionsausschusses PHYSIK:	Prof. Dr. Johannes Haller
Leiter des Fachbereichs PHYSIK:	Prof. Dr. Markus Drescher
Dekan der Fakultät MIN:	Prof. Dr.-Ing. Norbert Ritter

Dedicated to Ashwathi, the love of my life.

ABSTRACT

Clusters are of great interest in studying material properties, occupying the phenomenological regime between the quantized behavior of atoms and molecules and the properties derived in the classical limit from those of bulk matter. As the chemical behavior of clusters is influenced primarily by their morphological properties and surrounding medium, understanding their native properties requires their study in the gas phase. This doctoral thesis describes the findings of multiple experiments designed to characterize the structural and morphological properties of gas-phase copper clusters produced by a method based on inert-gas condensation following pulsed-vaporization, and to study their dynamic evolution.

For the characterization of cluster properties, a custom spectrometer capable of mass spectrometry and momentum imaging of high-momentum ions, as well as Velocity Map Imaging spectroscopy of photoelectrons, was first designed and commissioned. An experimental setup was then designed with this spectrometer and a pulsed laser to study the photo-ionization and photofragmentation of complex clusters in the gas phase. The characterization data were interpreted using physical models, allowing for the retrieval of parameters to describe the morphology and internal structure of the clusters. The morphology of the same clusters was also studied via Small Angle X-Ray Scattering (SAXS) with a soft X-ray FEL at the Small Quantum Systems Instrument at the European XFEL. The clusters were found to be polydisperse agglomerates with fractal properties correlated to their growth times and conditions.

The evolution of these structural and morphological cluster properties was studied via time-resolved ion spectrometry and SAXS experiments over a hundred picoseconds after irradiation with an IR pump laser. Pump irradiation was found to trigger a reconfiguration of the clusters into a dense structure similar to melting, using the original methodology applied, which provides

valuable information about the pathways of this evolution.

ZUSAMMENFASSUNG

Cluster sind von großem Interesse für das Studium von Materialeigenschaften, da sie das phänomenologische Regime zwischen dem quantisierten Verhalten von Atomen und Molekülen und denjenigen Eigenschaften einnehmen, die sich im klassischen Grenzfall aus denen von Massivmaterial ableiten. Da das chemische Verhalten von Clustern in erster Linie durch ihre morphologischen Eigenschaften und ihr umgebendes Medium beeinflusst wird, erfordert das Verständnis ihrer intrinsischen Eigenschaften deren Untersuchung in der Gasphase. Diese Dissertation beschreibt die Ergebnisse mehrerer Experimente, die darauf ausgelegt sind, die strukturellen und morphologischen Eigenschaften von Kupferclustern in der Gasphase zu charakterisieren, die durch ein Verfahren erzeugt werden, das auf Inertgas-Kondensation nach gepulster Verdampfung basiert, sowie deren dynamische Entwicklung zu untersuchen.

Für die Charakterisierung der Clustereigenschaften wurde zunächst ein spezielles Spektrometer entwickelt und in Betrieb genommen, das Massenspektrometrie und Impulsabbildung von Ionen mit hohem Impuls sowie Velocity-Map-Imaging-Spektroskopie von Photoelektronen ermöglicht. Anschließend wurde ein experimenteller Aufbau mit diesem Spektrometer und einem gepulsten Laser entwickelt, um die Photoionisation und Photofragmentation komplexer Cluster in der Gasphase zu untersuchen. Die Charakterisierungsdaten wurden mithilfe physikalischer Modelle interpretiert, wodurch Parameter zur Beschreibung der Morphologie und der inneren Struktur der Cluster gewonnen werden konnten. Die Morphologie derselben Cluster wurde außerdem mittels Small-Angle X-Ray Scattering (SAXS) mit einem weichen Röntgen-FEL am Small Quantum Systems Instrument des European XFEL untersucht. Es wurde festgestellt, dass die Cluster polydisperse Agglomerate mit fraktalen Eigenschaften sind, die mit ihren Wachstumszeiten und -bedingungen korrelieren.

Die Entwicklung dieser strukturellen und morphologischen Clustereigenschaften wurde über mehrere hundert Pikosekunden nach

der Bestrahlung mit einem IR-Pumplaser mittels zeitaufgelöster Ionspektrometrie und SAXS-Experimenten untersucht. Es zeigte sich, dass die Pump-Bestrahlung eine Rekonfiguration der Cluster zu einer dichten, dem Schmelzen ähnlichen Struktur auslöst, wobei die angewandte ursprüngliche Methodik wertvolle Informationen über die Entwicklungspfade dieses Prozesses liefert.

CONTENTS

LIST OF FIGURES

1 INTRODUCTION

1.1 NANOSCALE COMPLEX MORPHOLOGY

Clusters are defined as aggregates consisting of 3 to 10^7 atoms or molecules [1]. They may possess either a chemically uniform or mixed composition, with sizes extending up to several tens of nanometers.

Clusters exhibit a wide diversity in size, chemical composition, and morphology. Their study is therefore essential for understanding the evolution of material properties from individual atoms to bulk matter. In metallic clusters, for instance, the electronic structure transitions from discrete, molecule-like orbitals in small clusters to continuous, band-like states as the cluster size approaches that of bulk material [2].

Cluster-based materials find applications across multiple fields of nanotechnology, including catalysis, energy conversion and storage, and biocompatible coatings for medical applications [3–5]. The capability to synthesize novel materials through a bottom-up, hierarchical approach makes clusters highly versatile nanoparticles.

Metal cluster synthesis mainly follows two methodologies. One is chemical synthesis, wherein the clusters are formed and stabilized as a result of interaction with a medium or a substrate [6]. The other is gas-phase vapor condensation, wherein cluster formation occurs in a chemically inert environment [7, 8].

The nature of chemical synthesis makes it extremely difficult to isolate the clusters from the synthesis media or substrate. This makes it unsuitable for studying the properties of native clusters. Gas-phase synthesis, despite its relative complexity, has the distinct advantage of producing isolated clusters. The clusters pro-

duced by gas-phase synthesis are thus ideal samples for characterization and analysis of native cluster properties.

This thesis presents the design, implementation, and results of experiments aimed at characterizing the structure and morphology of isolated **copper** clusters produced via gas-phase synthesis using a **Pulsed Microplasma Cluster Source (PMCS)**. It further investigates the evolution of these cluster properties following energy transfer over extended timescales (on the order of picoseconds), which can provide insights into the underlying physics governing these systems.

The relatively low atomic number of copper makes it well-suited for computational modeling and simulation [9–11], while still offering a high X-ray scattering cross section [12]. Moreover, copper nanoparticles possess a wide range of practical applications, including use in biosensors and electrochemical sensors [13], broad-spectrum antibacterial agents [14], and corrosion-resistant coatings [15]. Their localized surface plasmon resonances [16] enhance optical responses, producing plasmonic bands within the visible spectrum. Additionally, copper's electrical conductivity makes it an ideal material for cluster synthesis using the PMCS, the principles and operation of which are detailed in the following section.

1.2 PULSED MICROPLASMA CLUSTER SOURCE

For gas-phase synthesis of clusters, the required process is threefold. Firstly, the introduction or production of the precursor vapor into the gas phase, followed by the condensation of this vapors into clusters, and finally their extraction.

For molecular or rare gas clusters, once the cluster precursor is introduced into the gas phase, the adiabatic expansion through a nozzle into vacuum satisfies the remaining steps of vapor condensation and extraction [17].

For refractory materials, such as metals, the vapor can be obtained through the non-thermal vaporization of a solid target. Va-

porization is commonly achieved by using various techniques: using an intense laser pulse or arc discharge [18], by magnetron [19], or, as in the case of this thesis, pulsed sputtering [8] in the PMCS.

The PMCS consists of an insulating ceramic body in a vacuum, which contains a thermalization cavity holding a rod of the target material. The rod is connected to a pulsed high voltage power supply (with negative polarity and high current). The back of the cavity is attached to a metal nozzle, behind which is affixed a pulsed solenoid valve, connected to a high-pressure gas reservoir. The metal nozzle is connected to the neutral line of the high voltage power supply, held at ground. The target rod and metal nozzle of the pulsed valve, therefore, act as the cathode and the anode, respectively. The cavity opens towards an exit nozzle connected to an aerodynamic lens system.(Figure 1.1).

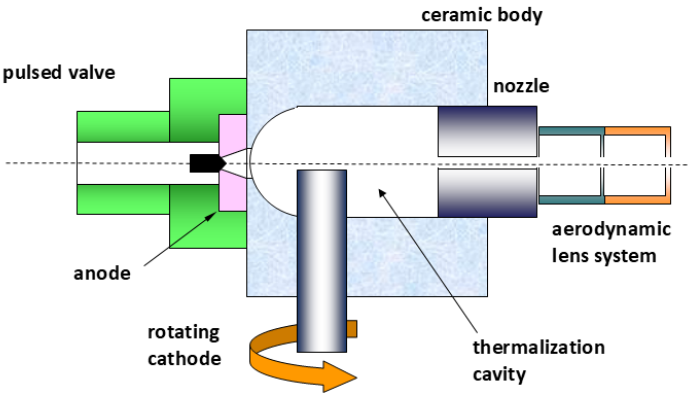

Figure 1.1: Schematic of the Pulsed Microplasma Cluster Source (PMCS). [8]

Four processes characterize cluster synthesis in the PMCS:

- The pulsed valve periodically injects gas from the high-pressure reservoir into the cavity, creating a strong jet directed against the target rod. (Figure 1.2a)
- After a short delay determined by the injected gas dynamics, a brief ($\approx 50\,\mu s$) pulse of high voltage is applied between the target rod (cathode) and the anode plate. Due to the high density of gas in a small region of the cathode surface, the applied voltage causes an intense discharge that vaporizes

the rod through ion bombardment, creating a microplasma of the target material (Figure 1.2b).

- The localized nature of the discharge facilitates a rapid quenching of the microplasma, favoring effective cluster nucleation close to the cathode, in a bath of the injected gas. (Figure 1.2c)
- After formation, clusters are extracted from the cavity by the drift of the injected gas, acting as a carrier for the suspended clusters (Figure 1.2d). The extracted mixture undergoes supersonic expansion, meaning that no further growth of clusters occurs after their extraction.

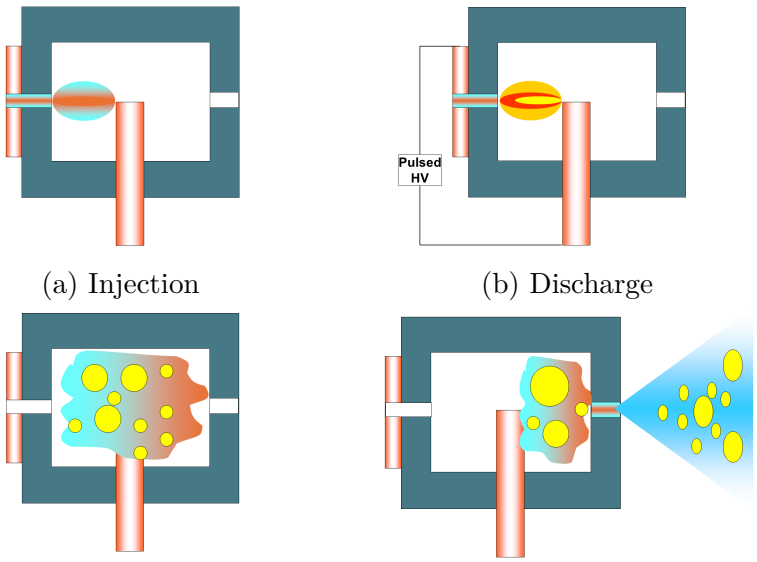

(a) Injection (b) Discharge

(c) Nucleation (d) Extraction

Figure 1.2: Cluster formation and extraction during PMCS operation.

By exploiting inertial separation in rarefied gas flows, the aerodynamic lens system forming the exit nozzle of the PMCS focuses clusters to the central part of the free jet at the origin of the supersonic beam. This aerodynamic focusing maximizes cluster extraction from the source cavity. The system consists of a series of thin plates mounted in cylindrical stages [20, 21]. Each plate has a central aperture, with the system terminating at a skimmer located at the sonic plane of the final supersonic expansion.

To effectively characterize clusters produced by the PMCS, the source must operate consistently and reproducibly on a pulse-to-

pulse basis. This consistency is strongly influenced by two factors. The first is the stability of the gas injection and the pulse-rise time (on a scale of 10 µs). The second is the uniformity of the discharge, which is primarily influenced by the ablated surface. The stability of gas injection is achieved through the control of pulsed valve temperature using liquid cooling. The uniformity of the discharge is achieved with the continuous rotation of the cathode via an external motor, creating homogeneous consumption of the cathode along its lateral surface.

Based on the long timescale of cluster extraction (≈ 100 ms) compared to nucleation, the clusters produced by the PMCS can undergo several additional processes. Some of these processes include: additional growth and agglomeration; drift towards walls of the discharge cavity; inertial separation effects due to gas flow. Each of these processes can affect the structure, morphology, and yield of the extracted clusters at different times [22]. Since cluster formation occurs entirely within the injected gas volume, the composition of the injected gas can also influence cluster formation. Injecting high-purity inert gases, such as He or Ar, leads to the formation of clusters with a chemical composition identical to that of the target rod. Doping the inert gas with reactive species can alter the chemical composition of the synthesized clusters [23, 24].

The majority of cluster differentiation occurs in the condensation period between cluster nucleation and extraction. This growth process is primarily influenced by the thermal environment of cluster formation. This depends on the delay between discharge and the eventual extraction of the cluster. This time spent by the clusters in the thermalization cavity before extraction is henceforth referred to as their **Residence Time**. The maximum resolvable residence time of clusters extracted from the PMCS is defined by its **duty cycle**, i.e., the time between successive pulses of the gas valve. Clusters with similar residence times will have similar growth histories and thus exhibit similar properties.

Varying the operating conditions of the PMCS, such as the calibration of the pulsed valve, its repetition rate, and opening time, as well as the delay between gas injection and discharge,

and the configuration of the aerodynamic lenses, can affect the growth and properties of the extracted clusters. In this thesis, the PMCS is used to produce copper clusters in the gas phase with fixed operating parameters for all experiments. This fixed operation mode was chosen to obtain maximum consistency in cluster measurements across all the experiments described in this thesis.

1.2.1 *PMCS Operation Parameters*

The PMCS is attached to an expansion chamber held at high vacuum (2×10^{-7} mbar). The pulsed valve is connected to a reservoir of pure Argon (Ar) maintained at a pressure of 60 bar. A rod of pure Copper (Cu) is inserted into the PMCS cavity as the cathode (target material). The tip of the cathode is aligned to the gas injection nozzle. This ensures that the discharge occurs along the cathode tip, facilitating longer source operation before maintenance is required.

The pulsed valve is operated with an opening time of 200 µs. The high voltage discharge occurs after a delay of 430 µs from injection, with a duration of 60 µs.

The PMCS is triggered either internally and externally for different experiments. In the internal trigger mode, the source is operated at a frequency of 3 Hz, with a duty cycle period of 333 ms. When externally triggered, the source is operated at a frequency of 3.33 Hz, with a duty cycle period of 300 ms. As the differences between the two trigger modes are minimal, the clusters formed in both cases are comparable.

The extracted clusters, after formation, are focused via a 4-stage aerodynamic lens system housed in the expansion chamber. The lens system consists of an entry nozzle and 4 apertures of 1 mm each spaced 90 mm apart, making the whole system 360 mm. This stage is much longer than the focusing stages used in previous experiments [25].

1.3 CHARACTERIZATION TECHNIQUES

The intrinsic properties of PMCS operation create a pulsed supersonic jet of clusters having a broad range of sizes and structural features. As these clusters undergo further growth after nucleation, they are agglomerates of smaller **primary particles**.

The primary particles are small clusters of the target material (copper) formed during the nucleation step, by the quenching of the microplasma. Due to this, primary particles are expected to be dense spheroids which will maintain their structure during agglomeration.

Clusters produced by the PMCS, while decoupled from any medium, are non-trivial to characterize due to their high dilution and diverse growth histories. Poly-disperse systems like those of gas-phase clusters require unified parameters to describe their morphologies. This thesis describes the morphology of the clusters using their fractal dimension D_f [26] and their structural properties using the overlap factor C_{ov} [27] between primary particles in the cluster.

The fractal dimension D_f of an aggregate (such as a cluster) is a non-integer exponent that characterizes how the mass of the aggregate, or the number of primary particles in it, scales with its size [28]. D_f is thus indicative of the morphology of the clusters as a whole.

The overlap factor C_{ov} of two particles that have undergone an inelastic collision (such as the primary particles during cluster growth) gives the degree of overlap (sintering) between them. It can be used to retrieve the normal contact forces between the two particles [29]. Characterization of C_{ov} thus reveals information about the internal structure of the clusters with different growth conditions.

The properties of PMCS-generated clusters depend strongly on their residence time, and repeats with each new cycle. Therefore, any characterization method must satisfy the following crite-

ria:

- Capability to associate any measurement with the cluster residence time to extract homogeneous and meaningful data.
- High repeatability to obtain consistent data across several pulses of the PMCS.
- Capability to determine the mass, structural and morphological properties of clusters independently.

This section outlines the principles of the characterization techniques used to study copper clusters in the gas phase explored in the remainder of this thesis.

1.3.1 *Cluster Mobility Analysis*

A particle moving in a medium gradually loses energy due to interactions with the same. When a constant external force is applied, the particle adopts a mean terminal velocity when the energy imparted by the force and the energy lost to dispersion are in equilibrium. The ease with which the particle moves through the medium is defined as its mobility.

The mobility of a particle is proportional to the cross-section of the particle with respect to the medium surrounding it. It can therefore be used to study the interaction between the two. For clusters in an inert gas, lacking any interaction aside from inertial drag, the mobility gives information regarding the "effective size" of the particles. In this case, "effective size" is a combination of the size and morphological features of the clusters, and determining either independently alongside mobility enables their structural characterization. The mobility study in this thesis is based on the model derived by Mazza et. al. in their 2011 publication [30]. The model is used to determine the fractal dimension D_f of copper clusters from the PMCS in the gas phase, and describe how it evolves with cluster residence time.

The analysis of mobility was carried out using mass and momentum spectrometry of clusters ionized by a pulsed UV laser. A specialized ion spectrometer was designed, constructed, and commissioned for this purpose (Chapter 2). The spectrometer imaged the velocity of cluster ions along the jet, as well as independently measured cluster mass via Time-of-Flight (TOF) spectrometry (Chapter 3).

1.3.2 *Cluster Fragmentation Analysis*

Agglomeration of clusters in the gas phase occurs through the irreversible contact of primary particles undergoing Brownian motion, leading to collision and aggregation, resulting in partial overlap (sintering) between them. The degree of overlap between two primary particles is influenced by their thermal environment at the moment of impact and is therefore indicative of the contact forces acting between them.

Upon energy absorption, the probability of a primary particle dissociating depends on both the contact forces between neighboring particles—determined by their degree of overlap—and the number of such contacts, which is governed by the overall cluster morphology. This thesis introduces a physical model that correlates the yield of dissociated primary particles with the cluster size, fractal dimension D_f, and overlap factor C_{ov} [27]. This framework is subsequently used to track the evolution of C_{ov} as a function of residence time, enabling estimation of the clusters' structural properties.

Characterization of cluster fragmentation was performed via photoion spectrometry of the primary particle ions generated by ionizing clusters with a high-fluence, pulsed visible laser. The same spectrometer previously designed for cluster mobility analysis was employed for this experiment. The spectrometer measures the yield of cluster fragments via TOF spectrometry (Chapter 3).

1.3.3 *Small Angle X-ray Scattering (SAXS)*

Small-angle X-ray scattering is a technique to study material structures at small scattering angles. It utilizes variations in a sample's electron density to generate a high contrast reciprocal space representation of the material's structure [31]. SAXS is a powerful method for studying a sample's size distribution, shape, and surface structure [32]. With advancements in synchrotron and FEL-based X-ray sources that offer high flux and energy, as well as the development of new detectors, SAXS has become a powerful tool in nanoparticle research [33]. As the timescales of the scattering are much faster than any other light-matter interactions, the data obtained from SAXS corresponds to the unperturbed sample system. As it provides access to native structural data averaged over macroscopic sample volumes, [34] combined with the tunable flux and energy, as well as short pulse durations at modern FELs, SAXS becomes ideally suited for in-situ experiments in realistic sample conditions.

The SAXS data from clusters are analyzed to obtain the average radial profile (average intensity of scattering as a function of distance from the scattering center) of the clusters for differing residence times. The unified fit model developed by Beaucage et.al. [35] is used to interpret this SAXS data to extract information about cluster size and morphology by calculating the radius of gyration and fractal dimension of the clusters.

The experiment was conducted at the Small Quantum Systems instrument, in the European X-Ray Free Electron Laser facility, as part of allocated internal and user beamtimes (Chapter 4).

1.3.4 *Studying Time-Resolved Structural Dynamics*

As most differentiation in cluster properties occurs during the agglomeration stage prior to extraction, understanding this growth process is essential for comprehending the overall behavior of these systems. In this work, the cluster growth process is investigated through controlled energy transfer using a pulsed laser of low pho-

ton energy—hereafter referred to as the **pump**. This approach enables the examination of structural dynamics at various time delays following the perturbation [36, 37].

The structural dynamics of the pumped clusters are investigated using SAXS and fragmentation analysis. Tracking changes in the cluster fractal dimension through their SAXS spectra as a function of pump delay allows the morphological evolution of the clusters to be characterized. Monitoring the yield of cluster fragments as a function of delay after pumping, via mass spectrometry, provides insight into their internal structure and how it evolves (Chapter 5).

The processes that occur after the pumping of the clusters are varied and complex, requiring physical modeling or extensive simulation for a comprehensive understanding of their dynamics. This thesis interprets trends in the extracted structural and morphological parameters from experimental observations and derives general inferences regarding the underlying pathways. Fully simulating time-resolved dynamics is beyond the scope of this thesis. Despite the limited scope, the information obtained from these experiments provides valuable insights into constructing a comprehensive understanding of metal clusters, their growth, and properties.

2

WIDE-RANGE MOMENTUM MAPPING OF ELECTRONS AND IONS

2.1 INTRODUCTION

Since its introduction in 1987 [38], photoion imaging has been widely used to study the dissociation dynamics of atoms, molecules, and nanoparticles. Among the photoion imaging techniques, Velocity Map Imaging (VMI) [39] is characterized by its high collection efficiency and simultaneous detection of particles with different velocities and emission angles.

This makes it ideal to study gas-phase copper clusters produced by the Pulsed Microplasma Cluster Source (PMCS) [8], ionized using optical or UV Lasers, and the photoelectrons excited from this process.

Clusters produced by the PMCS are large, with distribution in sizes ranging from hundreds to thousands of atoms [8] seeded in a supersonic gas jet. The cluster velocity has a maximum value equal to the speed of the supersonic jet v_0, which is defined by the species of the carrier gas and temperature (2.1).

$$v_0 = \sqrt{\frac{C_p T}{M}} \tag{2.1}$$

Where T is temperature, M is the molar mass of the gas that makes up the supersonic jet, and C_p is its molar thermal capacity at constant pressure. For an Argon Jet at 300 K, this gives a maximum cluster velocity of 559 m/s. This chapter details the study of photoions and photoelectrons created by ionizing this cluster jet using ion time-of-flight (TOF) and Velocity Map Imaging

(VMI) to characterize the properties of the clusters produced by the PMCS. This also allows explorations of cluster morphologies from the TOF and VMI data by deriving the cluster fractal dimension D_f [30].

Studying these photoions and photoelectrons necessitates the design and development of a spectrometer capable of measuring the VMI of ions and electrons and the TOF of ions having a large momentum acceptance and capable of effectively resolving the ion mass, ion momenta, and the electron momenta across the range of its acceptance.

Spectrometers built to measure both ions and electrons traditionally use a 2-detector setup with a potential gradient driving the ions and electrons towards opposite detectors [40, 41]. Another method is to use switching electric fields to alternate detection of ions and electrons [42, 43]. The low detection efficiency of MCP detectors for large masses [44] and the high cost/complexity of switching potential fields make these approaches unsuitable for this experiment.

A spectrometer for the characterization of cluster ions and electrons needs to satisfy several criteria. The spectrometer needs a large dynamic range to detect ions with high initial momenta. The detected ions must be well-resolved by the spectrometer, both temporally (in terms of time-of-flight or mass resolution) and spatially (in terms of momentum resolution). The spectrometer also needs to resolve the kinetic energy of electrons effectively.

The solution presented in this report involves a spectrometer in a single detector configuration with static potentials. The ion detector in a traditional two-detector system is replaced with a solid electrode, allowing ions to impact it and create electron emission from the electrode surface. The spectrometer design ensures that the detection position of the secondary electrons is directly related to the position of the ions on the conversion electrode. This enables the operation of a VMI spectrometer where the momentum of large ions and photoelectrons is imaged on the same detector.

2.2 DESIGN

The spectrometer design was optimized, tuning aspects such as geometry, spacing, and potentials of the electrodes using SIMION 8.1.1. The final design of the spectrometer is as seen in Figure 2.1. The spectrometer consists of a thick, flat ion lens electrode sandwiched between flat ion extractor electrodes, which act as a focusing system for the ions. The ion flight tube then guides the ions towards the ion conversion electrode (henceforth referred to as iCoP), where they generate secondary electrons upon impact. The iCoP was allowed to have a curved (spherical) shape during the optimization of its geometry. This lead to a concave surface in its current design. The photoelectrons from the ionization are repelled towards the mesh electrode by the ion extractor, which forms an equipotential surface allowing focusing for VMI with the electron flight tube.

The electrodes are biased by a 20 kV high-voltage power supply and high-precision resistors as voltage dividers, with an independent 5 kV power supply for the electron flight tube. Modifying the high voltage bias alters the momentum range of ions detected by the spectrometer, and the independent drift voltage is used to tune the electrostatic focus. The MCP front remains at ground potential.

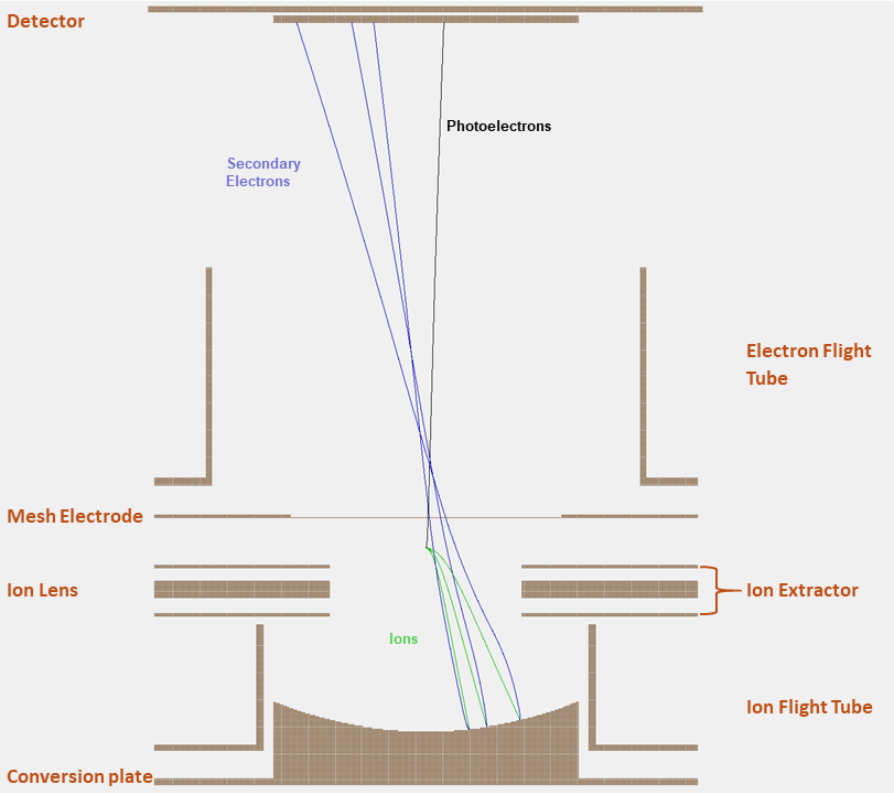

Figure 2.1: Design of the single detector spectrometer employing the iCoP

This iCop provides several advantages for characterizing cluster ions. It allows the application of extremely high potentials for efficient ion conversion without risking damage to the detector. These strong potentials also create strong electrostatic fields that increase the spectrometer's acceptance for ions with high momenta.

The detection is handled by a Roentdek HEX75, which is a triple-stacked micro-channel plate detector with a delay-line anode having an active diameter of 80 mm. It is placed 155 mm above the region of interaction between the cluster jet and the ionizing laser (henceforth referred to as the ion source). The signal from the detector is fed into a Roentdek TDC8HP board for acquisition. This enables high-resolution 2D imaging and timing of charged particles. The detection is event-based, meaning that each valid hit (detection event) on the detector yields positional and timing data for the corresponding particle.

The ion extractors and ion lens are flat electrodes made of copper. The iCoP is a copper cylinder of 90 mm diameter with a

spherical concave top face having a radius of curvature of 116 mm. The center of the iCoP is 55 mm below the interaction region, as viewed from the laboratory frame. The flight tubes are made of carbon-coated Aluminum. The mesh is a 70 lines per inch copper mesh with 80 % transmission, mounted on a flat stainless-steel frame.

2.2.1 *Secondary Electron Detection*

The detection of secondary electrons in place of ions raises two questions. First, how well do the detected secondary electrons retain information about the ions? Second, how reliable are these derived ion TOF and VMI spectra upon changing ion source conditions, such as size and alignment?

To answer the first question, it is necessary to determine whether detecting secondary electrons is equivalent to detecting ions. In essence, ensuring that the arrival times and positions of ions on the iCoP correspond 1:1 to those of the resulting secondary electrons on the detector is necessary. This is verified by running ion simulations with a range of masses, recording the ion and secondary electron TOFs and positions on the iCoP and detector, respectively (Figure 2.2a).

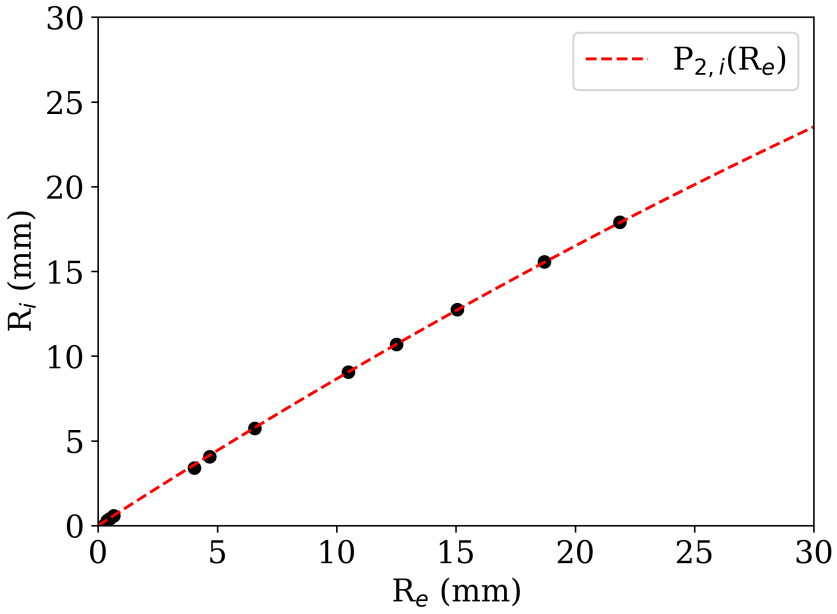

(a)

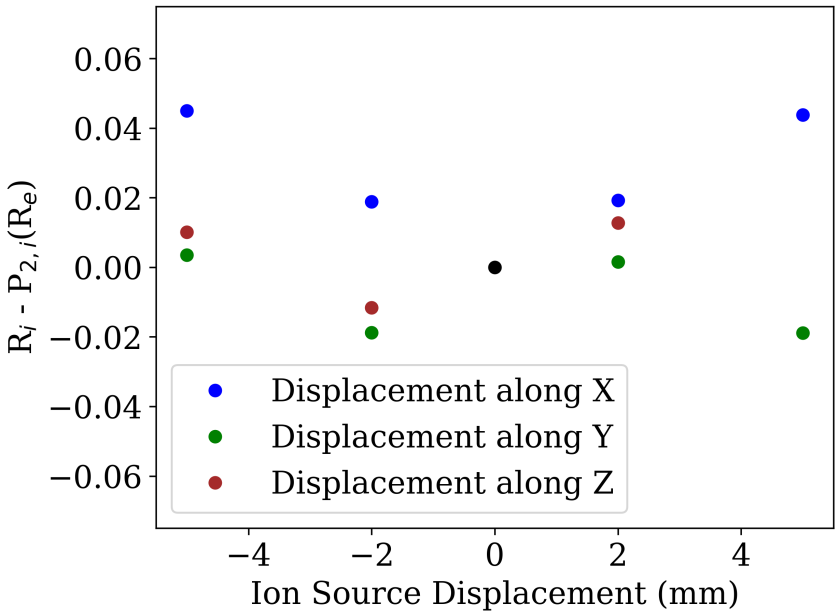

(b)

Figure 2.2: (a) Simulated map of secondary electron hit radius R_e vs. ion hit radius R_i and the 2^{nd} order polynomial polynomial fit $P_{2,i}(R_e)$ relating the two. (b) Difference between R_i and $P_{2,i}(R_e)$ for displacement of ion source along X, Y (parallel to detector plane) and Z (Normal to detector plane).

The radial positions of the secondary electron hits R_e on the detector and the corresponding radial coordinates of the ions on the iCoP (R_i) are seen to map via a 2^{nd} order polynomial function

$P_{2,i}(R_e) = R_i$ with coefficients $(3.35 \times 10^{-3}, 8.94 \times 10^{-1})$. Their corresponding angular coordinates are related as $\theta_i = \theta_e + \pi$. The secondary electron TOFs are constant ($\approx$6 ns) and small compared to the ion TOFs ($\geq$350 ns), so the time of flight recorded at the detector is the ion time-of-flight except for this negligible offset.

To address the second question, the simulation is rerun while displacing the ion source. For each simulation configuration, the difference between the ion hit radius R_i obtained from the simulation and that calculated from the 2^{nd} order polynomial fit $P_{2,i}(R_e)$ is obtained to verify the robustness of this correlation. As seen in Figure 2.2b, there is an absolute displacement $|R_i - P_{2,i}(R_e)| \leq 0.05$ mm on the detector for a source displacement $R_0 \leq 5$ mm along any direction, indicating the secondary electron - ion map is robust and not significantly affected by source displacement.

2.3 SPECTROMETER PERFORMANCES

The performance of the spectrometer is evaluated using several key metrics such as dynamic range, ion mass and momentum resolution, and electron energy resolution. The performance was characterized using simulations and experiments. Experiments were performed on clusters seeded in supersonic beams and on molecular samples back-filling the experimental chamber.

2.3.1 *Dynamic Range*

The dynamic range of the spectrometer was characterized by simulating the largest ion momentum that would be collected entirely by the ion iCoP, while varying the bias voltage applied to the spectrometer. As seen from Figure 2.3, there is a linear correlation between the dynamic range and the applied bias from -7 kV to -20 kV (Device limit) with a maximum detected momentum of 5×10^8 amu m/s. At the speed of the Ar jet (559 m/s), this corresponds to a maximum detected ion mass of 8.9×10^5 amu.

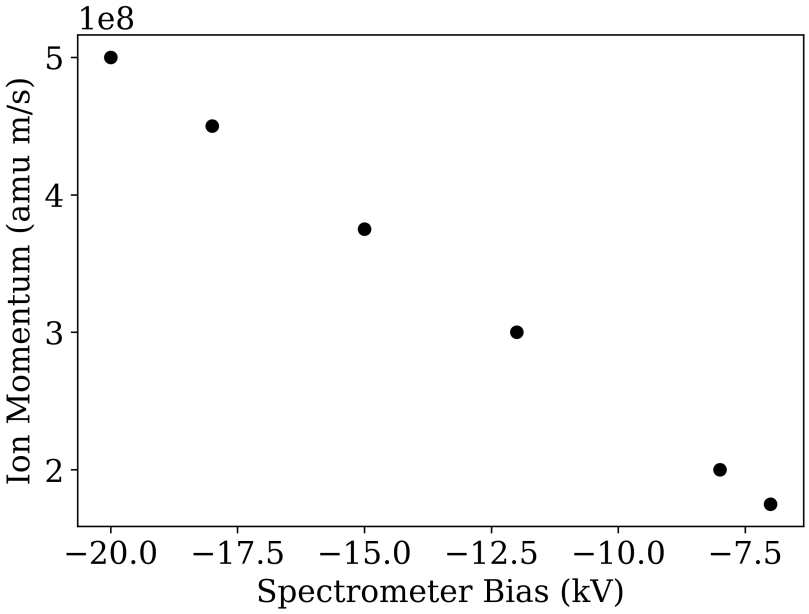

Figure 2.3: Simulations for the largest detected ion momentum in the spectrometer as a function of Spectrometer Bias.

2.3.2 *Mass Resolution*

The spectrometer's performance in resolving photoelectron energy, cluster mass, and momentum was characterized through experiments and simulations using copper clusters, with the spectrometer bias set to -8 kV. At this bias, the spectrometer collects ions with a momentum of up to $2{\times}10^8$ amu m/s with 100% acceptance. This momentum corresponds to an ion mass of $4{\times}10^5$ amu (6.3k Cu atoms) with a velocity of 500 m/s. This velocity was chosen for simulations as a rough representative of mean cluster velocities in typical PMCS operation.

The spectrometer was initially tested by ionizing the rest gas species in the vacuum chamber using a focused UV laser. In the time of flight (TOF) spectra measured from this test (Figure 2.4a), photoelectrons, H_2O^+, and CO_2^+ ions were identified and used to calibrate the TOF to a mass spectrum. The mass spectrum also reveals peaks from CO^+ and from ionized hydrocarbons. This mass calibration was used to characterize the spectrometer by ionizing copper clusters created by the PMCS with a low-intensity UV laser (to minimize cluster fragmentation) and measuring the native mass spectrum of the cluster jet. The resulting spectrum (Fig-

ure 2.4b) shows a mass distribution in the cluster jet, with an ion mass/charge ratio of up to $5{\times}10^5$ amu/e ($\approx$ 9000 copper atoms assuming a unit charge).

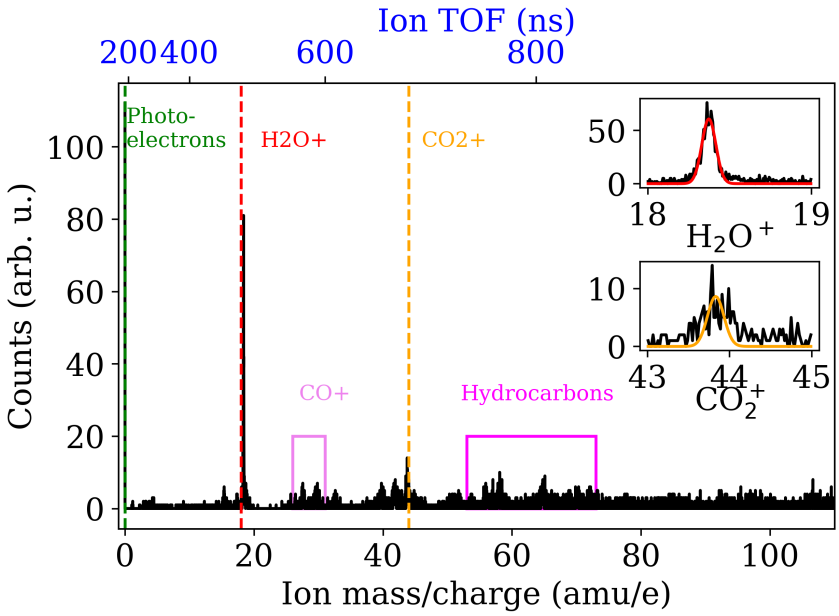

(a)

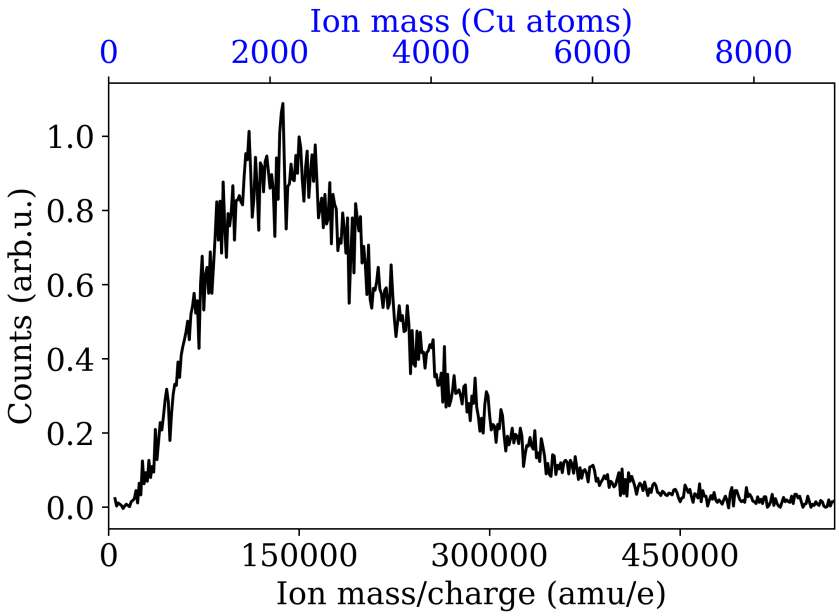

(b)

Figure 2.4: (a) Measured ion mass spectra for rest gases with markers identifying photoelectrons, H_2O^+, CO_2^+, and CO^+. (b) Mass spectrum of ions from copper clusters created using PMCS.

The resolution of H_2O^+, as measured from Figure 2.4a, serves as a reference point to assess the mass resolution performance of the spectrometer. Ion spectra of H_2O^+ were simulated by varying the dimensions of the ion source, which is characterized by a three-dimensional Gaussian profile. Here, $\sigma_y = \sigma_z$ is delineated by the diameter of the ionizing laser at the interaction region, while σ_x is determined by the size of the cluster jet along the trajectory of laser propagation. As depicted in Figure 2.5a, the experimental resolution is well-replicated by an ion source generated with a laser beam of full width at half maximum (FWHM) 330 µm. The value of σ_x is established at 1.2 mm, with the cluster jet width calculated based on the separation between the interaction region and the PMCS, taking into account the dimensions of the intervening skimmer and collimating aperture systems.

Simulating the ion trajectories of copper clusters with initial momenta expected from a supersonic jet, and initial positions determined by σ_x, σ_y, σ_z, the spectrometer's mass resolution capabilities across the range of accepted masses are extracted (Figure 2.5b). The spectrometer is seen to be capable of effectively resolving masses throughout its dynamic range with a mass resolution ≥ 430.

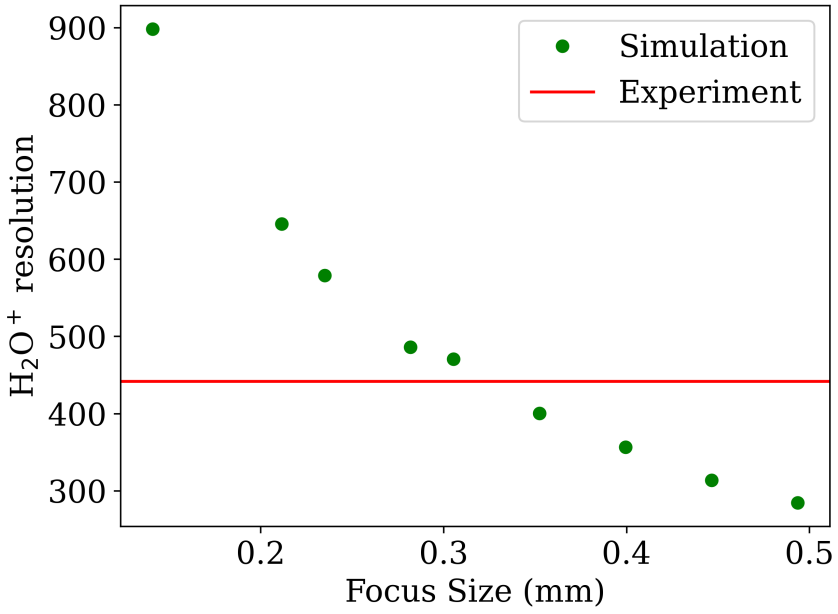

(a)

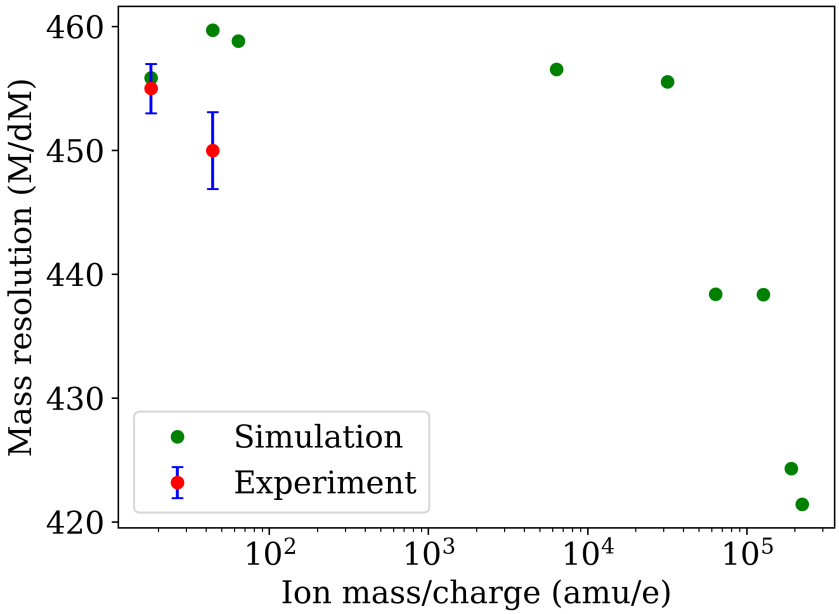

(b)

Figure 2.5: (a) Simulated Mass resolution of H_2O^+ versus 3D Gaussian ion source as a function of the FWHM of the ionizing laser (denoted by the Gaussian FWHM along X : $2.35\,\sigma_x$) with measured mass resolution of H_2O^+ from experiment denoted by the red line to find the intercept. (b) Simulated ion mass resolutions for rest gases and cluster ions in green, with the mass resolution of H_2O^+ and CO_2^+ ions measured from experiment in red. The simulated ion source and the experimental interaction region have similar spatial dimensions.

2.3.3 *Ion Momentum Resolution*

Accurate momentum measurement is required to characterize the spectrometer's momentum resolution capabilities. This requires an understanding of how the misalignment of the ion source affects the detected ion momentum (derived from the hit position on the detector). In experiments, the detected hit position of ions was found to be sensitive to ion source misalignment along the direction of the supersonic jet (Y-direction on the detector). Simulations further confirmed that ion source misalignment along the X-direction (parallel to the detector plane) or Z-direction (normal to the detector plane) does not affect the detected Y-position of the ions.

To characterize this, a cylindrical coordinate system was established with the Y-axis becoming the axial coordinate Y and the XZ-plane becoming the radial plane with coordinates R and θ. The ion detection Y-coordinate for ions with zero initial momentum is defined as Y_0. Y_0 is correlated to displacements along Y and R by simulating ions with no initial momenta with corresponding displacements. Applying Y_0 as an offset, the difference dY between the Y hit positions detected with source displacement and those detected for a centered ion source is calculated, simulating ions with a range of momenta. As we can see from Figure 2.6, if Y_0 can be determined, the accurate Y hit positions of ions and consequently, their velocities and momenta can be calculated.

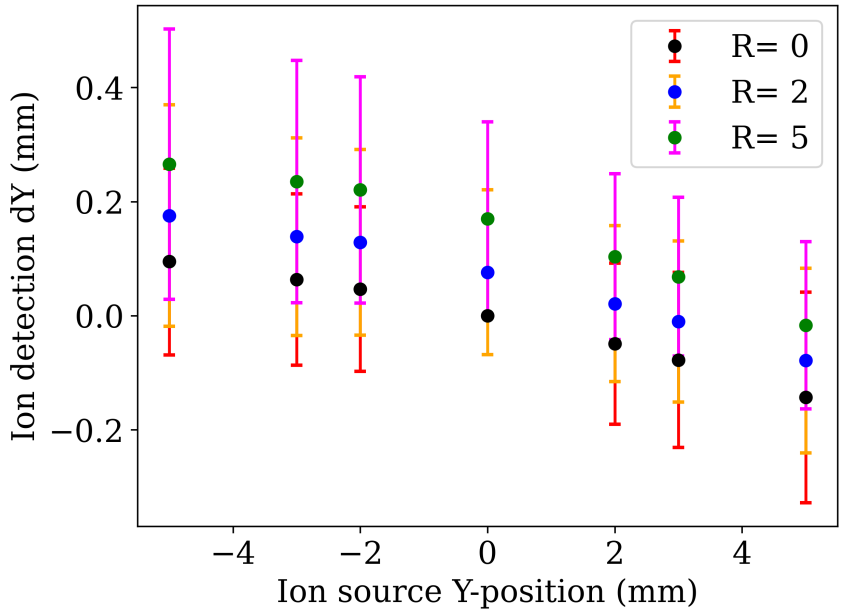

Figure 2.6: Average Difference in ion hit along y direction (dY) with corrections for Y_0 for different radial positions. The error bars signify the standard deviation of the ion Y-hit positions for each position.

Experimentally, this determination of Y_0 is performed by mapping the position of rest gas species in the spectrometer chamber, such as H_2O^+.The histogram of the corresponding events along the Y-direction is then calculated and fitted with a Gaussian profile to extract Y_0(Figure 2.7).

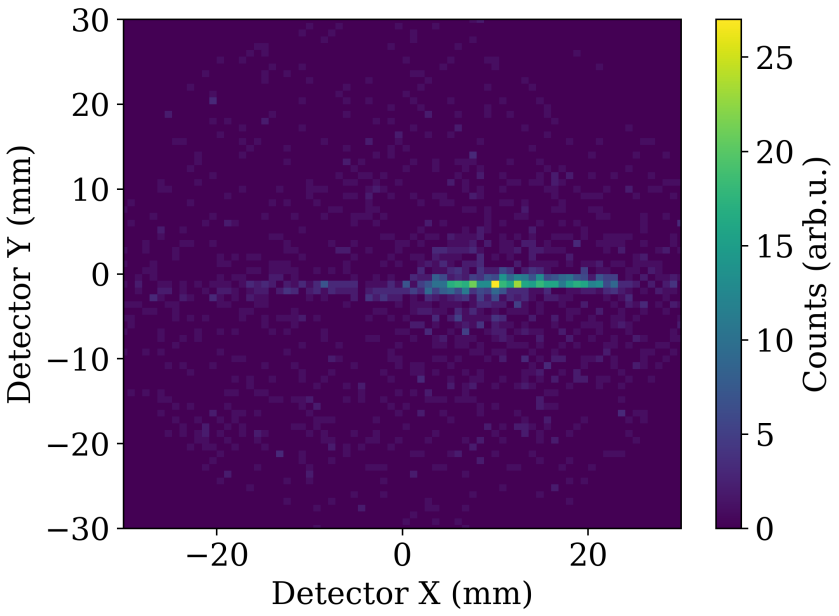

(a)

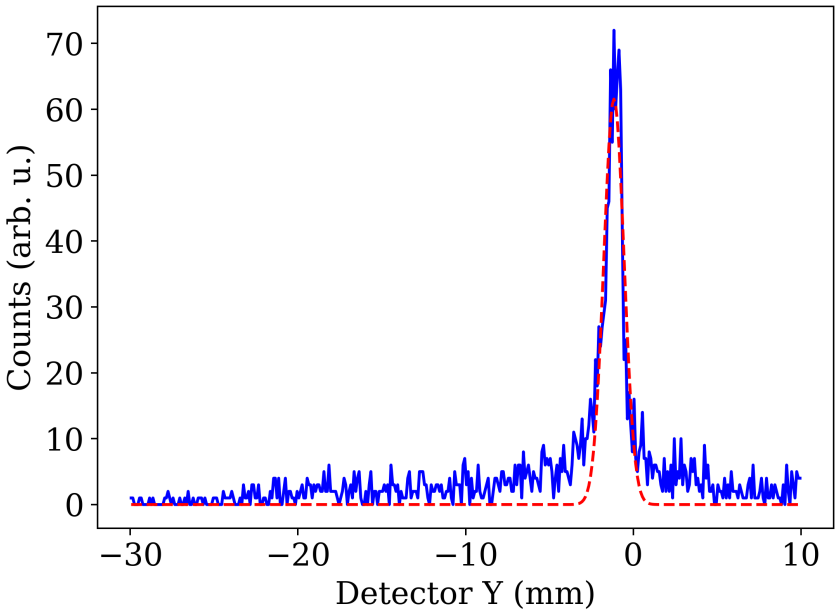

(b)

Figure 2.7: (a) Map of H_2O^+ position on detector.(b) Histogram of H_2O^+ hits along the y-direction of the detector, with a dotted line signifying a Gaussian profile fit.

Measurement of the spectrometer's performance in high-momentum ion resolution necessitates testing with cluster ions from PMCS. The ion velocity in the jet is initially determined from TOF and hit position. The distribution of cluster masses (as seen in Figure 2.4b) and the variations in cluster properties due to the pulsed na-

ture of the PMCS jet necessitate the calculation of average cluster momenta.

Due to the lack of a monochromatic beam of ions with uniform masses and momenta, it is impossible to directly compare the experimental resolution of the momentum distributions to that of the simulations. Selecting a homogeneous cluster sample, binned for statistically significant data (having residence times between 140 ms and 160 ms), the clusters are observed to have an average velocity of 430 m/s.

Comparing the width of the momentum distribution calculated with this binning (by taking the average momentum value for a bin and dividing by its standard deviation) to the momentum resolutions of simulated cluster ions with similar momenta (Figure 2.8), the simulated ion momentum resolutions are higher than the distribution momentum width, as expected. The spectrometer is thus amply capable of characterizing the momenta of high momentum ions.

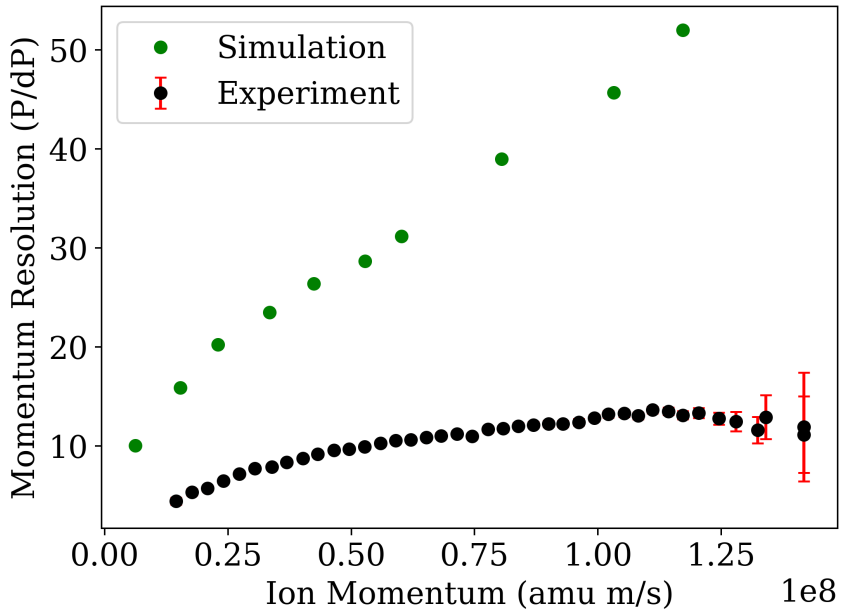

Figure 2.8: Momentum resolution of cluster ions calculated from simulations(green). Also shown are the experimental momentum widths of the momentum distribution from the PMCS, binned for statistical significance (black).

2.3.4 *Electron Momentum Resolution*

The spectrometer's capabilities in resolving electron energies were characterized using simulations of photoelectrons emitted from a 3D Gaussian source identical to the ion source. The simulated photoelectron had energies ranging from 1 eV to 20 eV, flying 50k particles for each energy (2.9a). The energy resolutions of these electrons on the spectrometer are calculated by performing a Gaussian fit on the Abel inversion [45] of their distribution on the detector.

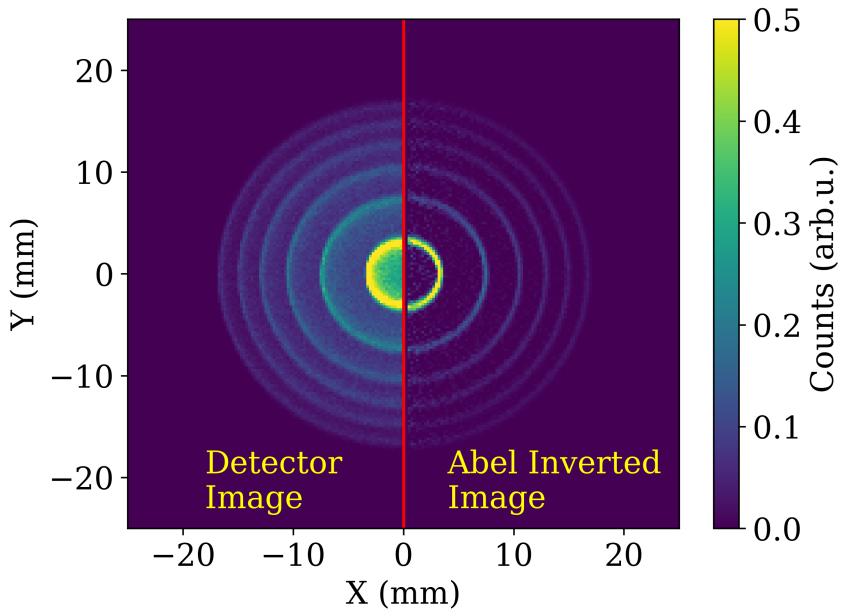

(a)

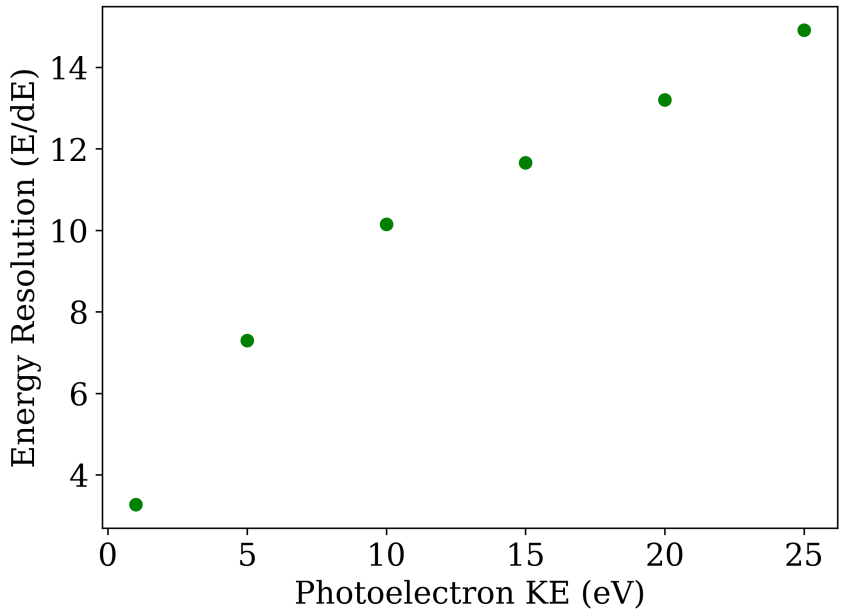

(b)

Figure 2.9: (a) Detector image (left) and Abel inversion (right) of simulated VMI signal from photoelectrons ranging from 1 eV to25 eV. (b) energy resolutions for the same.

As seen from 2.9b, the energy resolution capabilities of the spectrometer are rather low. This poor resolution, combined with the relatively low kinetic energy photoelectrons (<2 eV) excited by ionizing clusters with UV, makes the electron spectrum from

experiments blurry and difficult to characterize.

2.4 RESULTS

The goal of designing this spectrometer was to create a single-detector solution for characterizing photoelectrons and high-momentum ions, as stated at the beginning of this chapter. As seen in the previous sections, this prototype satisfies the conditions of high dynamic range and mass resolution. The momentum resolution of ions by the spectrometer is satisfactory for samples from the PMCS on testing. This prototype is limited in its ability to resolve electron momenta, as discussed in the previous section.

This version of the spectrometer prototype is thus effective for characterizing ions of PMCS clusters. Still, it is insufficient for conducting any serious analysis of the low-energy photoelectrons created by ionizing the clusters with an optical laser. This prototype is used in the following chapters to characterize cluster ions.

3

MORPHOLOGICAL AND STRUCTURAL CHARACTERIZATION OF GAS-PHASE CLUSTERS

3.1 INTRODUCTION

Free metal clusters are frequently represented as spheres to account for their electronic characteristics [46]. The process by which PMCS clusters grow by agglomeration of smaller clusters (primary particles) is characterized by stochastic [47] and multiplicative [48] dynamics. Due to the localized nature of the PMCS discharge, the temperature of the thermalization cavity only increases slightly, to near room temperature. The rapid quenching of the microplasma and supersonic expansion means that the majority of cluster agglomeration occurs at temperatures lower than room temperature. Such a process leads to structurally complex and heterogeneous clusters within the supersonic jet, despite their small size (section 1.2). Moreover, the characterization of nano-structured solids assembled from cluster nanoparticles in the gas phase indicates that the structural intricacy of free clusters significantly influences the properties of the assembled material [49].

A comprehensive understanding of cluster properties necessitates a multi-parametric evaluation, encompassing size, morphology, stoichiometry, and spatial distribution. This chapter delves into two experimental approaches for the quantitative morphological characterization of copper clusters from the PMCS over long residence times.

The initial approach is predicated on gas-phase ion mobility measurement principles [50], utilizing a size-independent parameter: the cluster fractal dimension D_f.

The second approach uses the yield of cluster fragmentation alongside the fractal dimension to model the contact forces be-

tween primary particles during the cluster's formation, utilizing the cluster overlap factor C_{ov}.

3.2 EXPERIMENTAL SETUP

This characterization of cluster size, mobility, and fragmentation is based on the single detector spectrometer described in Chapter 2. The experimental setup consists of the spectrometer installed with its axis perpendicular to the direction of propagation of the cluster jet in a chamber maintained at ultra-high vacuum (3×10^{-8} mbar).

For this characterization, the PMCS and expansion chamber are connected via a vacuum chamber to the spectrometer chamber, having the clusters fly for ≈ 1 m before ionization and detection. The source is operated in the internal trigger mode parameters described in section 1.2.1.

As the spectrometer's detection system is event-based, this allows for the determination of the time of flight and position for each detected photoelectron or secondary electron. This enables the characterization of ion mass and ion momentum, which facilitates the mobility analysis of cluster ions, as discussed in later sections.

Based on the distance between the PMCS and the spectrometer, and assuming cluster velocity of ≈ 500 m/s (considering speed of supersonic Ar at room temperature), the time between cluster extraction and ionization and detection is less than 2 ms. This detection timescale is much shorter than the PMCS duty cycle period (300 ms), and can be neglected. This means that the time between source discharge and ion detection is a good approximation of the residence time of the detected cluster ion. It can be measured experimentally by referring the detection event time to a trigger signal synced to the PMCS pulsed valve. [25]. (Figure 3.1)

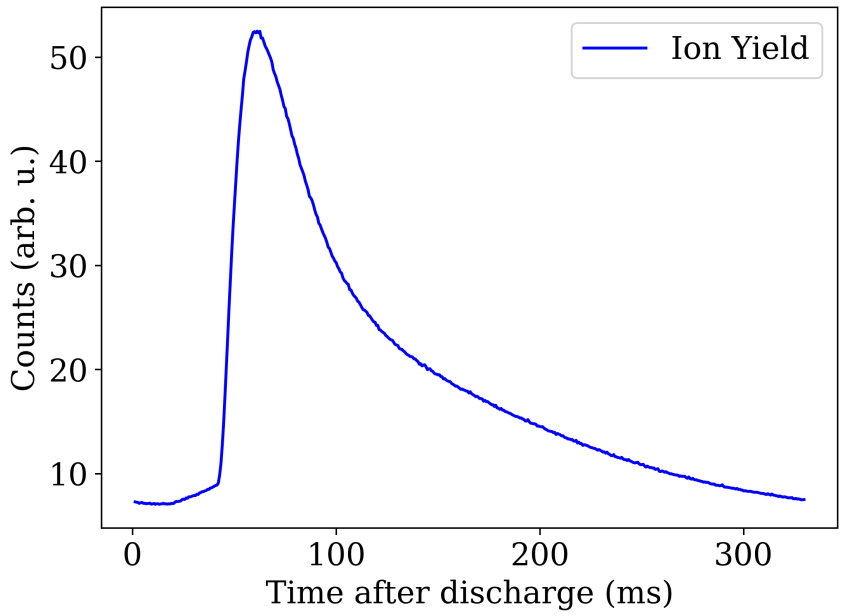

Figure 3.1: Ion yield as a function of time after PMCS discharge, giving the residence time profile of the clusters for the PMCS configuration used in these experiments.

The ionization probe is a focused, pulsed laser incoupled to the spectrometer chamber with its beam path orthogonal to both the cluster jet and the spectrometer axis. Alignment ensures that the laser and the jet meet in the interaction region of the spectrometer. The laser has a pulse rate of 3 kHz with a fundamental frequency of 800 nm and a pulse duration of ≈30 fs. The beam delivered to the spectrometer can be the fundamental, frequency doubled (400 nm) or frequency tripled (266 nm) mode of the laser. The beamline uses a third harmonic generation femtokit [51] together with dichroic mirrors to change the photon energies of the beam delivered to the spectrometer.

This allows for the study and characterization of cluster photoions ionized by different photon energies while accounting for the high momentum of cluster ions from the supersonic jet.

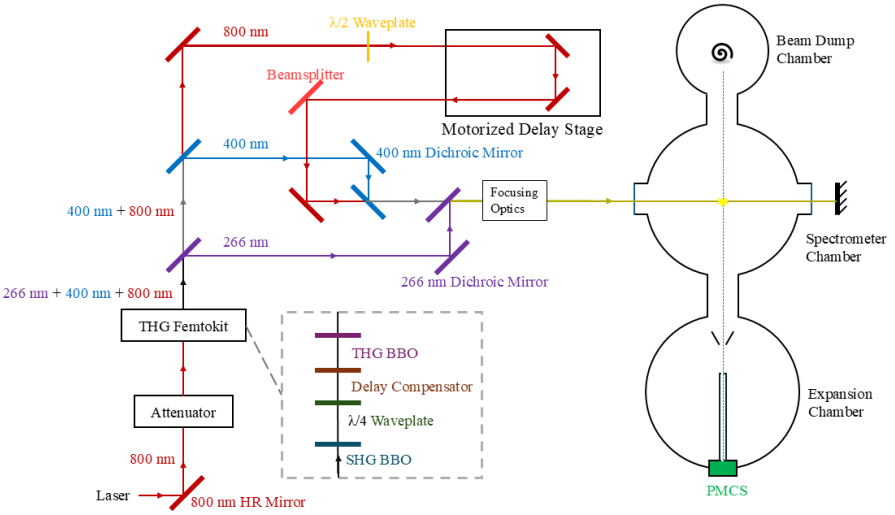

Figure 3.2: Schematic of experimental setup for cluster ion characterization. The setup is capable of delivering 800 nm, 400 nm or 266 nm laser to the spectrometer chamber. The 800 nm brach of the beamline consists of an optical delay stage and a polarization based attenuator to facilitate pump-probe measurements.

3.3 RESULTS

3.3.1 *Cluster Mass Spectra*

The copper clusters were ionized using a frequency-tripled (266 nm) UV laser having a laser fluence of 1.9×10^5 J/cm^2 for mass spectrometry. This choice for wavelength and fluence minimizes the chances of cluster fragmentation or multiple ionization while maintaining reasonable acquisition times for statistically significant datasets. In the fixed operating mode of the PMCS, the mass spectra of the detected copper cluster ions range from hundreds to several thousands of copper atoms. The distribution is plotted for clusters with residence times between 140 ms and 160 ms in figure 3.3a.

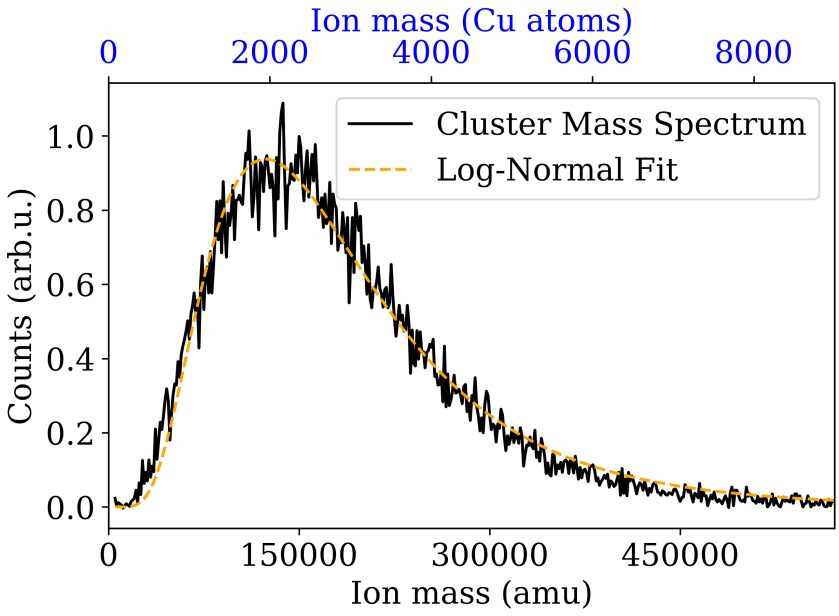

(a)

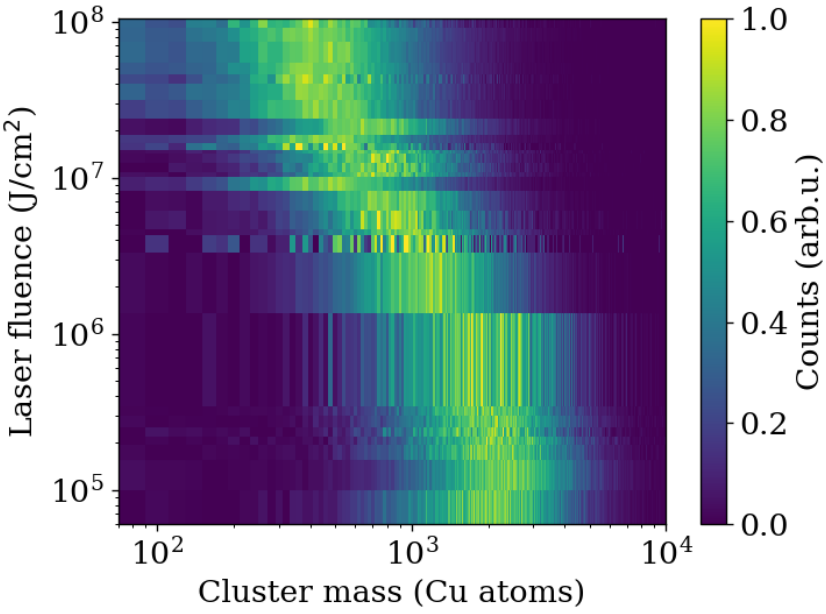

(b)

Figure 3.3: (a) Mass spectrum of cluster ions from PMCS with residence times between 140 ms and 160 ms ionized with UV laser at a fluence of 1.9×10^5 J/cm^2, showing their log-normal profile. (b) Map of cluster mass spectra for different UV fluence displaying nonlinear effects during ionization

The histogram of ion yield versus cluster mass (m) displays a log-normal profile Y_{L-N}. This is to be expected from the stochastic and multiplicative nature of the agglomeration process [47, 48].

The expression for this distribution is given by:

$$Y_{L-N} = \frac{1}{m\sigma\sqrt{2\pi}} exp\left(-\frac{(ln(m)-\mu)^2}{2\sigma^2}\right) \tag{3.1}$$

The mean and standard deviation of this distribution are defined as:

$$Mean_{L-N} = \left(\mu + \frac{\sigma^2}{2}\right) \tag{3.2}$$

$$Std_{L-N} = [exp(\sigma^2) - 1]\, exp(2\mu + \sigma^2) \tag{3.3}$$

The photon energy of the 266 nm probe is close to the ionization potential of copper clusters. Therefore the measured mass spectrum will be influenced by fluence-dependent effects. These need to be characterized to determine the native mass distribution of the clusters detected by the spectrometer.

These effects are characterized by measuring the mass spectra of copper clusters, varying the attenuation and focus size to tune the fluence of the 266 nm laser. The mass distribution (at residence times between 140 ms and 160 ms) trends towards heavier masses at lower fluence as observed from the resulting map of cluster mass spectra (Figure 3.3b).

To analyze the mass spectra in figure 3.3b, the log-normal fitting parameters μ and σ of each mass spectrum are plotted as a function of the laser fluence F.

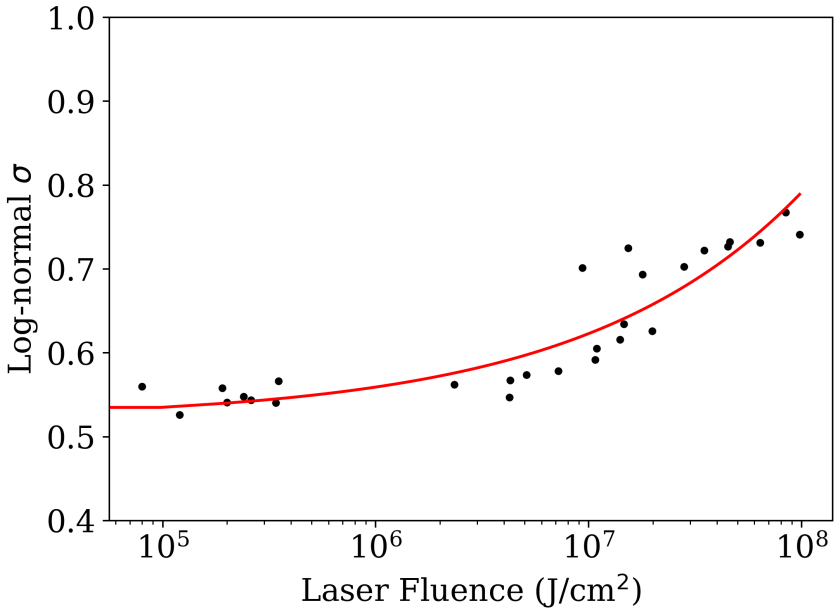

(a)

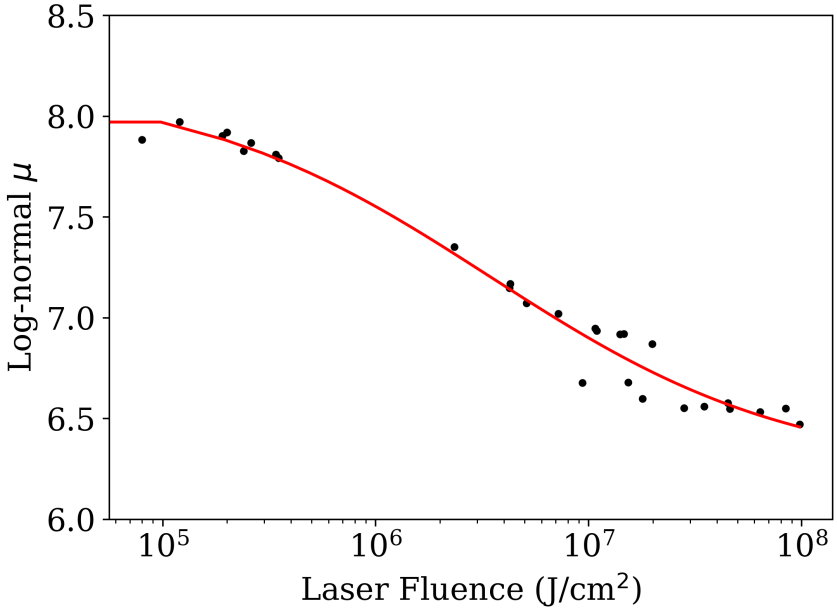

(b)

Figure 3.4: Log-Normal fitting parameters (a) μ and (b) σ of PMCS cluster mass spectrum varying with laser fluence F and power-law fits of each.

As seen in Figure 3.4, both parameters scale with some power of F. σ increases with F leading to a power-law of the form (Equation 3.4):

$$\sigma(F) = a_\sigma + b_\sigma F^k \tag{3.4}$$

Where a_σ is the offset, corresponding to the value of σ at 0 fluence, and b_σ is a scaling factor.

μ decreases with increasing F, but necessarily has a finite value at $0\,\mathrm{J/cm^2}$. This behavior can be modeled as a power-law of the form(3.5):

$$\mu(F) = a_\mu \left[\frac{d_\mu}{F^n + c_\mu} + 1 \right] \tag{3.5}$$

Where a_μ is the asymptotic value of μ for high fluences; c_μ and d_μ are scaling factors of the parameter with fluence; and $a_\mu \left(\frac{d_\mu}{c_\mu} + 1\right)$ is the value of μ at 0 fluence.

Fitting equation 3.4 to the data in Figure 3.4a and equation 3.5 to the data in Figure 3.4b allows for the retrieval of these parameters for the given PMCS configuration at $F = 0$ via extrapolation. This zero fluence distribution has log-normal fitting parameters $\mu(0) = 8.017$ and $\sigma(0) = 0.517$. This corresponds to an average cluster mass of 3500 Cu atoms and a standard deviation of 1900 Cu atoms for residence times between 140 ms and 160 ms. This is contrasted against cluster mass spectra for high fluence ($>6\times10^7\,\mathrm{J/cm^2}$) and low fluence($< 3.5\times10^5\,\mathrm{J/cm^2}$) laser in Figure 3.5.

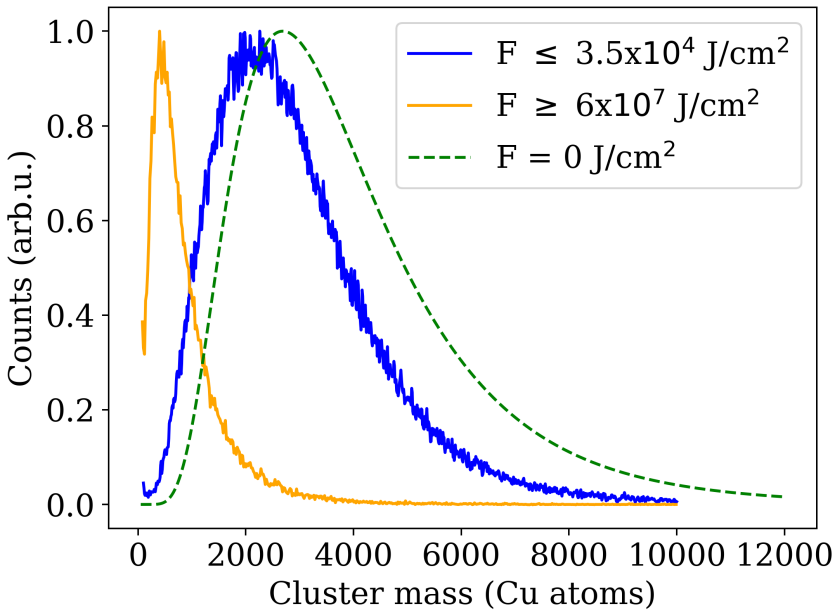

Figure 3.5: Mass spectrum of cluster ions from PMCS at low and high laser fluence, with the profile of mass distribution at zero fluence for comparison

Retrieving the mass distributions for low-fluence runs ($F \leq 1.9\times10^5\,J/cm^2$) at different residence times reveals a distinct evolution of cluster properties, after correcting for ionization cross section.

Mapping the features of the log-normal profile reveals that the average mass and standard deviation of the cluster mass distribution increase with residence time up to $\approx 150\,ms$. The average cluster mass remains almost constant at residence times higher than 150 ms, whereas the standard deviation of the distribution decreases (Figure 3.6).

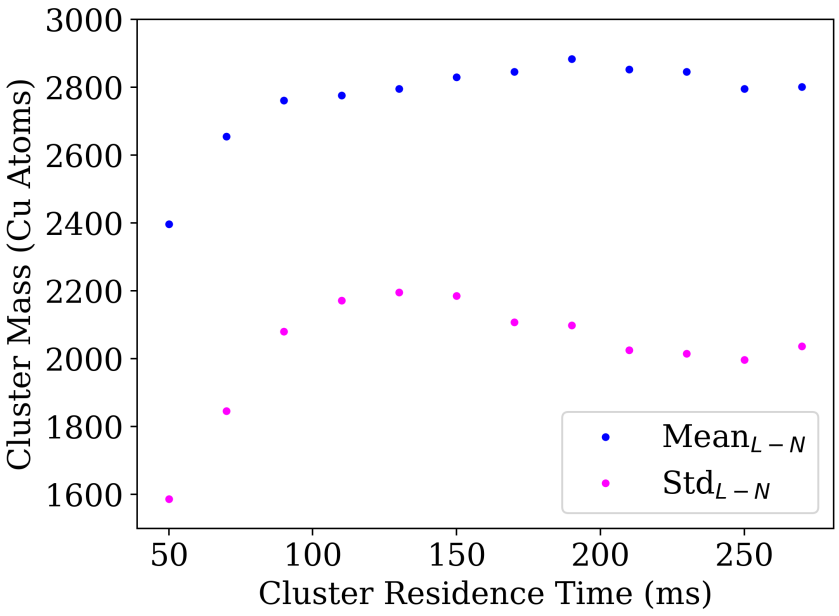

Figure 3.6: Mean and standard deviation of cluster masses from the PMCS as a function of their residence time, obtained by log-normal fit

The mass spectra used for these calculations have not been corrected for their ionization cross-section. At high laser fluence, due to the effects of fragmentation and multiple ionization, calculations of ionization cross sections for different masses become complicated. This is due the inability to identify the contributions of various nonlinear processes. As the fluence approaches $0\,\mathrm{J/cm^2}$, assuming the clusters to be opaque, the ionization cross section at a given residence time becomes directly proportional to the geometric cross section of the clusters A_{geo} [52]. The geometric cross-section is itself proportional to the mass of the clusters (given by the number of atoms in the cluster N_z) [28] as:

$$A_{geo} \propto N_z^{\left(\frac{2}{D_f}\right)} \tag{3.6}$$

Where D_f is the mass-independent fractal dimension of the clusters at the selected residence time, which indicates their morphology. D_f, retrieved from the mobility analysis in the next section, enables the retrieval of the $N_z^{\left(\frac{2}{D_f}\right)}$ term for each residence time. The native mass distribution of copper clusters produced by

the PMCS in this residence time window can be visualized by dividing the zero fluence distribution by this term.

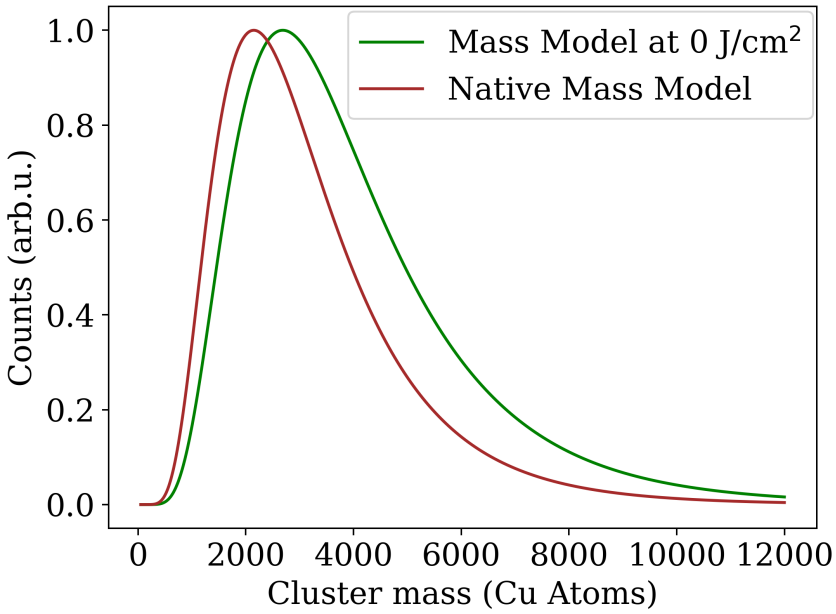

Figure 3.7: Mass distribution model of PMCS clusters between 140 ms to 160 ms at zero fluence (green) and native mass distribution model (brown) obtained by correcting for ionization cross section based on equation 3.6

For residence times 140 ms - 160 ms the native mass distribution thus obtained (Figure 3.7) has a log-normal profile with an average cluster mass of 2800 Cu atoms and a standard deviation of 1500 Cu atoms for this PMCS configuration.

3.3.2 *Mobility Analysis*

The clusters seeded in the supersonic beam gain velocity by colliding with the faster, lighter carrier gas atoms. The final velocity of each cluster depends on: its mass, its collisional cross section (which relates to its morphology), and the effectiveness of each collision in transferring momentum.

Modeling terminal velocity based on these collisions reveals the efficiency of cluster acceleration by the carrier gas. This efficiency is conceptually similar to its mobility. Modeling cluster velocity as

a function of mass gives access to morphology, which governs the mobility of clusters in supersonic beams [30].

As discussed in Chapter 2, the event-based detection of ion TOF and position of the spectrometer allows mobility analysis of the clusters through velocity modeling. For ease of analysis, the data of ions created at fluence $< 3.5{\times}10^5$ J/cm^2 is henceforth used for characterization. This significantly reduces the margin of error introduced to the analysis by alternatively attempting to extrapolate the TOF and positional data of ions as a function of laser fluence and retrieving the native cluster velocity based on these results.

This work uses the cluster velocity model established by Mazza et al. in 2011 [30] to compute the fractal dimension D_f of the clusters. The clusters seeded in the supersonic expansion are accelerated along the jet axis by collisions with the expanding gas molecules. The effectiveness of each collision in transferring momentum is assumed to be constant. This would mean that the terminal cluster velocity is determined by the number of forward kicks the cluster experiences. This number is then affected by the particle's collisional cross section, under the assumptions of the model. This model describes the velocity v of clusters as a function of their mass m and their morphological factor ξ as expressed in equation 3.7:

$$v(m,\xi) = v_{gas}\left[1-\left(\frac{m-m_{gas}}{m+m_{gas}}\right)^{\tilde{\beta}\cdot m^{\xi}}\right] \tag{3.7}$$

Where m_{gas} is the atomic weight of the carrier gas, v_{gas} the terminal velocity of the carrier gas, $\tilde{\beta}$ is the effective collision pre-factor, and $\xi = \frac{D^*}{D_f}$, where D_f is the fractal dimension of cluster's volume in 3D, and D^* the fractal dimension of their projection in 2D. ξ here is treated as a free parameter that varies with residence time to allow for flexible modeling of cluster velocity.

The carrier gas velocity v_{gas}, and collision pre-factor $\tilde{\beta}$ are defined in terms of the residence time t_{res}, and the PMCS temper-

ature relaxation time τ as:

$$v_{gas}(t_{res}) = v_0 \cdot e^{t_{res}/2\tau} \tag{3.8}$$

$$\tilde{\beta}(t_{res}) = \tilde{\beta_0} \cdot e^{3t_{res}/2\tau} \tag{3.9}$$

Where v_0 and $\tilde{\beta_0}$ are the values of v_{gas} and $\tilde{\beta}$ respectively at zero residence time.

This enables modeling of cluster velocity given the mass and residence time of the clusters. The velocity of clusters along the cluster jet can be retrieved for each event from the TOF and positional data of ions, after correcting for the offset of ionization position (mapping position of H_2O^+ ions as established in chapter 2).

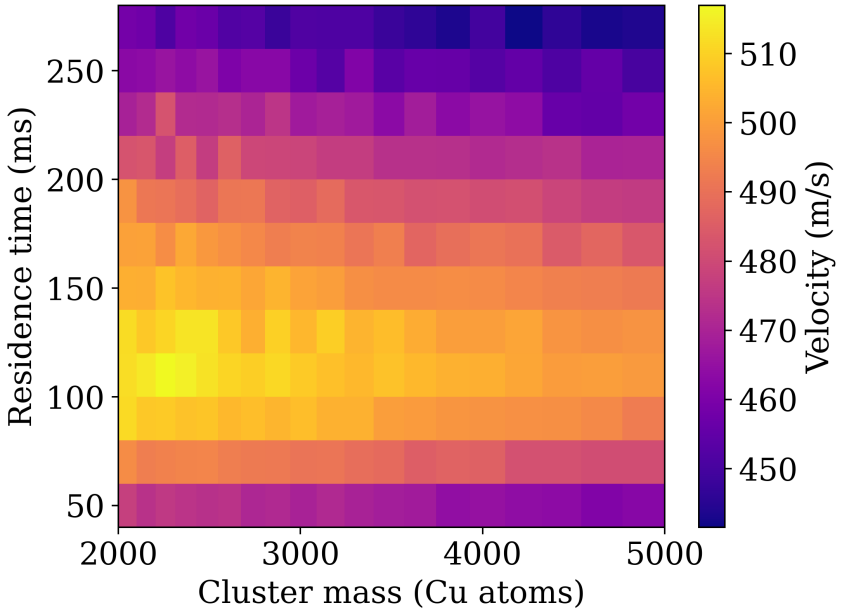

Figure 3.8: Cluster velocity map based on cluster mass and residence time.

Mapping cluster velocities based on their masses and residence times illustrates the trends in their evolution (Figure 3.8). Velocity decreases with increasing mass, for each residence time bin. Keeping mass fixed, cluster velocity shows an increase with residence

time up to ≈ 150 ms, and then decreases slightly. This evolution of cluster velocity with mass and residence time is studied using the model described in equation 3.7. Fitting the measured velocity of clusters with the expression provides information about their fractal dimension D_f as a function of residence time (t_{res}).

The PMCS temperature relaxation time τ and initial carrier gas velocity v_0 were independently determined by residence time-resolved measurement of carrier gas velocities. The yield of Ar^+ ions is quite low when ionized with a 266 nm laser, making it an unsuitable species for this measurement. Doping a trace amount of O_2 into the Ar mixture yields an O_2^+ signal, which is used to extract residence time-based velocity data for the carrier gas. On fitting this with equation 3.8 τ and v_0 for this configuration of the PMCS are found to be 1174 ms ± 293 ms and 534 m/s ± 10 m/s respectively (Figure 3.9).

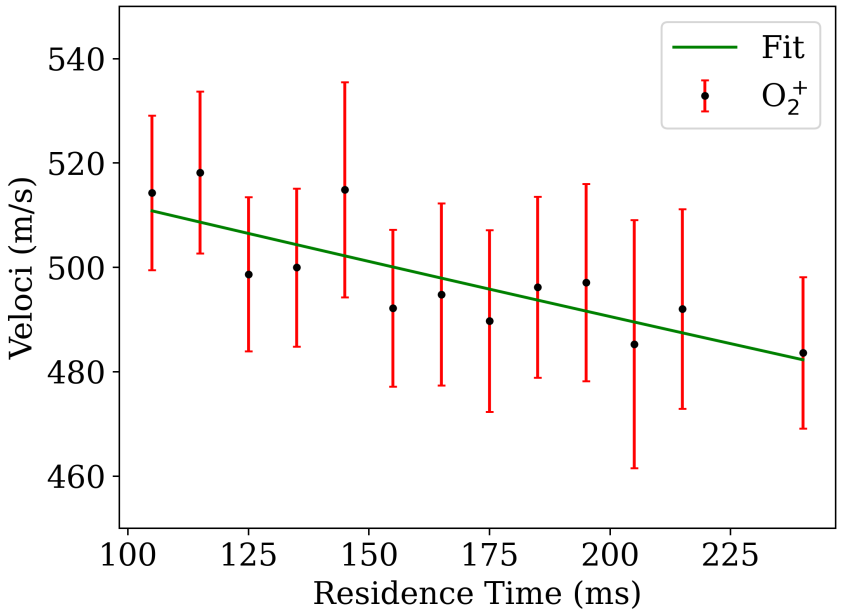

Figure 3.9: Residence time resolved plot for velocity of O_2^+ seeded in a supersonic jet of Ar. The error bars denote the uncertainty in determining velocity, based on Gaussian fitting of position and TOF. The solid green line is the data fitted by equation 3.8.

With the array of ξ values for each t_{res} bin and $\tilde{\beta}_0$ as free parameters, a least squares fit shows that the model agrees with the experimentally retrieved cluster velocity with a margin of error

±4% (Figure 3.10).

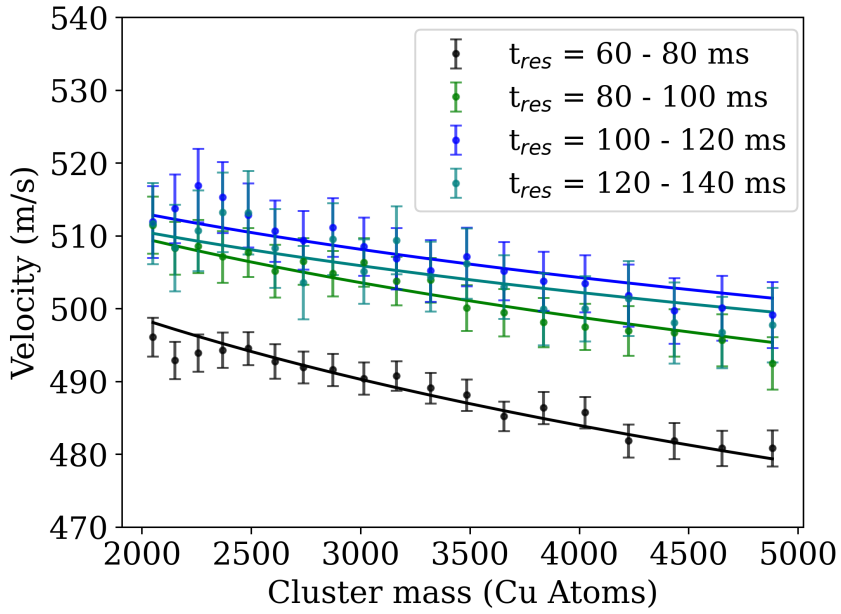

(a)

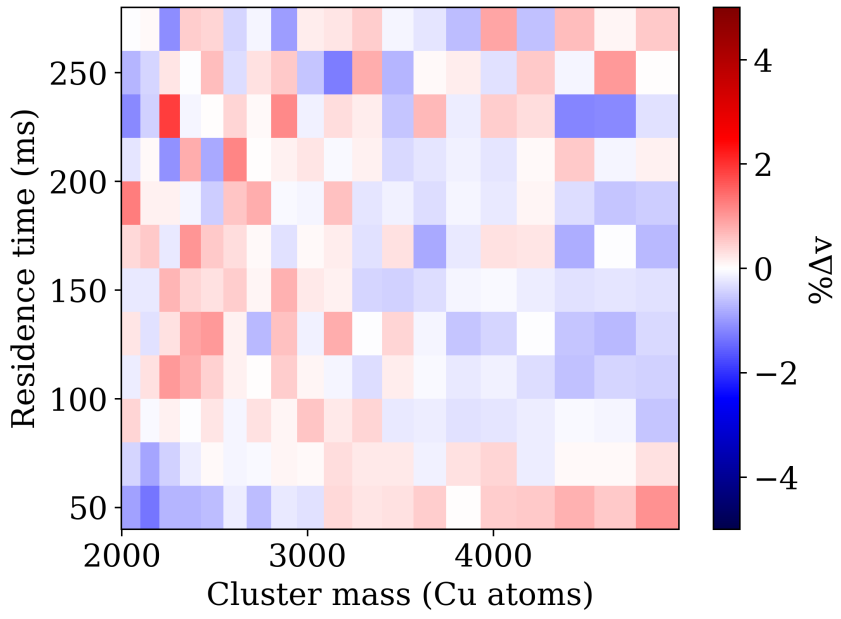

(b)

Figure 3.10: (a) Cluster velocity as a function of mass for different residence times, with the solid line denoting the velocity derived from equation 3.7. (b) Map of percentage difference between measured velocity and velocity obtained from fit, showing a maximum error of ±4%

Based on previous literature [30], the fractal dimension D_f of clusters from the PMCS is between $2 < D_f \leq 3$, implying $\xi = 2/D_f$. From the values of ξ obtained from the fit, the fractal dimension D_f of PMCS clusters decreases from 2.44 to 2.33 by residence time of 150 ms, but then increases slightly to 2.35 by 300 ms (Figure 3.11), with an uncertainty of ± 0.04. Based on this uncertainty in retrieving D_f ,the retrieved values are compatible with a constant D_f for t_{res} >150 ms.

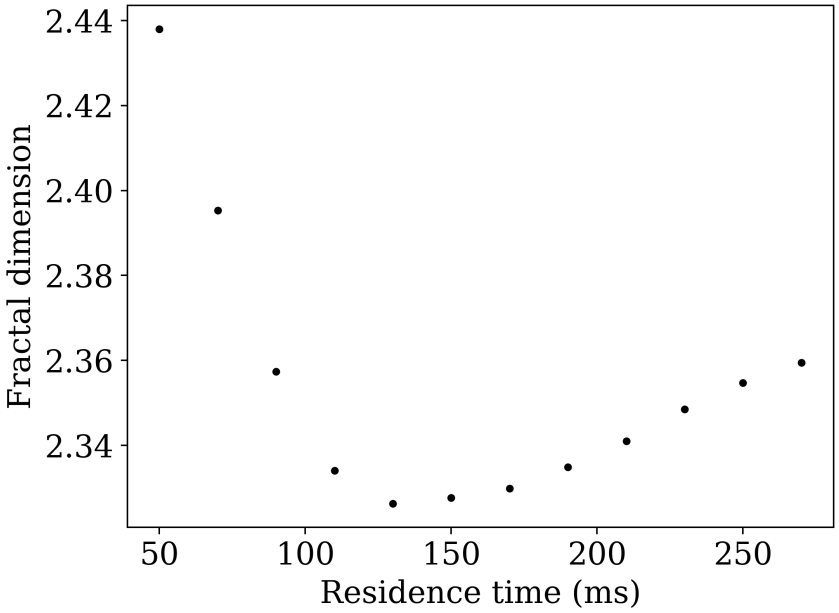

Figure 3.11: Evolution of cluster fractal dimension D_f as a function of residence time t_{res} based fitting results of equation 3.7. The retrieved values of D_f have an uncertainty of ± 0.04.

The mobility analysis of copper clusters created by this configuration of the PMCS displays distinct features from reference [30]. The extremely high collision relaxation time τ implies that the temperature of the carrier gas and clusters inside the PMCS cavity decreases slowly. This thermal impedance may be an effect of the long focusing stage. Another interesting feature is the increase/stagnation in fractal dimension at residence times greater than 150 ms. This contrasts with the observations of ref. [30] that the fractal dimension strictly decreases with residence time. The possible reasons for this deviation are discussed in the conclusion

of this chapter.

3.3.3 *Cluster Fragmentation Analysis*

The internal structure of cluster agglomerates can be investigated through their controlled fragmentation into the primary particles that constitute them.

The mass spectrum of copper clusters ionized using the frequency-doubled (400 nm) laser (Figure 3.12) differs markedly from that obtained with the 266 nm laser (Figure 3.3). Ionization with the 400 nm laser produces a mass spectrum featuring three regions as contrasted to the log-normal distribution of the UV-ionized clusters: the first peak corresponding to large masses ($\geq$ 300 Cu atoms); a second peak at smaller masses in the range of 100–300 Cu atoms; and finally a large number of very small ions, including Cu^+ atoms.

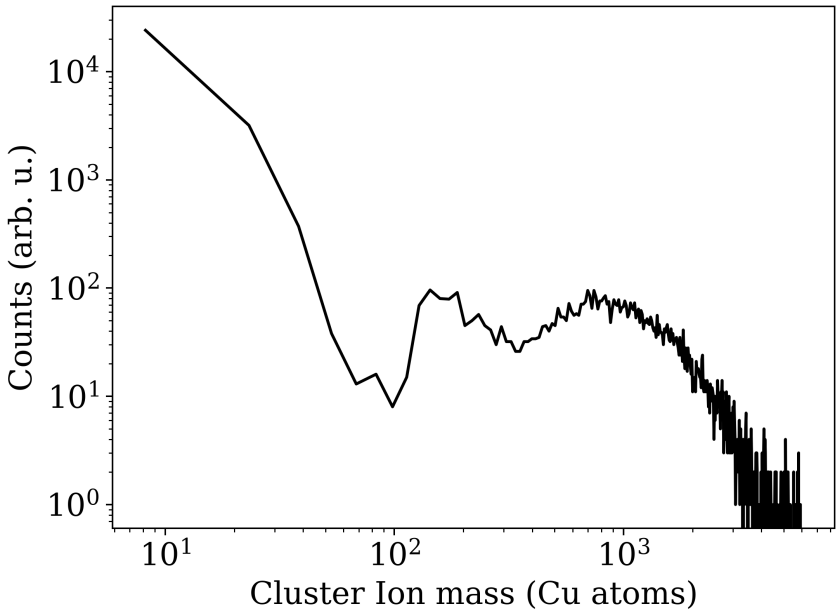

Figure 3.12: (a) Mass spectrum of cluster ions with residence time between 140 ms - 160 ms ionized by 400 nm laser.

The significance of the two peaks in the mass spectra becomes evident from the momentum resolved mass spectra of the cluster ions (Figure 3.13).

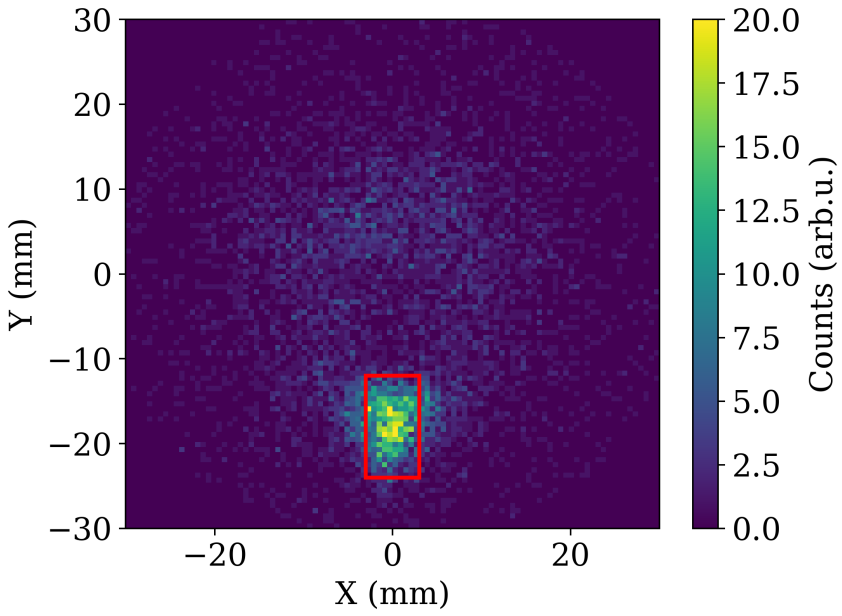

(a)

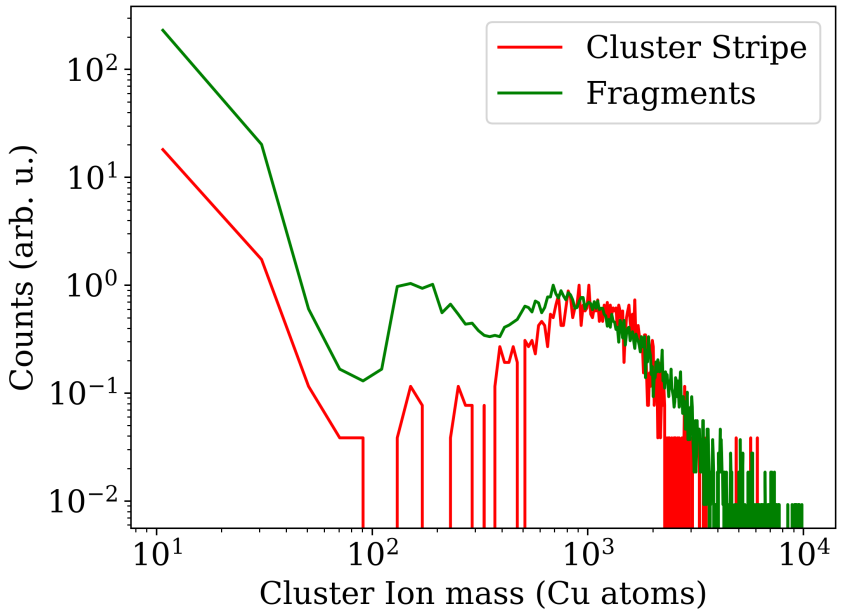

(b)

Figure 3.13: (a) Momentum map of cluster ions with residence time between 140 ms - 160 ms ionized by 400 nm laser. The ions within the red box signify whole and dissociated cluster ions, moving along the cluster jet. The ions outside the red box correspond to fragments exploded from clusters.(b) Mass spectra of unexploded (red) and exploded (green) cluster ions selected from the momentum map. Both spectra are normalized to the .

The momentum map of all cluster ions (Figure 3.13a) reveals unexploded cluster ions having momentum aligned with the cluster jet direction, forming a distinct blob. In contrast, ions not aligned with the cluster jet have momenta in all directions, characteristic of Coulomb explosions.

The mass spectrum of ions within the cluster jet (Figure 3.13b) resembles the mass spectrum obtained from the UV ionization experiments, displaying a log-normal distribution for higher masses. Plotting the mass spectrum of the exploding fragments (figure 3.13b), it is evident that they make up the spectral peak for ions with masses between 100 and 300 Cu atoms observed in figure 3.12. Comparing with the native mass distribution retrieved in figure 3.5, the ions with masses between 100 and 300 Cu atoms correspond to the smallest clusters extracted from the PMCS. Considering clusters as agglomerates of primary articles, these exploding fragments are most likely ionized primary particles. The small masses below 100 Cu atoms detected by the spectrometer should then correspond to small and atomic fragments created by the destruction of clusters and primary particles.

By quantifying the number of primary particle fragments at each residence time, it becomes possible to correlate the fragmentation yield with the cluster structure. This relationship is examined through a physical model of fragmentation yield at fixed fluence, as described below.

3.3.3.1 *Primary Particle Fragmentation Model*

Given an agglomerate (cluster) composed of primary particles, each with a radius of r and a fractal dimension of D_f [28], the number of primary particles in the system within a cutoff radius of d_c is given by:

$$N(r_c) = k \left(\frac{d_c}{r} \right)^{D_f} \tag{3.10}$$

When the cutoff radius d_c is equal to the radius of gyration R_g, the equation gives the total number of primary particles making up the cluster.

Energy absorption by fractal aggregates can depend on several factors [52]. For fluffy aggregates ($D_f \leq 2$), the absorption cross section is dominated by the sum of the absorption cross sections of each primary particle making up the agglomerate. The cross section in this case is proportional to the number of primary particles N_p. As the density of the primary particles in the agglomerate increase, the primary particles on the surface absorb the radiation while those behind the surface particles are shadowed, decreasing the total absorption cross-section of the agglomerate. Finally, as the agglomerate becomes opaque, only a portion of primary particles on the agglomerates surface will see the laser, and the cross-section becomes proportional to the surface area of the agglomerate.

For this model, PMCS clusters are assumed to be opaque enough to correspond to geometric optics. Under this approximation, the energy absorbed by the clusters (E_{abs}) on irradiation by the pump laser is dependent on their geometric cross-section A_{geo} as seen by the laser beam. This is related to their radius of gyration R_g as:

$$E_{abs} \propto A_{geo} \propto R_g^2 \tag{3.11}$$

Given the number of primary particles in the agglomerate (N_p), equation 3.11 can be redefined as:

$$E_{abs} \propto N_p^{(2/D_f)} \tag{3.12}$$

The probability of a primary particle dissociating from the cluster agglomerate is inversely proportional to the contact force between individual primary particles. This contact force is dependent on the degree of overlap between the primary particles (sin-

tering) [27].

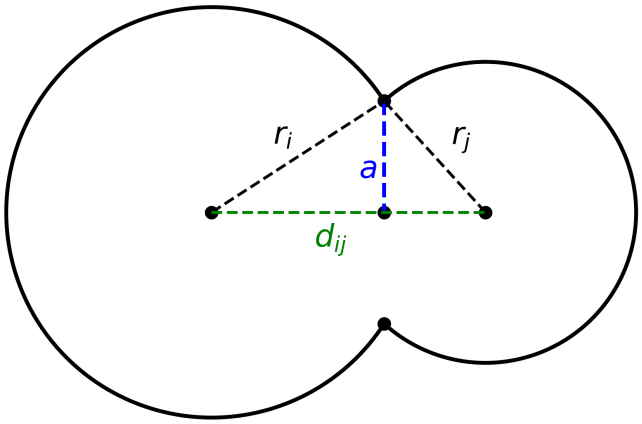

Figure 3.14: Visualization of overlap between two primary particles with radii r_i and r_j at a distance of d_{ij}. a is the radius of the contact area between the two particles at this distance.

Given two primary particles having radii r_i and r_j whose centers of mass are at a distance d_{ij} from each other (Figure 3.14), the degree of overlap between these primary particles $C_{ov\,i,j}$ (henceforth referred to as the overlap factor) [27] is given by:

$$C_{ov\,i,j} = 1 - \frac{d_{ij}}{r_i + r_j} \tag{3.13}$$

Since primary particles are assumed to undergo inelastic collisions as part of the agglomeration process, the force of contact between any two primary particles in a cluster can be defined as proportional to the contact area between them. If the radius of the contact region is a and the distance between the primary particle i and the contact surface is x, a can be estimated as:

$$a^2 = r_i^2 - x^2 \tag{3.14a}$$

$$a^2 = r_j^2 - (d_{ij} - x)^2 \tag{3.14b}$$

$$a^2 = r_i^2 - \frac{(r_i^2 - r_j^2 + d_{ij}^2)^2}{4d^2} \tag{3.14c}$$

Primary particles formed during the microplasma quenching in the PMCS are inherently polydisperse. Since each cluster consists of many such primary particles and is significantly larger than any individual one, the behavior of a cluster can be approximated by that of an agglomerate composed of primary particles with the same average radius. Given the average radius of a primary particle, r_p, and the average center-to-center distance between two primary particles, d_{av}, equation 3.13 can be redefined to express the average overlap factor, C_{ov}, as:

$$C_{ov} = 1 - \frac{d_{av}}{2r_p} \tag{3.15a}$$

$$d_{av} = 2r_p(1 - C_{ov}) \tag{3.15b}$$

Which in turn allows equation 3.14c to be written as:

$$a^2 = r_p^2 - \frac{d_{av}^2}{4} \tag{3.16a}$$

$$a^2 = r_p^2(1 - (1 - C_{ov})^2) \tag{3.16b}$$

$$a^2 = r_p^2 C_{ov}(2 - C_{ov}) \tag{3.16c}$$

The contact force between two primary particles is proportional to a^2 in this model. The energy required to break this contact is an equal force working over a fixed distance, and is therefore

also proportional to a^2.

Applying equation 3.10 with a particle radius of r_p and a cut-off radius of d_{av} gives the number of neighbors a primary particle is attached to, plus itself. Subtracting one from this gives $\left[\left(\frac{d_{av}}{r_p}\right)^{D_f} - 1\right]$, which is the average number of neighbors each primary particle has, or its mean coordination number. The coordination number and the energy to break a contact enable the estimation of the average binding energy (energy required for complete dissociation) of a single primary particle from the cluster:

$$E_b \propto \left[\left(\frac{d_{av}}{r_p}\right)^{D_f} - 1\right] \times C_{ov}(2 - C_{ov}) \tag{3.17a}$$

$$E_b \propto \left[(2(1 - C_{ov}))^{D_f} - 1\right] \times C_{ov}(2 - C_{ov}) \tag{3.17b}$$

The probability of dissociation of a single primary particle during ionization p, assuming a stochastic process, can be defined as:

$$p = 1 - e^{\left(-\frac{E_{abs}}{E_b}\right)} \tag{3.18}$$

For an agglomerate consisting of N_p primary particles, this gives the number of primary particles ejected from the cluster (or the fragmentation yield) N_{frag} as:

$$N_{frag} = N_p \times p \tag{3.19}$$

Given equations 3.12 and 3.17b this can be rewritten as:

$$N_{frag} = Np\left[1 - exp\left(q_c \frac{N_p^{\frac{2}{D_f}}}{\left[(2(1 - C_{ov}))^{D_f} - 1\right] \times C_{ov}(2 - C_{ov})}\right)\right] \tag{3.20}$$

Where q_c is a combination of all the relevant physical constants. This means it is possible to retrieve C_{ov} as a function of t_{res}, given the fragmentation yield $N_{frag}(t_{res})$ along with the fractal dimension $D_f(t_{res})$ (obtained from the mobility analysis), and the total number of primary particles available $N_p(t_{res})$ (obtained from mass characterization) at a given residence time.

3.3.3.2 *Overlap Factor Characterization*

As observed from figure 3.12, irradiation of the clusters with the 400 nm laser creates both primary particle fragment ions as well as smaller ion fragments created from the destruction of clusters and primary particles. The absolute number of primary particle fragment ions N_{pr} is indicative of the total number of dissociated primary particles N_{frag} provided the ratio between N_{pr} and the smaller ion fragments N_{at} (with masses lower than 100 Cu atoms) remains constant across different residence times.

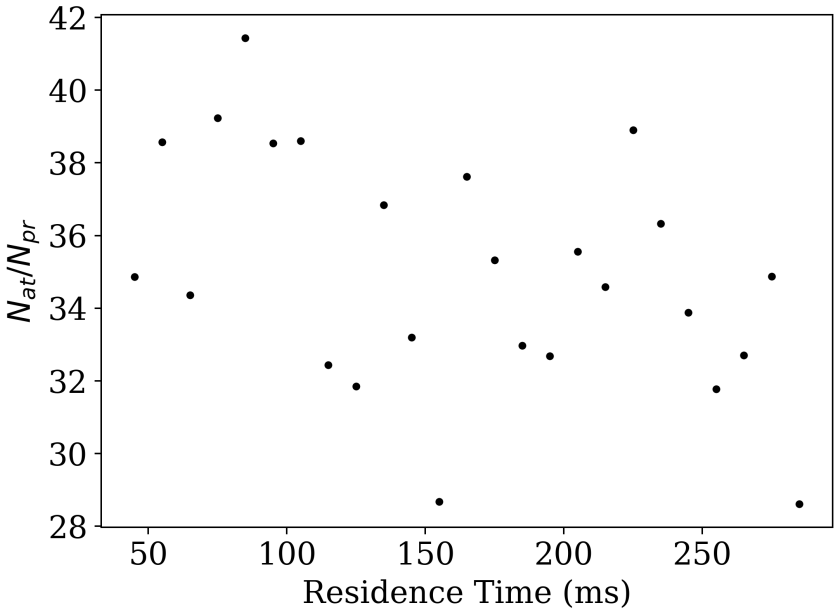

Figure 3.15: Ratio between the number of small fragment ions N_{at} and primary particle fragment ions N_{pr} across different residence times.

As seen in figure 3.15, the ratio is constant. This indicates that a constant fraction of the irradiated clusters further separate into smaller ions and atomic fragments, independent of their growth

conditions. This means that N_{pr} can be treated as equivalent to N_{frag} in the modeling of primary particle dissociation, even if it is not the dominant channel for cluster fragmentation.

N_{frag} can thus be retrieved for each residence time from the number of primary particle ions (Figure 3.16a). The average mass of the primary particles is found to be 190 Cu atoms, retrieved from a log-normal fit of the primary particle masses in the mass spectrum. Given this, the total number of primary particles N_p in a cluster of a given mass can be calculated by dividing the cluster mass by the mass of a single primary particle.

The total N_p available at a given residence time (Figure 3.16b) is then obtained by calculating N_p for each cluster mass, multiplying it by the corresponding yield from the native cluster mass distribution, and integrating over all cluster masses.

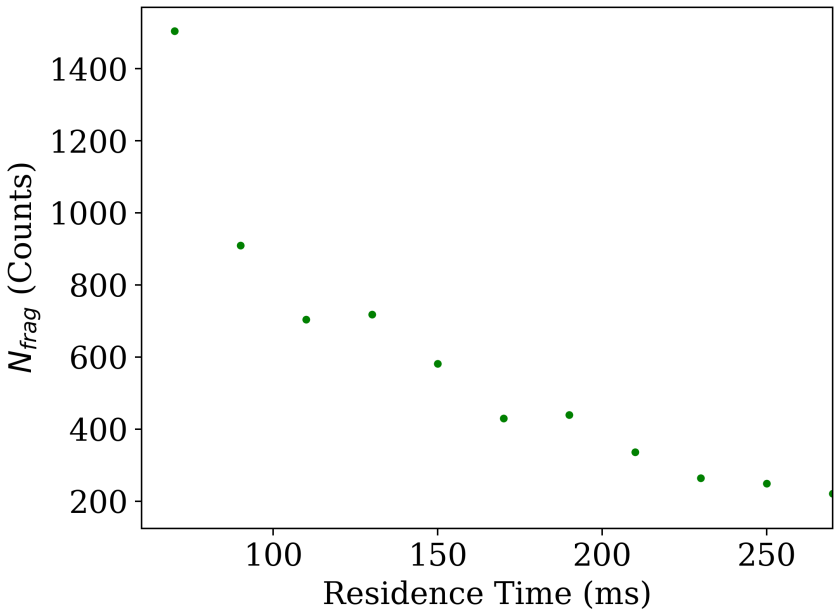

(a)

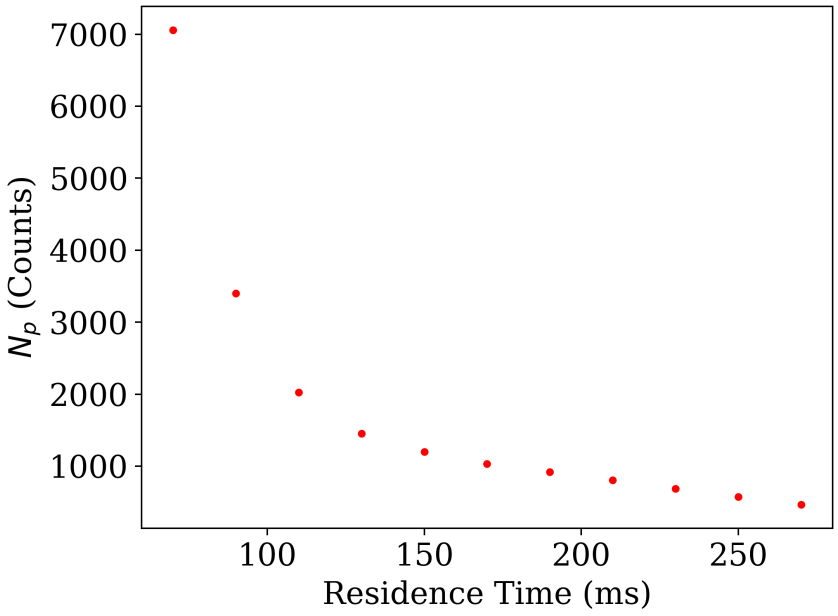

(b)

Figure 3.16: a)Number of primary particle fragment ions detected at different residence times. b) Total number of primary particles available for ionization at different residence times. This number is retrieved by integrating over the native cluster mass distribution,and is not normalized to the residence time dependent cluster yield from the source).

With $D_f(t_{res})$ obtained from the mobility analysis, $N_p(t_{res})$ from the mass characterization and $N_{frag}(t_{res})$ retrieved above,

equation 3.20 is fitted to retrieve C_{ov} for different residence times. This allows characterization of the degree of overlap between primary particles in the clusters for different growth periods.

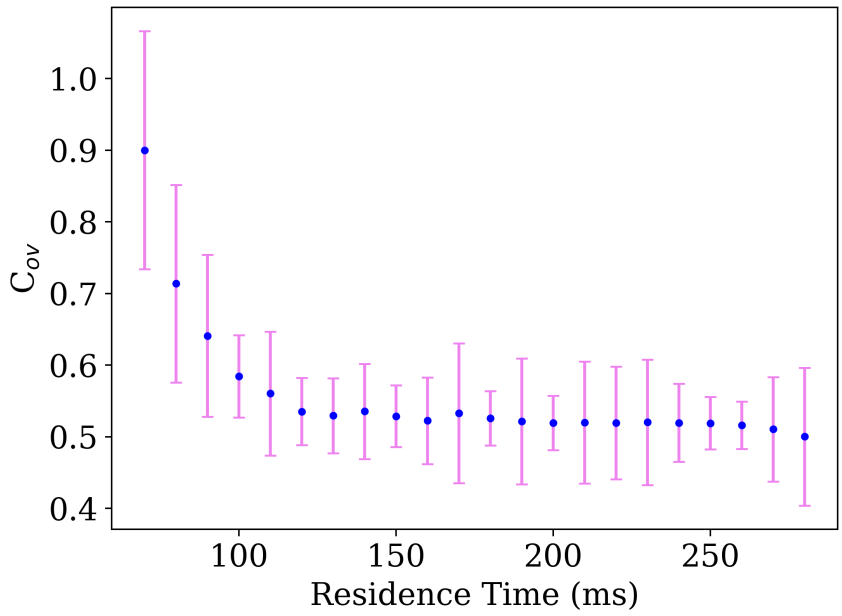

Figure 3.17: Average overlap factor C_{ov} between primary particles in clusters at different residence times, calculated via equation 3.20. The uncertainty of C_{ov} is calculated from the inherited uncertainty in the retrieval of D_f in the mobility analysis.

The value of q_c retrieved from the fit is $1.4 \times 10^{-4} \pm 7.52 \times 10^{-5}$. As seen from figure 3.17, C_{ov} decreases rapidly with residence time, from 0.89 at 70 ms indicating almost complete overlap between primary particles, down to 0.54 at 130 ms. At residence times higher than at 130 ms, C_{ov} decreases much more slowly. This could indicate that clusters extracted soon after the discharge are much more strongly overlapped, as opposed to those extracted later.

3.4 DISCUSSION

Characterization of cluster mass, fractal dimension, and overlap factor as functions of residence time for the detected species across the full duty cycle reveals several notable trends. It is important

to note that the characterization of cluster properties described in this chapter does not address the entire population of clusters extracted from the PMCS. Those members of the population that are not characterized here are explored in chapter 4.

During the first 150 ms, all three parameters exhibit monotonic changes: the average cluster mass increases, while both the fractal dimension and overlap factor decrease.

The high number of primary particles in the PMCS moving at high velocities cavity soon after discharge leads to strong collisions. This can result in near complete overlap between primary particles during agglomeration. This would create denser clusters with high fractal dimensions. As clusters are extracted from the PMCS, the cavity cools, as discussed in the mobility analysis. The cooler temperatures can lead to weaker contact forces between primary particles during agglomeration. This would result in softer clusters having lower fractal dimension.

After 150 ms, both the overlap factor and average mass stabilize, while the fractal dimension shows a slight increase. Given the uncertainty in its determination, this variation may not be significant, suggesting that D_f could remain effectively constant. This behavior, however, contrasts with theoretical predictions of cluster growth, which generally anticipate a continuous decrease in fractal dimension, as well as the overlap factor. Such deviations may arise from different mechanisms, some of which are explained below.

The characterization technique requiring ionization, and unobserved fluence effects emerging from this, could create measurement effects. At long residence times, very large, soft agglomerates are fragmented by very low laser fluences. This can result in a decrease in the average detected cluster mass for these residence times. As the terminal cluster velocity is determined at extraction, fragments would retain the velocity of their parent clusters. This would lead to lower detected velocities for given masses due to the low velocities of fragments of large clusters having the same mass, which lower the average velocity. This can explain the stag-

nating values for fractal dimensions at long residence times in the mobility analysis. Measurement effects, as described above cannot account for the lack of change in the fragmentation probabilities at long residence times however.

Another possible reason for this deviation could be due to the inefficient aerodynamic focusing of larger clusters. As the stagnation pressure in the source decreases at longer residence times, large clusters may not be properly seeded in the carrier gas jet. This can be compounded by the long duty cycle of the PMCS operation and the long focusing stage of the aerodynamic lens. This would imply that the sizes and morphologies of extracted clusters are dominated by effects beyond temperature, contact forces and multiplicative growth.

The selective extraction of clusters at long residence times can explain the stagnation of cluster properties such as average mass, fractal dimension, and overlap factor at long residence times.

This question could be clarified by using lower fluences of higher photon energies for ionization, which may minimize the chances of fluence effects in ion detection. Another avenue would be the characterization of cluster properties through independent experiments that are not susceptible to these errors, which could provide more direct information about cluster size and morphology.

4

STUDY OF GAS-PHASE CLUSTERS VIA SOFT X-RAY SCATTERING WITH FELS

4.1 INTRODUCTION

The size and morphology of cluster nanoparticles, formed through the aggregation of hundreds to thousands of atoms or molecules, strongly influence their physical and chemical properties. Direct imaging methods are essential for characterizing these features. Techniques such as Scanning Electron Microscopy (SEM) and Transmission Electron Microscopy (TEM) have been widely used to study cluster films and deposits [53], but they are unsuitable for clusters in the gas phase. For gas phase clusters, which are typically $\leq$10 nm in size, X-ray scattering provides the necessary spatial resolution[54]. The use of high fluence X-ray Free Electron Lasers (XFELs) with ultrashort pulses further enables time-resolved studies of cluster dynamics[55].

Several X-ray-based techniques can probe cluster morphology, depending on cluster size, scattering cross-section, and FEL parameters such as photon energy, flux, and pulse duration. These include Coherent Diffraction Imaging (CDI) [56], Small-Angle X-ray Scattering (SAXS), and Wide-Angle X-ray Scattering (WAXS) [57]. CDI uses ultrashort XFEL pulses to record diffraction patterns from individual clusters before radiation damage occurs. The resulting far-field diffraction encodes the cluster structure, which is recovered via phase retrieval algorithms. While CDI is powerful, it is limited for PMCS clusters due to their small size and polydispersity. The low number of scattered photons per event makes single-particle imaging challenging.

To overcome these limitations, SAXS is employed here to study cluster structure. Its statistical nature allows the extraction of structural information by averaging data over many shots. For PMCS clusters, SAXS with soft X-rays from FELs is particularly

suitable, as the enhanced scattering cross-section at these photon energies improves signal strength [58]. The SAXS measurements reported here were conducted at the Soft X-ray Small Quantum Systems (SQS) instrument of the European XFEL under Proposal 8055.

4.2 EXPERIMENTAL SETUP

The European XFEL delivers X-ray pulses with extremely high average brilliance, owing to its burst-mode pulse emission pattern [59]. Accelerated electrons are used to generate ultrashort X-ray pulses via magnetic undulators configured to produce Self-Amplified Spontaneous Emission (SASE). Of the three SASE undulators at the European XFEL, SASE 1 and SASE 2 produce hard X-rays, and the SASE 3 undulator produces soft X-rays.

X-ray pulses are organized into trains with durations up to 600 µs and an inter-train repetition rate of 10 Hz. Within a train, pulses are separated by a minimum interval of 220 ns, corresponding to a maximum intra-train repetition rate of 4.5 MHz [60].

For this experiment, the SASE3 undulator was configured to deliver 80 X-ray pulses per train at a photon energy of 1 keV to the SQS instrument [61]. The FEL beam was focused using a Kirkpatrick-Baez (KB) bendable mirror system [62] onto the NQS end station at the $F2$ position of the SQS instrument [61].

The PMCS and expansion chamber were installed on the NQS. The cluster jet was aerodynamically focused to intersect the FEL beam at the center of NQS. The opening time, discharge delay, and cluster focusing conditions remained fixed, as described in Chapter 1, while the trigger system was modified. The PMCS was triggered externally at 3.33 Hz, synchronized to the 10 Hz FEL accelerator.

The NQS includes a time-of-flight (TOF) spectrometer equipped with a delay line detector. Unlike the spectrometer described in Chapter 2, this TOF is optimized for high mass resolution and cannot detect native cluster ions, only their exploding fragments.

Since ionization with FEL does not likely produce native cluster ions anyway, this TOF configuration is sufficient for cluster detection.

X-rays scattered from the clusters are detected using a 1 megapixel pnCCD detector [63]. The detector operates at 10 Hz, averaging the scattered signal from all pulses within a train. It is positioned 50 mm from the cluster jet, with a central gap of 3.2 mm. The direct FEL beam passes through this gap to a downstream beam dump. Stray light is minimized using mechanical slits, maximizing the contrast of the cluster scattering signal (Figure 4.1).

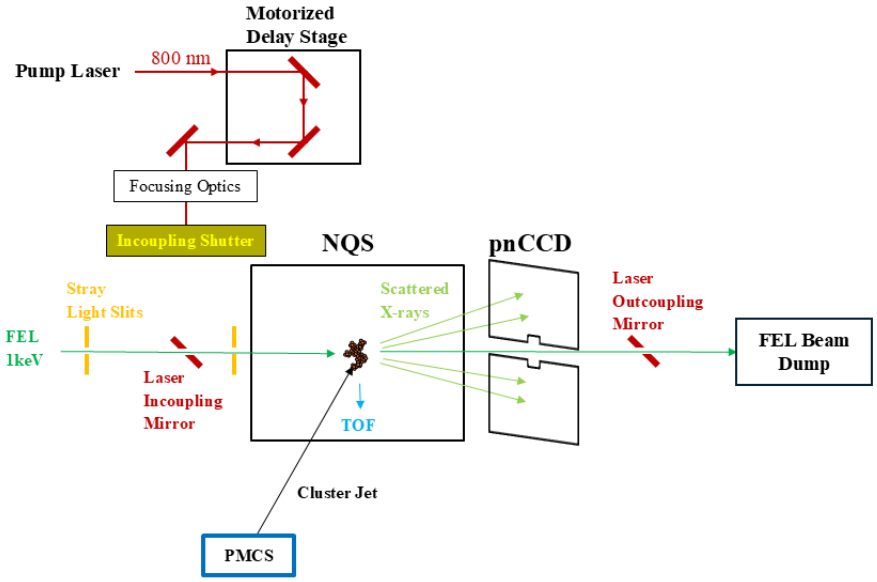

Figure 4.1: Schematic of experimental setup for cluster SAXS. It is possible to incouple an 800 nm pump laser to the FEL for pump-probe measurements, if needed. The incoupling can be achieved via an electronic shutter and a high reflective mirror with a central aperture, allowing the FEL to pass through.

The various data streams from the experiment are acquired and processed via the European XFEL data acquisition system (DAQ) [64]. Each train of the FEL receives a unique integer id, or **train ID**, which is used for indexing in the data files. The pnCCD, which acquires at the rate of 10 Hz has a unique train ID for each shot.

The current signal from the PMCS discharge is also acquired in the DAQ, allowing identification of train IDs where discharge occurs. During the PMCS duty cycle period of 300 ms, the FEL probes three distinct residence times. By varying the delay between the FEL and PMCS trigger, the entire residence time profile can be scanned.

4.3 DATA ANALYSIS

Due to the extreme sample dilution combined with the small scattering cross-section, the polydisperse nature of the sample, and the strong contribution from stray light on the detector, the primary challenge in analyzing the SAXS data is extracting the cluster scattering signal.

4.3.1 *Background Correction*

To separate the signal from the stray light background, correlations between the two experimental data types - time-of-flight (TOF) (Figure 4.2a) and photon scattering (Figure 4.2b) - were analyzed.

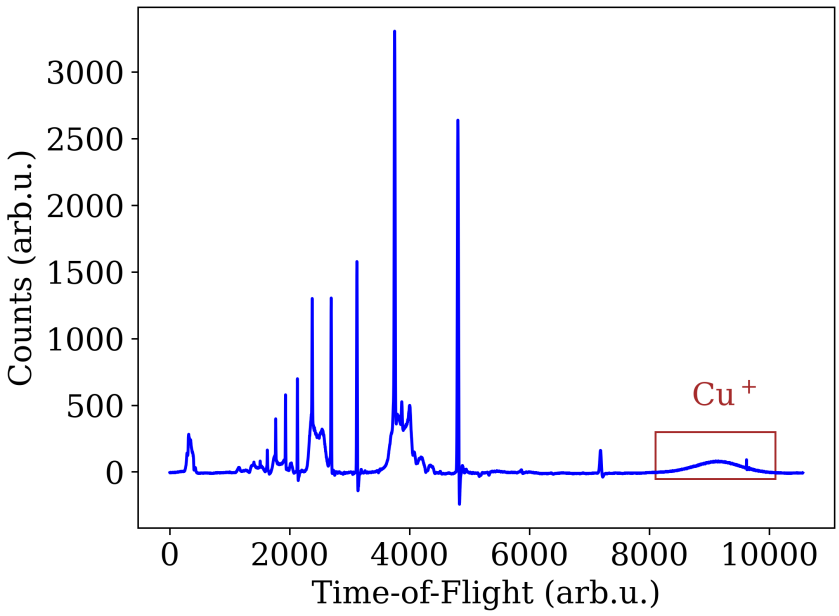

(a)

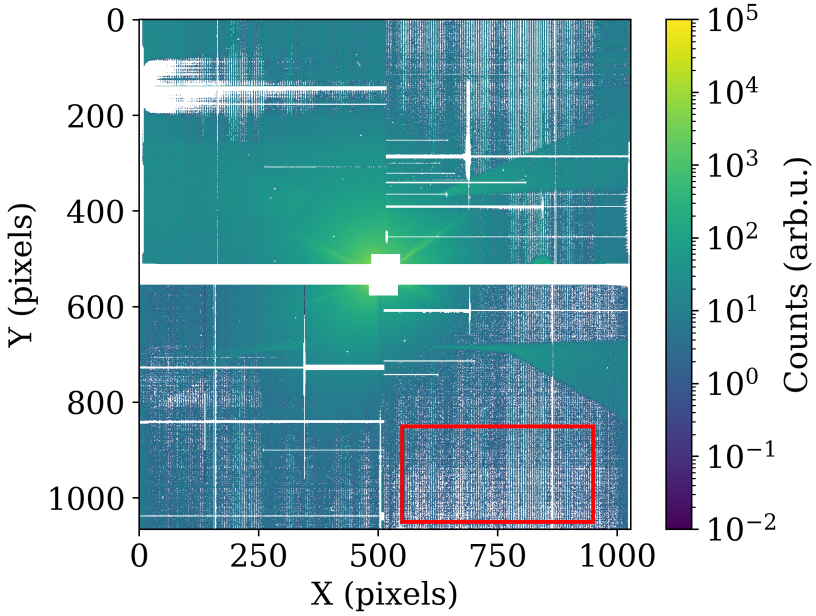

(b)

Figure 4.2: (a) Train averaged TOF spectrum of ions created by interaction between cluster jet and FEL. Cu^+ ion TOF highlighted in brown. (b) pnCCD image of scattered photons with low brightness ROI highlighted in red.

Pixels in a region of interest (ROI), where stray light is minimal, were selected. Summing the intensities of these pixels and comparing them with the integral of the TOF signal from Cu^+ ions reveals a correlation, confirming that the detector captures

scattered light from the clusters (Figure 4.3).

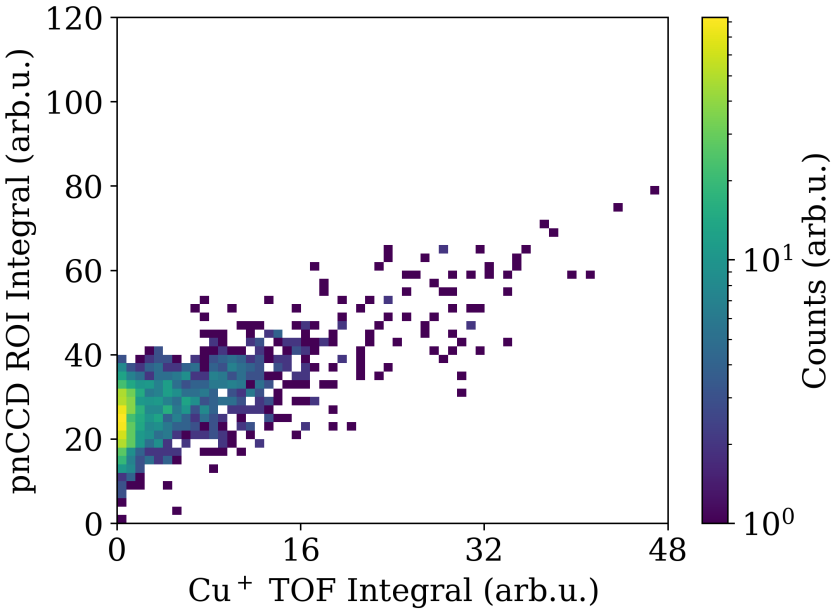

Figure 4.3: 2D histogram of pnCCD signal in low noise ROI and TOF signal of Cu^+. There is a correlation between the TOF signal and the pnCCD signal.

Mapping the pnCCD signal as a function of the FEL–gas injection delay retrieves the PMCS residence time profile. The scattering signal evolves consistently with the source duty cycle (Figure 4.4).

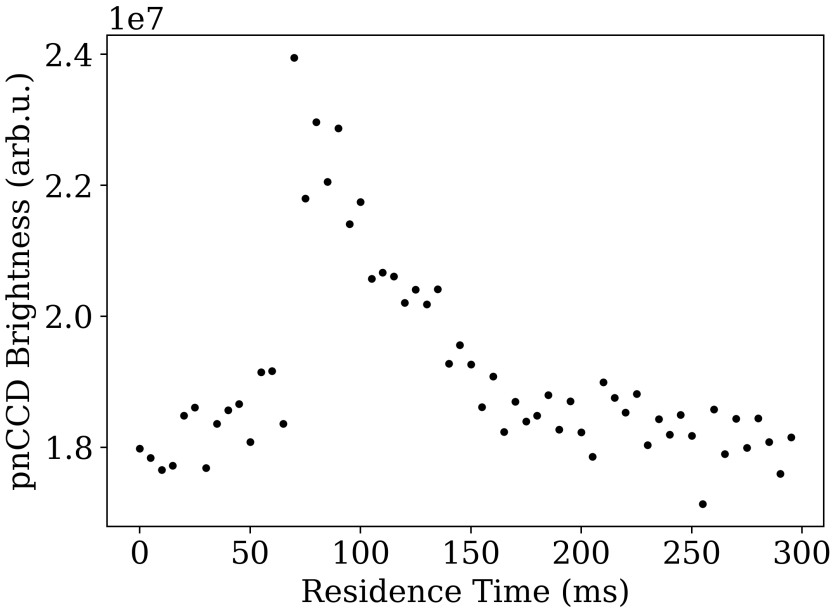

Figure 4.4: Averaged pnCCD signal at low noise ROI for different residence times.

Having established a clear scattering signal, background subtraction is performed. Since the scattering signal correlates with the TOF, this correlation is used to identify signal and background shots at each residence time.

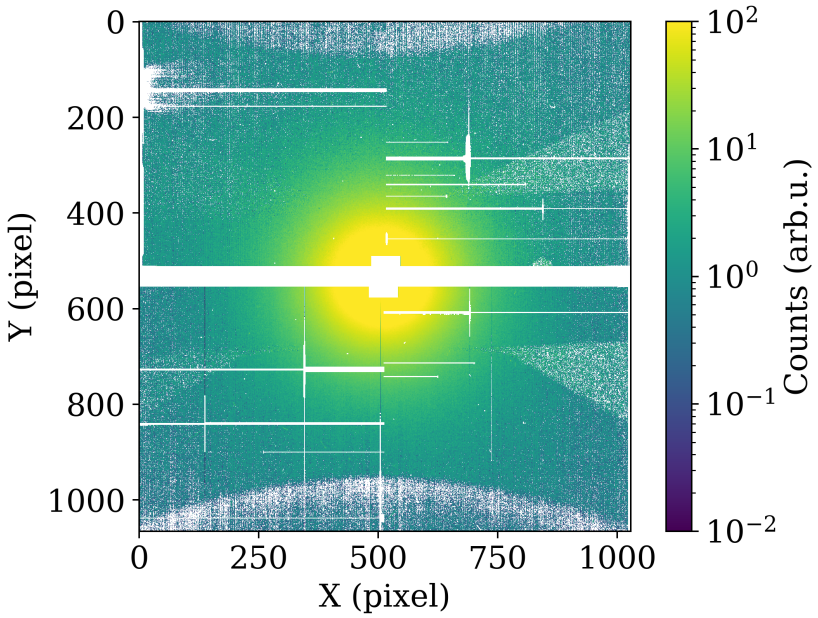

Figure 4.5: Averaged background corrected pnCCD image at residence time of 150 ms

The top 10% of shots based on TOF integral are defined as signal, and the lowest 10% as background. These averages are subtracted to yield the background-corrected scattering pattern at each residence time.

4.3.2 *Radial Profile calculation*

Having extracted the cluster scattering signal, the next step in analyzing the SAXS data is to calculate the radial distribution function, or radial profile. The obtained scattering pattern lacks distinct features such as concentric rings, which complicates the direct identification of the scattering center. Therefore, an optimization procedure was developed to determine the scattering center of the background-corrected data.

To locate the scattering center, a polar transformation of the background-corrected pnCCD image (Figure 4.5) is performed using an initial center guess (Figure 4.6a). A radial region with strong signal and minimal invalid pixels (between 120 and 200 pixels) is selected. The intensity within this region is then integrated along the radial coordinate to obtain the angular profile (Figure 4.6b).

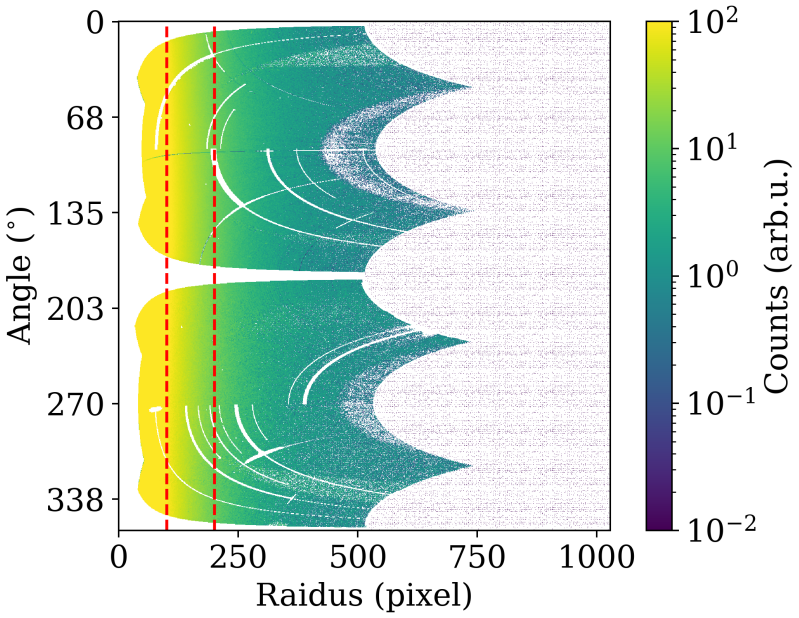

(a)

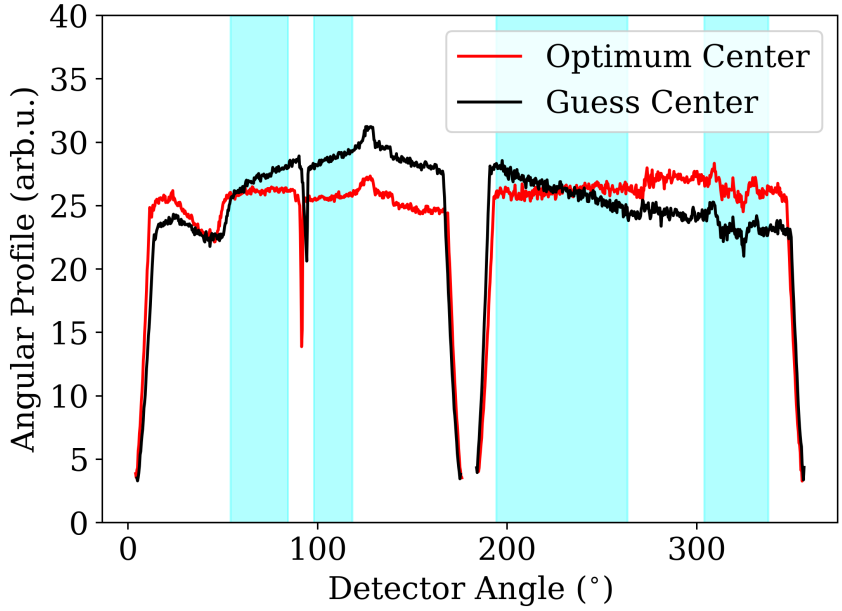

(b)

Figure 4.6: (a) Polar plot of the averaged background-subtracted pnCCD image with an initial center guess. The region between the dashed red lines indicates the radial range used to determine the optimal scattering center. (b) Angular profiles of the pnCCD image using a random center (black) and the optimized center (red). The regions highlighted in blue are the angles used for retrieving the optimized center.

The angular profile has irregularities due to the gap of the pnCCD detector, and possible artifacts from background subtraction. These are neglected in the retrieval of the scattering center. At the optimal scattering center, the angular profile (outside regions with irregularities, highlighted by the light blue shaded areas in Figure 4.6b) is expected to be uniform, meaning that its standard deviation will be minimum. With this standard deviation as a metric and the center as the free parameter, the optimal scattering center for the cluster signal is determined to be (507.4, 533.7) pixels.

The radial profile of the SAXS image is calculated by averaging the scattering intensities of all valid pixels (Figure 4.7). The radial variable is sampled exponentially.

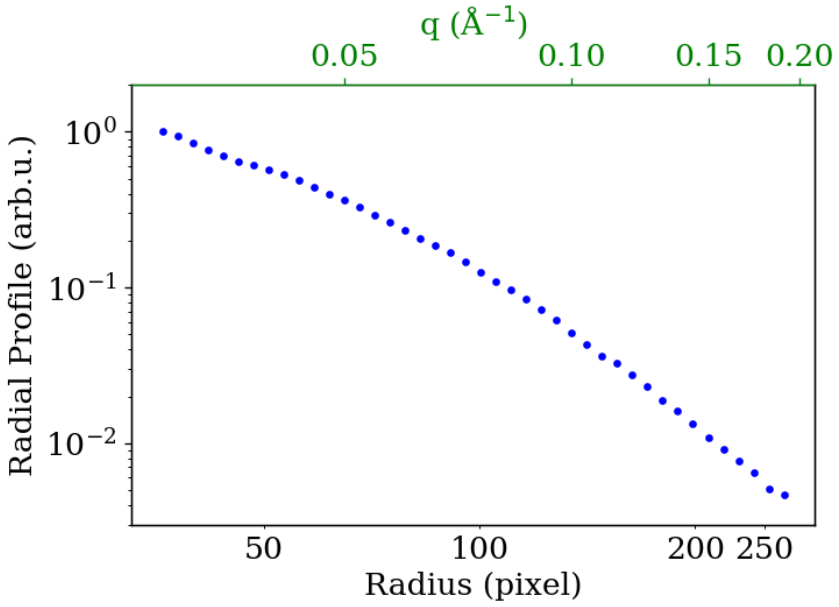

Figure 4.7: Radial profile of SAXS data calculated from optimal center, with radius in pixels and q-value.

4.3.3 *SAXS analysis*

The low-q and high-q scattering regimes in the SAXS radial profile correspond to different structural levels in a sample. The unified exponential/power-law model developed by Beaucage [35] provides a comprehensive framework for describing SAXS data across mul-

tiple structural levels without introducing additional parameters beyond those used in traditional Guinier and power-law analyses. In this framework, each structural level — defined by an overall size and internal substructure — is modeled by a Guinier region that transitions into a power-law regime for high q values (equation 4.1).

$$I(q) = Ge^{\frac{-(qR_g)^2}{3}} + B\left[\frac{\left(erf(\frac{qR_g}{\sqrt{6}})\right)^3}{q}\right]^P \tag{4.1}$$

The Guinier regime captures the average size of a scattering object using an exponential decay, while the power-law region describes how volume or surface features scale with size. When the exponential term of the power-law P is between -3 and -1, it describes the volume fractal dimension D_f of the associated structural level with $P = -D_f$. As discussed in chapter 3, a D_f of 3 describes scattering from spherical objects and lower values corresponding to scattering from softer agglomerates. When P is between -4 and -3, it describes the surface fractal dimension D_s of the associated the structural level with $D_s = 6 + P$. A D_s of 2 describes scattering from a smooth surface, while higher values correspond to scattering from rougher surfaces [65].

By combining these regimes using a unified function, the approach accurately captures overlapping structural features, even when some regions are obscured or poorly resolved due to the instrument's limitations.

Additionally, the unified model accounts for structural limits to the power-law regimes, introducing corrections at both the low-q and high-q ends to reflect the finite size and internal granularity of real-world materials. These corrections are achieved by modifying the power-law expressions with exponential cutoffs that incorporate the radius of Gyration R_g, effectively tapering the intensity in regions where the assumed fractal or interfacial behavior no longer applies. This model enables SAXS data to be fitted globally across a broad range of q values, thereby improving resolution and reliability in the characterization of complex, hierarchical materials,

such as fractal aggregates.

For the radial profile retrieved from the cluster SAXS data (Figure 4.6c), at least two structurally distinct levels can be identified. One at high q-values $>0.1\,\text{Å}^{-1}$, and the second at low q values. The radial profile in this case is modeled as a two-level system, each having an associated radius of Gyration and a power law according to equation 4.1. For the high-q region, the radius of Gyration (R_{g1}) and power law (P_1) are obtained from the SAXS radial profile. In contrast, for low-q regions, P_2 can be obtained from the profile, and R_{g2} is outside the detection range. In this case, the contribution of R_{g2} in the unified fit is neglected by artificially setting it to a high value ($1.9\,\mu\text{m}$). The unified model in this case approximates to a power-law model for the 2^{nd} level. This two structural level model is used to fit the SAXS radial profiles at each residence time.

4.4 RESULTS

The two-level unified model is applied to fit the SAXS radial profiles of the clusters. As shown in Figure 4.8, the model provides an excellent agreement with the experimental data. The fit was found to agree well for all residence times. Fitting the radial profiles at each residence time allows the retrieval of three physical parameters, R_g giving the average size of the scattering clusters, and P_1 and P_2 describing the volume or surface fractal dimensions of the associated levels.

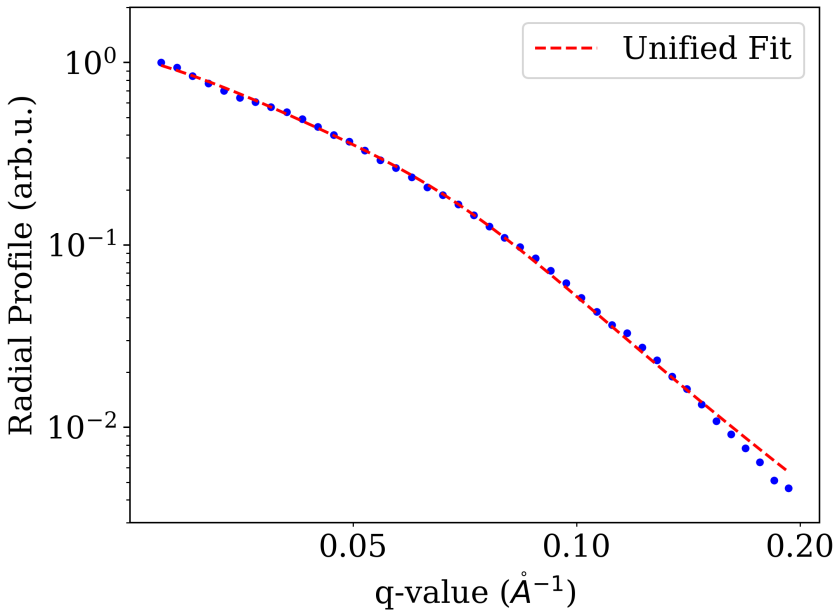

Figure 4.8: Radial profile of SAXS data at 95 ms residence time with unified model fit.

The average radius of gyration of the scattering clusters observed by the FEL, R_g, is approximately 50 Å (Figure 4.9). Only minor variations in R_g are observed with residence time, unlike the broad range of masses observed from the cluster mass spectrum.

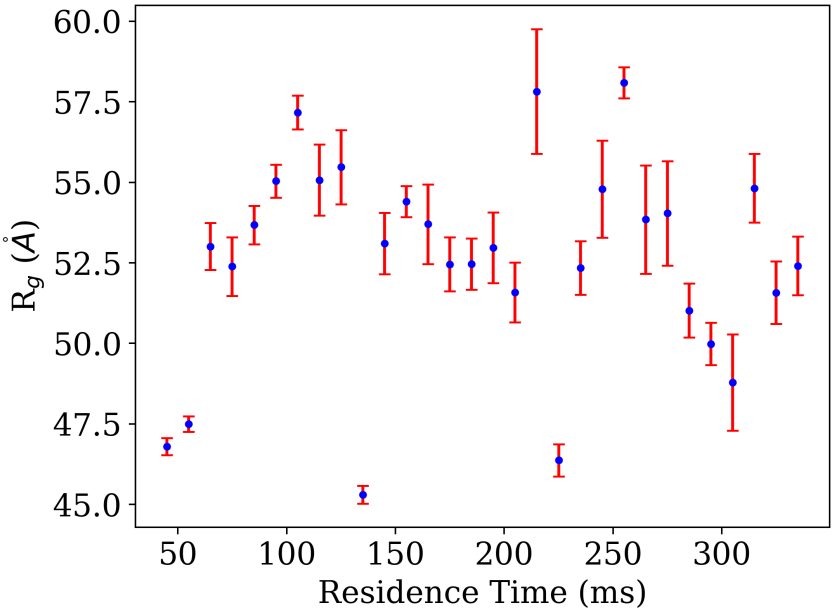

Figure 4.9: Average radius of clusters probed by the XFEL at different residence times R_g.

PMCS clusters can be modeled as agglomerates of primary particles, assumed to be dense spheres containing 190 atoms (as discussed in Chapter 3). A cluster with a radius of gyration $R_g \approx 50$ Å and an average fractal dimension $D_f = 2.3$, (retrieved from the mobility analysis in chapter 3) composed of such primary particles, corresponds to a mass of $\geq 10^4$ Cu atoms (calculated using Equation 3.10).

This indicates that the clusters probed by SAXS are the largest of those detected in the mass spectrum presented in Chapter 3.

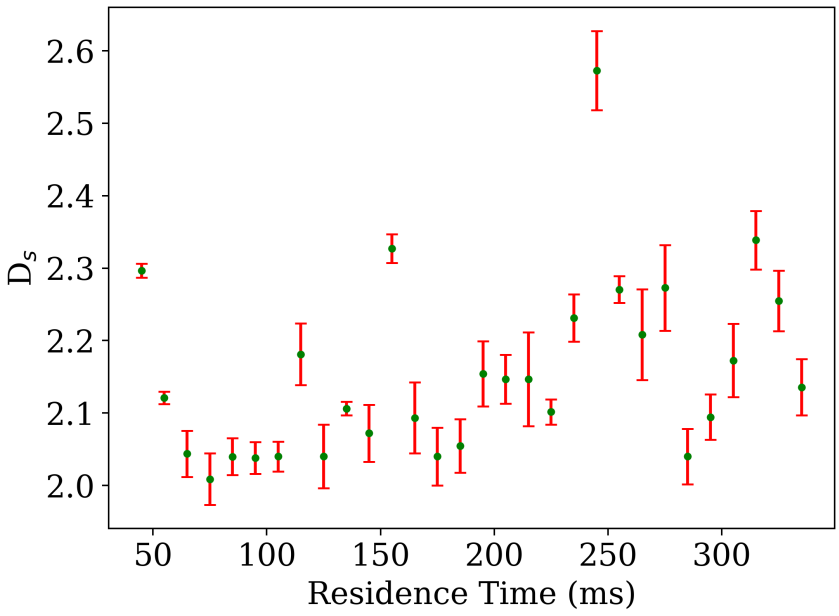

(a)

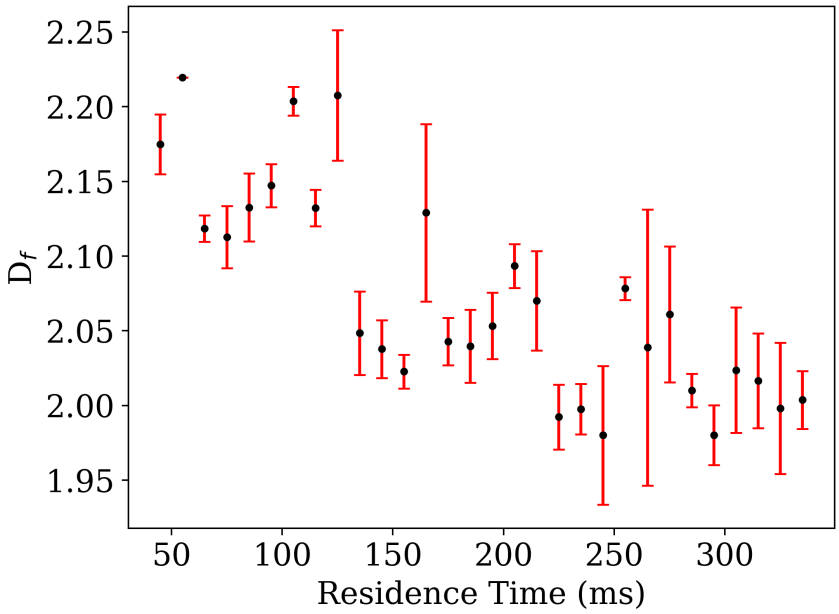

(b)

Figure 4.10: (a) Plot of surface fractal dimension D_s of the clusters probed by FEL, obtained from fitting parameter P_1 at each residence time. (b) Plot of volume fractal dimension D_f of the probed super-agglomerate clusters, obtained from fitting parameter P_2 at each residence time.

The values of P_1 retrieved from the unified fit is between -3 and -4. P_1 thus likely describes the surface fractal dimension D_s of the large clusters. Mapping D_s for different residence times reveals

an increasing trend from 2.05 to 2.3 (Figure 4.10a). According to this trend, the clusters extracted at low residence times have a smooth surface, when probed by the FEL. The clusters extracted later have surfaces with increasing roughness.

Plotting P_2 for different residence times reveals an increasing trend from approximately -2.3 to -2.0. $-P_2$ thus retrieves the volume fractal dimension D_f of systems formed by the agglomeration of the large clusters in the first structural level (Figure 4.10b). These large systems are henceforth referred to as super-agglomerates. The D_f values of the super-agglomerates lie within the same range as the fractal dimensions derived from the mobility analysis; however, their evolution with residence time follows a different trend, This deviation is could be due to the different properties of the super-agglomerates compared to the clusters described in chapter 3.

4.5 DISCUSSION

The results of the SAXS analysis demonstrate its effectiveness in characterizing cluster morphologies in the gas phase, despite the challenges posed by small particle sizes and low sample concentrations.

The increasing trend of the surface fractal dimension D_s indicates that the probed large clusters have surfaces which are rougher at longer residence times. As the clusters seen by the SAXS in the first structural level are likely large, D_s would contain information about the arrangements primary particles making up the surface of these clusters. As D_s is a distinct physical parameter which can evolve independently, it cannot, however give any direct information regarding the volume fractal dimensions of these clusters. Any correlation between the two would require a complete model of cluster growth, which is beyond the scope of this thesis. The data from D_s thus cannot be correlated to the mobility analysis performed in 3.

The D_f values obtained from the SAXS data corresponding to the super-agglomerates exhibit a monotonic decrease from approximately 2.3 to 2.0 over the duration of the duty cycle. In con-

trast, the D_f values derived from the mobility analysis of cluster ions in Chapter 3 decrease up to 150 ms before showing a slight increase thereafter. Since the clusters probed by the two experimental techniques occupy two structural levels, this observation raises two possible interpretations.

The first possibility is that both measurements yield accurate D_f values, with the apparent discrepancy arising from a dependence of the fractal dimension on cluster size. Such a scenario would mean that the average fractal dimension is not size-independent across all extracted clusters and is governed by more than their growth time.

The second possibility is that measurement artifacts affect the D_f values retrieved from the mobility analysis, as discussed in Chapter 3. Since SAXS directly probes cluster morphology, the fractal dimension obtained from this method may be more reliable. This could preserve the size-invariance of D_f, if true.

Resolving the discrepancies in the retrieved fractal dimensions would require SAXS measurements of clusters with an identical PMCS configuration, extending to higher q-values comparable to those probed in the mobility analysis. This would fall within the regime of Wide Angle X-ray Scattering (WAXS) and would necessitate further experiments at FEL facilities.

5

STRUCTURAL DYNAMICS OF GAS PHASE CLUSTERS AFTER IR-LASER EXCITATION

5.1 INTRODUCTION

Fractal aggregates, such as clusters, can be described as kinetically arrested structures formed through the irreversible aggregation of primary particles. These aggregates represent metastable configurations stabilized under conditions of low mobility and irreversible sticking, rather than the energetically favorable compact morphology of a sphere [66, 67]. Within this framework, perturbing the structural state of the clusters is expected to induce a reconfiguration process, and monitoring the ensuing dynamics can reveal their evolution towards a more stable configuration. Such observations provide valuable insight into the mechanisms underlying their initial growth and structural development.

While the dynamics of nanoparticle melting have been extensively studied in the literature [27, 37], small, isolated particles with non-equilibrium structures in the gas phase - such as those produced by the PMCS - remain largely uncharacterized. In this study, structural rearrangement within the clusters was initiated by a temporally stretched, low-fluence laser pulse of low photon energy, which induces thermal excitation in the clusters. This excitation triggers a reconfiguration process that was subsequently probed at various time delays using two complementary techniques: fragmentation studies employing a 400 nm pulsed laser, and Small-Angle X-ray Scattering (SAXS) using soft X-ray FEL radiation (XFEL internal proposal 7237). The experimental observations of cluster dynamics are interpreted using the structural parameters established in the preceding chapters to elucidate the underlying physical processes.

5.2 EXPERIMENTAL DESIGN

The excitation of the clusters was achieved using a temporally stretched (70 fs) infrared (800 nm) laser pulse, focused to a relaxed spot with a diameter of 120 µm. This pulse is hereafter referred to as the pump laser. This provides a controlled energy transfer over a long timescale resembling thermal excitation. The dynamics of the subsequent evolution of cluster properties are probed using experimental methods discussed in previous chapters.

5.2.1 *Small Angle X-ray Scattering*

SAXS data provides direct information regarding the morphological properties of large clusters (as discussed in chapter 4). Combining the pump laser with the FEL beam with delay control, therefore, enables the monitoring of the evolution of cluster morphology as a function of delay between the FEL probe and pump.

The pump in this experiment was the 800 nm mode of the optical pump–probe (PP) laser system at the European XFEL [68] tuned to have a pulse duration of 70 fs. Both the FEL and pump are configured to deliver 50 pulses per train to minimize stray light. The pump beam was coupled into the FEL beamline at the SQS instrument via a right-angled mirror, which features a central aperture to allow unimpeded transmission of the FEL. After interacting with the clusters in the NQS, the pump beam was extracted using a similar right-angled mirror with a central aperture and directed onto a beam block. The pump beamline includes an optical delay stage, which allows precise control of the pump–probe delay (Figure 4.1).

The FEL and pump beams were spatially overlapped using an imaging paddle inserted into the interaction region, which was monitored by a camera. Coarse temporal overlap between the pump and probe was achieved using a photodiode signal by varying the pump delay. Fine temporal overlap was determined from the pump-probe delay dependent ionization signal of N_2^{++} [69] de-

tected in the TOF spectrometer.

For this calibration, the reaction chamber was filled with nitrogen gas while the delay between the IR and x-ray was varied. When the IR arrives later than the x-ray, the X-rays ionize the N_2 molecules into N_2^{++}, which then dissociate into two N^+ ions on pump irradiation. The temporal overlap, or time-zero, was identified as the point at which the N_2^{++} signal intensity in the TOF spectrum increased, with a temporal resolution of approximately 100 fs. This pump–probe configuration enables the characterization of ultrafast structural dynamics, including processes such as cluster melting and dissociation.

For this experiment, SASE3 was configured to deliver 2 keV photons to the NQS. The pnCCD was positioned 105 mm from the interaction point, with a gap of 6.1 mm between its halves. The angular region of the scattering data imaged in this configuration is identical to that in proposal 8055 (chapter 4).

5.2.2 *Ion Spectrometry*

For probing cluster dynamics with ion spectrometry, the experimental setup from chapter 3 was used in conjunction with a two-color mode of the laser with the high-fluence frequency doubled mode (400 nm) as a probe and the fundamental mode as the pump.

For the two-color mode, the frequency doubled laser (probe) was separated from the fundamental (pump) using a dichroic mirror, coated for 99.7% reflection of 400 nm and 95% transmission of 800 nm at a 45° angle of incidence. The pump beamline consists of an optical delay stage for pump-probe delay control and a linear polarizer combined with a polarization dependent beamsplitter for attenuation. The pump was coaxially spatially overlapped with the probe using another 45° dichroic mirror (Figure 4.1).

The spatial overlap between pump and probe was optimized via a paddle introduced into the interaction region of the spectrometer chamber, imaged via a camera. Coarse temporal overlap was retrieved by observing the signal generated from the interaction

of pump and probe beams with a coaxial cable, monitored on an oscilloscope. Fine time overlap was determined using the fragmentation signal from copper clusters. When probe arrives after pump, the yield of cluster fragment ions was increased due to interaction of the probe with irradiated clusters. The implications of this contrast in the dynamics of cluster properties is discussed in the next section. Monitoring the contrast allows retrieval of time-zero.

Time overlap was additionally optimized using a UV laser for cluster ionization and monitoring an increase in the yield of Cu^+ ions after pump irradiation. The contrast in this case was weaker, but allowed the determination of time-zero with a resolution of 300 fs, agreeing with the value retrieved using the 400 nm laser.

This pump-probe setup was used to measure the dynamics of cluster fragmentation over $\approx$ 100 ps after irradiation to learn about cluster structure. The correlation between cluster fragmentation N_{frag} and cluster structural properties was defined using the model described in chapter 3 (equation 3.20).

For the model described by equation 3.20 to be valid, the pump-probe dynamics should not affect the ionization pathways for creation of small fragment ions. As the pump is assumed to excite the clusters without destroying them, cluster fragmentation using the 400 nm laser will likely occur through similar pathways with and without the pump. This means that the model can be sued to describe cluster fragmentation with the pump-probe setup. This would also imply that, at a given residence time, N_p can be estimated as a constant across all pump delays. The evolution of N_{frag} with pump delay would then contain information about the evolutions of D_f as well as C_{ov}.

5.3 RESULTS

5.3.1 *SAXS with pump-probe*

The inclusion of the pump laser introduces complications to the experiment. The stray light on the pnCCD detector due to the pump

laser was much stronger than with only the FEL. The likely cause of this increased background was due to scattered IR light from the downstream section of the experimental setup. The pump laser can scatter off the metal walls of the experiment chamber, creating multiple sources of scattered light, which would increase stray light signal on the detector (Figure 5.1a).

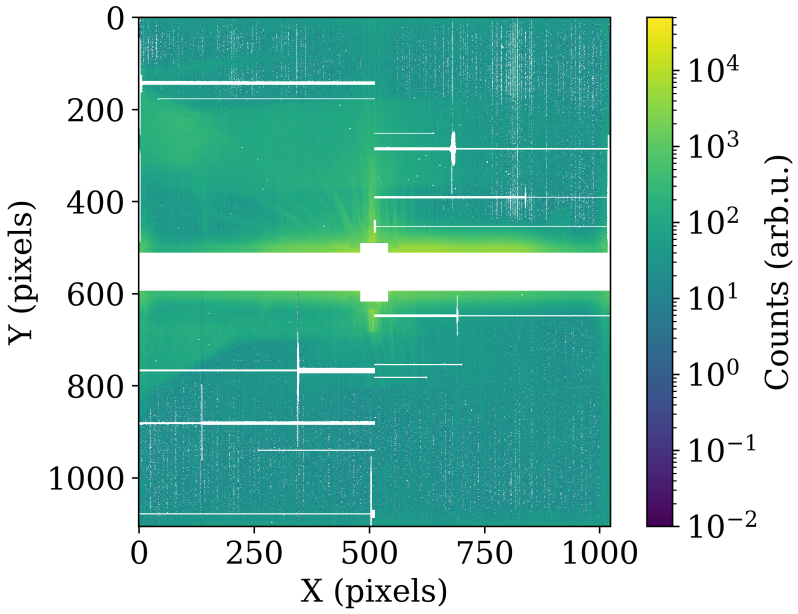

(a)

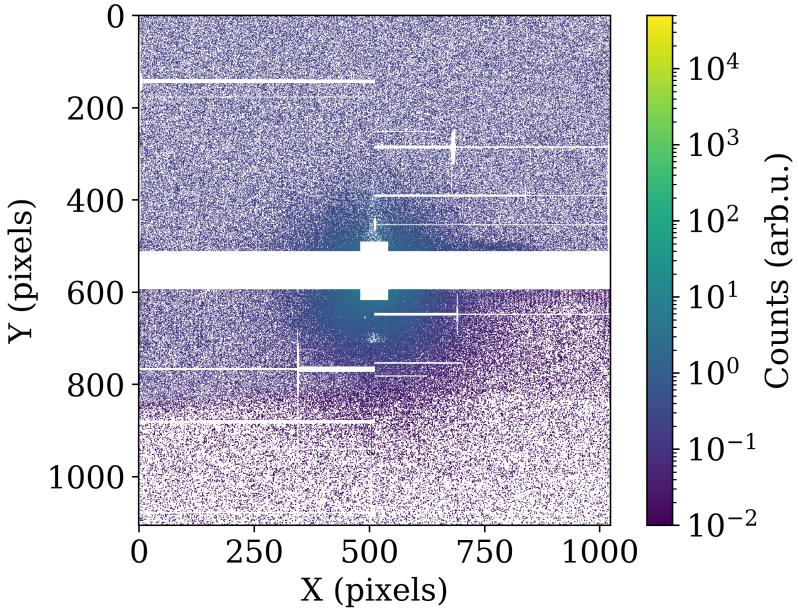

(b)

Figure 5.1: (a) Background pnCCD image with only FEL and pump laser, no clusters. (b)Background corrected pnCCD image showing cluster SAXS in pump-probe configuration. Both images share the same color scale.

The crucial limiting factor in extracting cluster SAXS data in this configuration becomes minimizing the stray light background on the pnCCD. Stray light was minimized using a series of slits together with a low-fluence mode of the pump laser

(2.21×10^6 J/cm^2). Signal and background shots are discriminated based on the yield of Cu^+ on the ion TOF, as described in chapter 4. On background correction, the cluster signal was weak compared to the background image, but distinct (Figure 5.1b).

As a consequence of the weak signal extraction and high levels of stray light from the SAXS data, applying the unified fit model described in Chapter 4 was not feasible, especially at high q-values. The radial profiles from clusters at 150 ms residence time are analyzed by performing a local power-law fit at low q-values ($\leq 0.08\,\text{Å}^{-1}$) (Figure 5.2a) to calculate the evolution of the volume fractal dimension D_f of the super-agglomerates as a function of delay after pump irradiation.

From Figure 5.2b it is clear that D_f increases after pump irradiation, and reaches a maximum value of ≈ 3 around 100 ps. Based on the analysis of cluster SAXS data in chapter 4, this indicates a transformation of cluster morphology from soft agglomerates to dense spheroids.

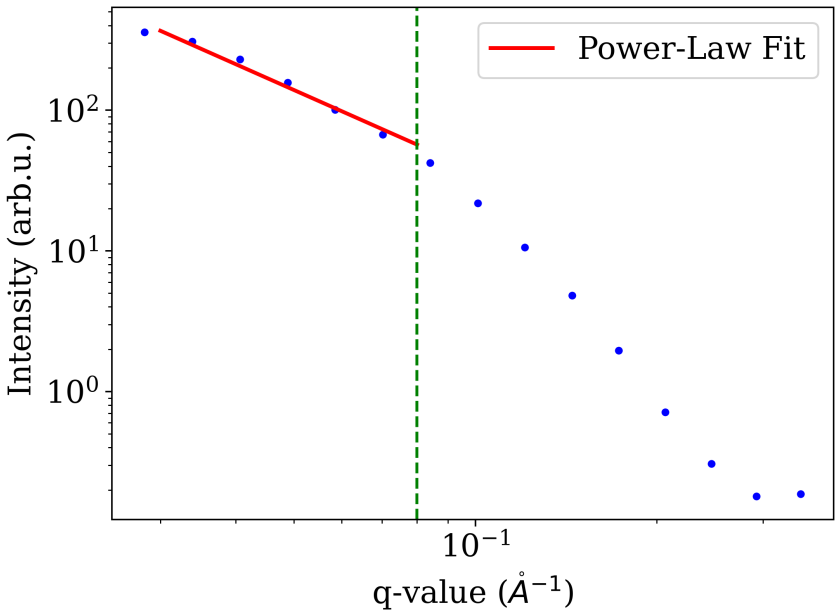

(a)

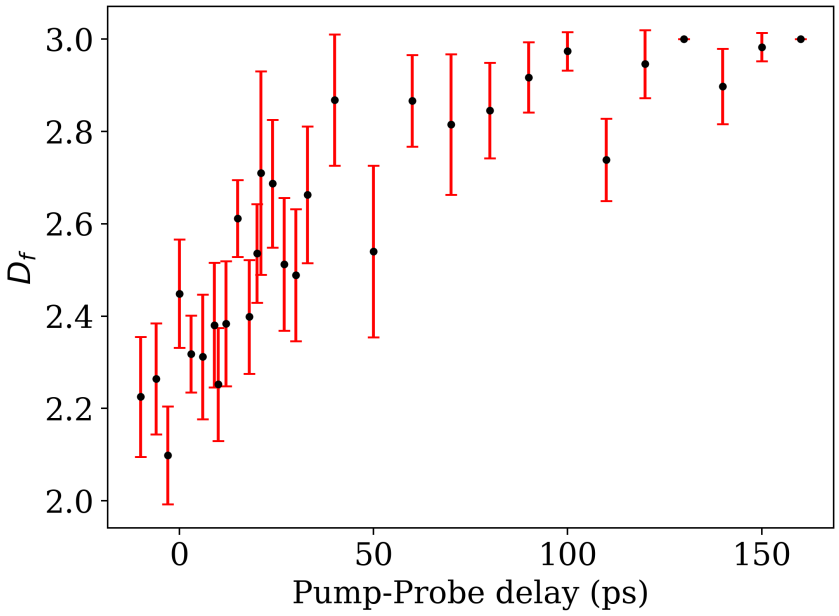

(b)

Figure 5.2: (a) Radial profile of background corrected cluster SAXS image in pump-probe configuration. The volume fractal dimension D_f of the super-agglomerate clusters was obtained via locally fitting the low-q regions denoted by the dashed green line using a power-law fit (red line). (b) Evolution of cluster D_f with pump delay, retrieved from power-law fit of SAXS data at 150 ms residence time (negative values denote pump late). The error of D_f (red error-bar) is obtained from the uncertainty of the fitting parameter.

5.3.2 *Cluster Fragmentation Dynamics*

The correlation between the fragmentation yield N_{frag} and the cluster fractal dimension D_f as well as its binding energy (via the overlap factor C_{ov}) in the model established in chapter 3, makes N_{frag} a suitable observable for characterizing cluster properties. As the N_{frag} is dependent on cluster properties at the moment of ionization, it can be used to track the evolution of cluster properties after pump excitation with the 2-color setup described above. The experiment was conducted with high ($8.8\times10^6\,\mathrm{J/cm^2}$) and low ($2.43\times10^6\,\mathrm{J/cm^2}$) pump fluence to observe the influence of the exciting energy on any observed dynamics between 140 ms and 160 ms residence time.

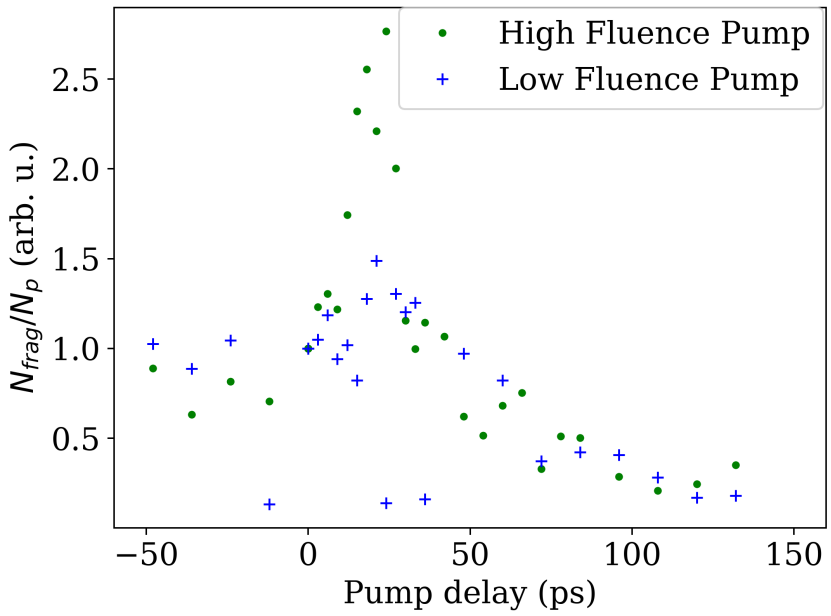

Figure 5.3: Variation in N_{frag}/N_p as a function of delay between pump and probe signals. The green points represent a high-fluence pump, and the blue points represent a low-fluence pump. The values of each set of measurements are normalized such that N_{frag}/N_p at time-zero is 1. This normalized N_{frag}/N_p decreases over a time-scale of 70 ps to 100 ps, compared to its value before pump irradiation.

As illustrated in Figure 5.3, N_{frag}/N_p normalized to the yield at zero pump delay increases after pump irradiation up to 30 ps before decreasing to a lower yield than at time zero by $\approx$ 120 ps. The

decrease in fragmentation combined with the dynamics of D_f observed in the previous section indicates a structural rearrangement of the primary particles in the clusters. The increase in fragmentation at delays ≤ 30 ps is more prominent at high pump fluences.

This trend in cluster fragmentation, when analyzed using the model established in equation 3.20, has two independent variables that influence N_{frag}, namely D_f and C_{ov}. Additionally, the absorbed energy from the pump can modify the binding energies between individual primary particles in the clusters, affecting q_c. As the timescale of electron-phonon coupling is of the order of femtoseconds, the change in q_c can be modeled as a two-level step function, which changes when the pump is early (positive delay). With this model the value od q_c retrieved for pump late measurements of a cluster distribution will be similar for similar probe fluences. Any contrast due to pump fluence will only be seen in the pump early measurements.

The pump-probe SAXS data provides insights into the evolution of the fractal dimension D_f with pump delay, as seen in the previous section. The values of D_f retrieved from the SAXS are likely for super-agglomerate clusters composed of multiple of the clusters detected by the ion spectrometer however, as has been discussed in Chapter 4. Moreover, the trend in retrieved cluster D_f with residence time from mobility analysis (Chapter 3) and cluster SAXS (Chapter 4) diverges for residence times ≥ 160 ms. For residence times $\leq$160 ms, the D_f retrieved from mobility analysis and that retrieved from SAXS differ by an offset of $\approx \pm 0.2$.

To use the D_f values extracted from the pump-probe SAXS measurement in equation 3.20 to retrieve a dynamic evolution of C_{ov} requires certain assumptions. Assuming that the structural rearrangement process initiated by the pump irradiation occurs through identical pathways irrespective of cluster size, the evolution of D_f with pump delay retrieved from the SAXS data can be used to describe the reconfiguration of the clusters detected with ion spectrometry as well. From figure 5.2b, the uncertainty in retrieving D_f from the SAXS data at 150 ms residence time is approximately 0.2, making these values comparable to the fractal

dimensions of the clusters detected via the ion mobility analysis.

With these assumptions, substituting D_f obtained from the SAXS data and q_c modeled as a two-level step function before and after irradiation, equation 3.20 can be used to retrieve C_{ov} and q_c for different pump delays.

Pump Fluence	Late	Early
High	$(1.96 \pm 0.64) \times 10^{-4}$	$(2.00 \pm 0.14) \times 10^{-3}$
Low	$(1.68 \pm 0.29) \times 10^{-4}$	$(1.16 \pm 0.12) \times 10^{-3}$

Table 5.1: Two-level model of fragmentation parameter q_c, for pump late and pump early, retrieved from fitting equation 3.20.

With the two-level model, the fragmentation parameter q_c is seen to increase after pump irradiation (Table 5.1). The values of q_c for pump late are similar to those retrieved with probe only irradiation in chapter 3 for both high and low fluence pump, as expected. The increase in the fragmentation parameter q_c is greater for higher pump fluence. As q_c is inversely proportional to the average binding energy per area between individual primary particles, its increase could mean that irradiation by the pump transfers energy to the vibrational levels of the clusters, lowering the energy required to dissociate primary particles.

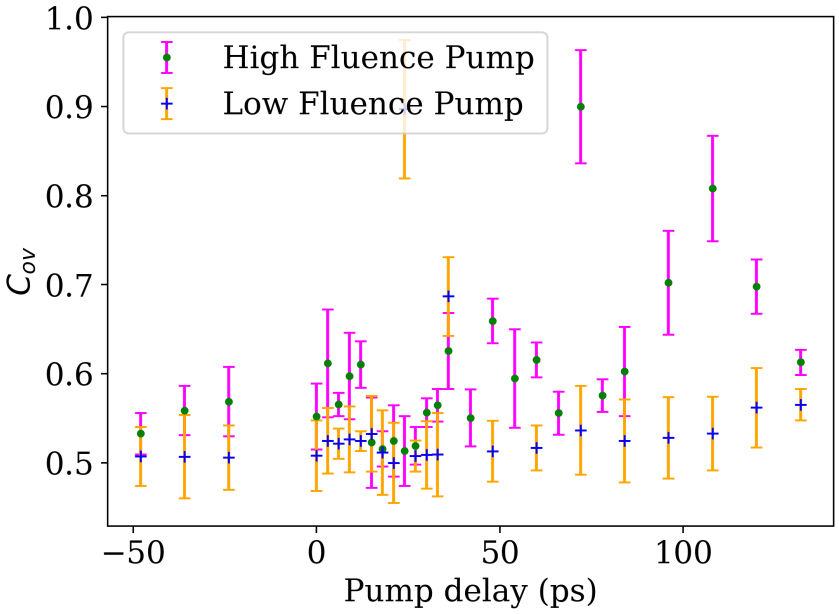

Figure 5.4: Evolution of C_{ov} with time after pump irradiation, calculated using equation 3.20 and D_f. Errors for both plots are calculated from the uncertainty in fitting parameters.

The dynamics of C_{ov} with time after pump irradiation, as seen in figure 5.4, reveal interesting aspects of the structural rearrangement process. For both high and low fluence pumps, C_{ov} first decreases after irradiation up to $\approx 30\,\text{ps}$. This decreasing trend is more pronounced with the high fluence pump. After 30 ps, C_{ov} is observed to increase with pump delay, to values greater than those observed at time-zero by 120 ps. For the high fluence pump, C_{ov} approaches 0.8, and for the low fluence pump, C_{ov} approaches 0.6.

The results of irradiation with high fluence pumps can be interpreted in terms of tightly overlapped clusters, with lower binding energies per primary particle contacts, as compared to irradiation with low fluence pumps. The observed timescales of the dynamics of C_{ov} seem to be similar for both pump fluences.

5.4 DISCUSSION

Cluster dynamics after pump irradiation were studied using two complementary experimental techniques: SAXS and fragmentation

dynamics, as discussed above. With both methods, cluster dynamics were observed over tens of picoseconds. These timescales indicate that the observed processes are too slow to be electronic. The pump irradiation therefore likely transfers energy to the vibrational degrees of freedom of the clusters, triggering processes occurring through thermal pathways. This timescale is in line with melting behavior in gold nanoparticles observed by Plech et. al in 2004 [37].

In both experiments, the observable parameters reach a steady state within 120 ps, implying that the process measured by both methods is the same. The observed dynamics of the parameters were correlated to two independent physical parameters, being the cluster fractal dimension (D_f) and the average overlap factor of primary particles (C_{ov}), which correlate to cluster morphology as well as sintering. Additionally, the retrieval of C_{ov} also reveals information about the influence of pump irradiation on the fragmentation factor q_c which correlates to the average binding energy between primary particles.

After stabilization, at $\approx$ 120 ps, the retrieved D_f and C_{ov} of the clusters both increase compared to their ground state. q_c of the clusters increases after pump irradiation, indicating a lowering of the average primary particle binding energy. This would indicate that after the reconfiguration, the clusters transform into a well-overlapped, spatially dense structure (spheroid), where average contact forces per unit area between primary particles is lower than the unperturbed system. This process is similar to melting. The reconfiguration process yields more overlapped clusters at higher pump fluences.

During the initial 30 ps window however, the fractal dimension (D_f) of the clusters increases, while the overlap factor C_{ov} decreases. Based on the definitions of D_f and C_{ov}, this indicates that the structure of the cluster agglomerate occupies an intermediate state where the primary particles are less overlapped, while being closer spatially, compared to their native state.

These dynamics provide valuable insight into the pathways through which the reconfiguration process could occur. The irradiation of the pump laser transfers energy to the cluster. This energy can weaken the contact forces between individual primary particles, increasing q_c and making their dissociation from the agglomerate easier. The lowered energy required for dissociation causes primary particles to become loosely overlapped. The loosely overlapped primary particles can migrate towards the center of mass of the cluster agglomerate, contacting other primary particles. The migration of primary particles would reduce the geometric cross-section of the agglomerate, and therefore increase its fractal dimension D_f. The loose overlaps between primary particles can explain the lowering of C_{ov} seen in the intermediate states. As the primary particles approach the center of mass, they would be packed densely and overlapped strongly, creating the final dense spheroid. In this model for structural reconfiguration, the greater the energy transferred from the pump to the clusters, the lower the binding energy would become. This would imply that the primary particles in clusters irradiated by a high fluence pump would have more freedom to reconfigure, resulting in a denser, more overlapped final structures compared to clusters irradiated by lower fluence pumps, which agrees with the observations in this thesis.

It is important to emphasize that this interpretation of the structural rearrangement of the clusters in relies on the assumptions and approximations stated in this work, and is merely one pathway by which the observed phenomena may be explained.

While this analysis of experimental data using the developed models can provide valuable insights into the broad trends in cluster dynamics, drawing further conclusions regarding cluster growth and dynamics, specifically the loosely overlapped intermediate states is beyond the scope of this thesis and requires computational simulations, as well as more and improved data.

6

CONCLUSION AND OUTLOOK

This thesis explores several complementary experimental techniques for the study and characterization of PMCS copper clusters in the gas phase over long residence times.

Chapter 2 details the design and commissioning of a prototype ion-electron spectrometer using a novel single detector configuration with static potentials for the gas-phase cluster ions. The primary electrons from the ionization process are focused via a mesh electrode and electrostatic lenses to map their momenta on the detector (VMI). The design focuses ions with transverse momenta onto a concave electrode held at high negative bias, called the ion conversion plate. The high energy ions reaching the conversion plate are converted to secondary electrons. The secondary electrons are focused, allowing mapping of the ion momenta onto the detector. This allows characterization of ions with high transverse momenta as well. The simulations and commissioning tests detailed in chapter 2 indicate that the current prototype of this spectrometer is optimal for effective resolution of the the masses and momenta of cluster ions. The current version of the design is however ineffective at the effective resolution of electrons with low kinetic energies $\leq 5\,\mathrm{eV}$. The prototype spectrometer was employed to effectively study cluster ion properties in chapters 3 and 5.

Chapter 3 describes the characterization of the structural and morphological properties of clusters at different residence times via ion spectrometry. The mass distributions of cluster ions excited by a UV laser was characterized for different laser fluences to retrieve the mass distribution of unfragmented, singly ionized clusters. Accounting for the ionization cross-sections of the clusters allows the retrieval of the native mass distribution of clusters in the PMCS jet.

The cluster mass distribution is characterized for different residence times in the duty cycle. The mass of cluster ions together

with their velocity, extracted from the positional mapping of ions, is used to extract the volume fractal dimension D_f of PMCS clusters via mobility analysis. Retrieving D_f for different residence times allows the morphological characterization of clusters with growth time. The retrieved values of D_f from the mobility analysis is < 3, and are lower at longer residence times.

Ionizing the cluster jet with a visible laser yields a mass spectrum pattern with contribution from exploding fragment with a characteristic mass distribution. The distribution is distinguished by a second peak in the ion mass spectra, and corresponds to the masses of the smallest ions detected in the native mass spectrum. The characteristic peak is thus interpreted as exploding primary particle fragments. The residence time resolved yield of primary particle fragments N_{frag} is correlated to the internal structure of the clusters by modeling the probability of primary particle dissociation upon irradiation by a laser. Together with the mass distribution and cluster fractal dimension D_f, the model can be used to retrieve the average overlap (sintering) factor C_{ov} between primary particles for different residence times, characterizing the internal structure of the clusters. The retrieved values of C_{ov} decrease with residence time before stabilizing.

The observed evolution of cluster fractal dimension D_f and overlap factor C_{ov} with residence time can provide insight into the cluster growth process in the PMCS. Clusters extracted soon after microplasma quenching are dense and strongly overlapped agglomerates of primary particles, implied by their high D_f and C_{ov}. Clusters extracted later have lower values of D_f and C_{ov} both of which stagnate at long residence times. These clusters are likely soft, loosely overlapped agglomerates of primary particles. The stagnation of cluster morphology and structure at long residence times could be due to limitations in aerodynamic focusing, measurement effects or other factors yet to be explored.

The morphology of PMCS clusters is explored more directly in chapter 4. 1 keV X-rays from the European XFEL are used to probe the structure of the clusters via SAXS. The cluster radius of gyration R_g, surface fractal dimension D_s and volume fractal

dimension D_f of large super-agglomerates can be retrieved from the SAXS spectra for different residence times. The extracted values of R_g remains near constant with residence time and are much found to correspond the largest of those detected via ion spectrometry. The surface fractal dimension of the large clusters imaged by SAXS increases with residence time, signaling a change of their surfaces from smooth to rough. The volume fractal dimension D_f of the super-agglomerates retrieved from the SAXS decreases monotonously with residence time. The monotonous decrease of D_f retrieved from cluster SAXS aligns with the agglomeration model of cluster formation, giving softer clusters at longer residence times.

The evolution of cluster volume fractal dimension D_f with residence time retrieved via mobility analysis and via SAXS differs at long residence times. The mismatch between the evolution tends of D_f retrieved from the two experiments may be due any of several factors. One possibility is that the variation of D_f occurs due to the different size ranges of the clusters probed in each experiment. This would imply that the fractal dimension D_f is not size-independent across the full range of cluster masses extracted from the PMCS. Another possibility for the mismatch could be measurements effects which are unaccounted for in either experimental technique.

Chapter 5 describes the dynamic evolution of cluster structural and morphological parameters after irradiation by an IR pump laser. The evolution of D_f with pump delay is retrieved from time resolved SAXS measurements with IR pump and FEL probe. The retrieved D_f values are used together with the values of N_{frag} retrieved from time-resolved ion spectrometry with IR pump and visible probe to model the evolution of C_{ov} with pump delay. The fragmentation parameter q_c is modeled as a two-level step function to account for any variation in the binding energies of the clusters that may occur due to the pump irradiation. q_c is seen to increase after pump irradiation, signaling a likely lowering of the binding energies of primary particles within the clusters. The dynamics of D_f and C_{ov} indicate a structural rearrangement of clusters into

dense spheroids after pump irradiation, similar to melting.

BIBLIOGRAPHY

[1] Uwe Kreibig and Michael Vollmer. *Optical properties of metal clusters*. Vol. 25. Springer Science & Business Media, 2013.

[2] Jean Demuynck, Marie-Madeleine Rohmer, Alain Strich, and Alain Veillard. "Bulk properties or not: The electronic structure of small metal clusters." In: *The Journal of Chemical Physics* 75.7 (Oct. 1981), pp. 3443–3453. ISSN: 0021-9606. DOI: 10.1063/1.442453. URL: https://doi.org/10.1063/1.442453 (visited on 06/04/2025).

[3] Donald M Brunette, Pentti Tengvall, Marcus Textor, and Peter Thomsen. *Titanium in medicine: material science, surface science, engineering, biological responses and medical applications*. Springer, 2001.

[4] Nikolai G Khlebtsov and Lev A Dykman. "Optical properties and biomedical applications of plasmonic nanoparticles." In: *Journal of Quantitative Spectroscopy and Radiative Transfer* 111.1 (2010), pp. 1–35.

[5] Michael A Henderson. "The interaction of water with solid surfaces: fundamental aspects revisited." In: *Surface Science Reports* 46.1-8 (2002), pp. 1–308.

[6] G Schmid. "Chemical synthesis of large metal clusters and their properties." In: *Nanostructured materials* 6.1-4 (1995), pp. 15–24.

[7] Y-L Li, Y Liang, K-S Xiao, F Zheng, and Z-Q Hu. "Synthesis and characterization of ultrafine Si powders from laser induced SiH4 gas reactions." In: *Nanostructured materials* 5.1 (1995), pp. 1–9.

[8] E Barborini, P Piseri, and P Milani. "A pulsed microplasma source of high intensity supersonic carbon cluster beams." In: *Journal of Physics D: Applied Physics* 32.21 (1999), p. L105. DOI: 10.1088/0022-3727/32/21/102. URL: https://dx.doi.org/10.1088/0022-3727/32/21/102.

[9] Bruno Pascucci, Guadalupe Sol Otero, Patricia Gabriela Belelli, F Illas, and Maria Marta Branda. "Comparative density functional theory based study of the reactivity of Cu, Ag, and Au nanoparticles and of (111) surfaces toward CO oxidation and NO2 reduction." In: *Journal of molecular modeling* 20.9 (2014), p. 2448.

[10] Daniel A. Rehn, John M. Wills, Torey E. Battelle, and Ann E. Mattsson. "Dirac's equation and its implications for density functional theory based calculations of materials containing heavy elements." In: *Phys. Rev. B* 101 (8 2020), p. 085114. DOI: 10.1103/PhysRevB.101.085114. URL: https://link.aps.org/doi/10.1103/PhysRevB.101.085114.

[11] Michael Dolg and Xiaoyan Cao. "Relativistic Pseudopotentials: Their Development and Scope of Applications." In: *Chemical Reviews* 112.1 (2012). PMID: 21913696, pp. 403–480. DOI: 10.1021/cr2001383. eprint: https://doi.org/10.1021/cr2001383. URL: https://doi.org/10.1021/cr2001383.

[12] J. S. Wark et al. *Femtosecond temperature measurements of laser-shocked copper deduced from the intensity of the x-ray thermal diffuse scattering*. 2025. arXiv: 2501.02940 [cond-mat.mtrl-sci]. URL: https://arxiv.org/abs/2501.02940.

[13] Xiliang Luo, Aoife Morrin, Anthony J Killard, and Malcolm R Smyth. "Application of nanoparticles in electrochemical sensors and biosensors." In: *Electroanalysis: An International Journal Devoted to Fundamental and Practical Aspects of Electroanalysis* 18.4 (2006), pp. 319–326.

[14] Laura Tamayo, Manuel Azócar, Marcelo Kogan, Ana Riveros, and Maritza Páez. "Copper-polymer nanocomposites: An excellent and cost-effective biocide for use on antibacterial surfaces." In: *Materials Science and Engineering: C* 69 (2016), pp. 1391–1409.

[15] Sinian Yang, Yuting Li, Hongxia Du, Yuqiu Liu, Yanhong Xiang, Lizhi Xiong, Xianming Wu, and Xianwen Wu. "Copper nanoparticle-modified carbon nanofiber for seeded zinc deposition enables stable Zn metal anode." In: *ACS Sustainable Chemistry & Engineering* 10.38 (2022), pp. 12630–12641.

[16] Chenhuinan Wei and Qiming Liu. "Shape-, size-, and density-tunable synthesis and optical properties of copper nanoparticles." In: *CrystEngComm* 19.24 (2017), pp. 3254–3262.

[17] Sang Soo Kim and Gilbert D Stein. "Creation and structure study of vacuum isolated clusters of argon, krypton, and xenon." In: *Journal of Colloid and Interface Science* 87.1 (1982), pp. 180–203.

[18] HR Siekmann, Ch Lüder, J Faehrmann, HO Lutz, and KH Meiwes-Broer. "The pulsed arc cluster ion source (PACIS)." In: *Zeitschrift für Physik D Atoms, Molecules and Clusters* 20 (1991), pp. 417–420.

[19] Maxim Tchaplyguine, Serguei Peredkov, Håkan Svensson, Joachim Schulz, Gunnar Öhrwall, Marcus Lundwall, Torbjörn Rander, Andreas Lindblad, Henrik Bergersen, Svante Svensson, et al. "Magnetron-based source of neutral metal vapors for photoelectron spectroscopy." In: *Review of scientific instruments* 77.3 (2006).

[20] F Di Fonzo, A Gidwani, MH Fan, D Neumann, DI Iordanoglou, JVR Heberlein, PH McMurry, SL Girshick, N Tymiak, WW Gerberich, et al. "Focused nanoparticle-beam deposition of patterned microstructures." In: *Applied Physics Letters* 77.6 (2000), pp. 910–912.

[21] Peng Liu, Paul J Ziemann, David B Kittelson, and Peter H McMurry. "Generating particle beams of controlled dimensions and divergence: I. Theory of particle motion in aerodynamic lenses and nozzle expansions." In: *Aerosol Science and Technology* 22.3 (1995), pp. 293–313.

[22] P. Piseri, H. Vahedi Tafreshi, and P. Milani. "Manipulation of nanoparticles in supersonic beams for the production of nanostructured materials." In: *Current Opinion in Solid State and Materials Science* 8.3 (2004), pp. 195–202. ISSN: 1359-0286. DOI: https://doi.org/10.1016/j.cossms.2004.08.002. URL: https://www.sciencedirect.com/science/article/pii/S1359028604000701.

[23] T Mazza, P Piseri, G Bongiorno, L Ravagnan, M Amati, M Devetta, C Lenardi, M Coreno, M de Simone, and P Milani. "Probing the chemical reactivity of free titanium clusters by

x-ray absorption spectroscopy." In: *Applied Physics A* 92.3 (2008), pp. 463–471.

[24] Alessandro D'Elia, SJ Rezvani, Nicola Zema, F Zuccaro, Mattia Fanetti, Blaž Belec, BW Li, CW Zou, Carlo Spezzani, Maurizio Sacchi, et al. "Stoichiometry and disorder influence over electronic structure in nanostructured VOx films." In: *Journal of Nanoparticle Research* 23.1 (2021), p. 33.

[25] P Piseri, T Mazza, G Bongiorno, M Devetta, M Coreno, and P Milani. "CESyRa: A versatile setup for core-level absorption experiments on free metallic clusters using synchrotron radiation." In: *Journal of Electron Spectroscopy and Related Phenomena* 166 (2008), pp. 28–37.

[26] A Schmidt-Ott. "New approaches to in situ characterization of ultrafine agglomerates." In: *Journal of Aerosol Science* 19.5 (1988), pp. 553–563.

[27] Stephen Robinson-Enebeli, Christof Schulz, and Kyle J Daun. "Investigating the absorption properties of metal nanoparticle aggregates during time-resolved laser-induced incandescence." In: *Journal of Quantitative Spectroscopy and Radiative Transfer* 322 (2024), p. 109009.

[28] Paul Meakin. *Fractals, scaling and growth far from equilibrium*. Vol. 5. Cambridge university press, 1998.

[29] Peter A Cundall and Otto DL Strack. "A discrete numerical model for granular assemblies." In: *geotechnique* 29.1 (1979), pp. 47–65.

[30] T Mazza, M Devetta, P Milani, G Bongiorno, M Coreno, and P Piseri. "Accessing the fractal dimension of free clusters in supersonic beams." In: *New Journal of Physics* 13.2 (2011), p. 023009. DOI: 10.1088/1367-2630/13/2/023009. URL: https://dx.doi.org/10.1088/1367-2630/13/2/023009.

[31] André Guinier, Gérard Fournet, Christopher B Walker, and Kenneth L Yudowitch. *Small-angle Scattering of X-rays*. Wiley New York, 1955.

[32] Harry Brumberger. *Modern aspects of small-angle scattering*. Vol. 451. Springer Science & Business Media, 2013.

[33] Bridget Ingham. "X-ray scattering characterisation of nanoparticles." In: *Crystallography Reviews* 21.4 (2015), pp. 229–303.

[34] Ryong-Joon Roe. "Methods of X-ray and neutron scattering in polymer science." In: (2000).

[35] G. Beaucage. "Approximations Leading to a Unified Exponential/Power-Law Approach to Small-Angle Scattering." In: *Journal of Applied Crystallography* 28.6 (1995), pp. 717–728. DOI: 10.1107/S0021889895005292. URL: https://doi.org/10.1107/S0021889895005292.

[36] Jesper Mellenthin, Alain Karma, and Mathis Plapp. "Phase-field crystal study of grain-boundary premelting." In: *Physical Review B—Condensed Matter and Materials Physics* 78.18 (2008), p. 184110.

[37] A Plech, V Kotaidis, S Grésillon, C Dahmen, and G Von Plessen. "Laser-induced heating and melting of gold nanoparticles studied by time-resolved x-ray scattering." In: *Physical Review B—Condensed Matter and Materials Physics* 70.19 (2004), p. 195423.

[38] David W. Chandler and Paul L. Houston. "Two-dimensional imaging of state-selected photodissociation products detected by multiphoton ionization." In: *The Journal of Chemical Physics* 87.2 (July 1987), pp. 1445–1447. ISSN: 0021-9606. DOI: 10.1063/1.453276. URL: https://doi.org/10.1063/1.453276 (visited on 08/12/2024).

[39] André TJB Eppink and David H Parker. "Velocity map imaging of ions and electrons using electrostatic lenses: Application in photoelectron and photofragment ion imaging of molecular oxygen." In: *Review of Scientific Instruments* 68.9 (1997), pp. 3477–3484.

[40] Utuq Ablikim et al. "A coincidence velocity map imaging spectrometer for ions and high-energy electrons to study inner-shell photoionization of gas-phase molecules." In: *Review of Scientific Instruments* 90.5 (May 2019), p. 055103. ISSN: 0034-6748. DOI: 10.1063/1.5093420. URL: https://doi.org/10.1063/1.5093420 (visited on 08/12/2024).

[41] Michael Davino et al. "A plano–convex thick-lens velocity map imaging apparatus for direct, high resolution 3D momentum measurements of photoelectrons with ion time-of-flight coincidence." In: *Review of Scientific Instruments* 94.1 (Jan. 2023), p. 013303. ISSN: 0034-6748. DOI: 10.1063/5.

0129900. URL: https://doi.org/10.1063/5.0129900 (visited on 08/13/2024).

[42] Akitaka Matsuda, Mizuho Fushitani, Chien-Ming Tseng, Yasumasa Hikosaka, John H. D. Eland, and Akiyoshi Hishikawa. "A magnetic-bottle multi-electron-ion coincidence spectrometer." In: *Review of Scientific Instruments* 82.10 (Oct. 2011), p. 103105. ISSN: 0034-6748. DOI: 10.1063/1.3648133. URL: https://doi.org/10.1063/1.3648133 (visited on 08/12/2024).

[43] C. Stefan Lehmann, N. Bhargava Ram, and Maurice H. M. Janssen. "Velocity map photoelectron-photoion coincidence imaging on a single detector." In: *Review of Scientific Instruments* 83.9 (Sept. 2012), p. 093103. ISSN: 0034-6748. DOI: 10.1063/1.4749843. URL: https://doi.org/10.1063/1.4749843 (visited on 08/13/2024).

[44] G. W. Fraser. "The ion detection efficiency of microchannel plates (MCPs)." In: *International Journal of Mass Spectrometry*. Detectors and the Measurement of Mass Spectra 215.1 (Apr. 2002), pp. 13–30. ISSN: 1387-3806. DOI: 10.1016/S1387-3806(01)00553-X. URL: https://www.sciencedirect.com/science/article/pii/S138738060100553X (visited on 08/12/2024).

[45] Cameron J. Dasch. "One-dimensional tomography: a comparison of Abel, onion-peeling, and filtered backprojection methods." EN. In: *Applied Optics* 31.8 (Mar. 1992). Publisher: Optica Publishing Group, pp. 1146–1152. ISSN: 2155-3165. DOI: 10.1364/AO.31.001146. URL: https://opg.optica.org/ao/abstract.cfm?uri=ao-31-8-1146 (visited on 05/15/2025).

[46] Walt A De Heer. "The physics of simple metal clusters: experimental aspects and simple models." In: *Reviews of Modern Physics* 65.3 (1993), p. 611.

[47] Jonathan AD Wattis. "An introduction to mathematical models of coagulation–fragmentation processes: a discrete deterministic mean-field approach." In: *Physica D: Nonlinear Phenomena* 222.1-2 (2006), pp. 1–20.

[48] Andrey Nikolaevich Kolmogorov. "The local structure of turbulence in incompressible viscous fluid for very large Reynolds." In: *Numbers. In Dokl. Akad. Nauk SSSR* 30 (1941), p. 301.

[49] Kari EJ Lehtinen, Robert S Windeler, and Sheldon K Friedlander. "A note on the growth of primary particles in agglomerate structures by coalescence." In: *Journal of colloid and interface science* 182.2 (1996), pp. 606–608.

[50] Abu B Kanu, Prabha Dwivedi, Maggie Tam, Laura Matz, and Herbert H Hill Jr. "Ion mobility–mass spectrometry." In: *Journal of mass spectrometry* 43.1 (2008), pp. 1–22.

[51] Guillaume FLE. *Extending the pump energy range for a pump-probe system using High Harmonics Generation*. 2015.

[52] CM Sorensen. "Light scattering by fractal aggregates: a review." In: *Aerosol Science & Technology* 35.2 (2001), pp. 648–687.

[53] Jingyue Liu. "Scanning transmission electron microscopy and its application to the study of nanoparticles and nanoparticle systems." In: *Microscopy* 54.3 (2005), pp. 251–278.

[54] Henning Zettergren, Alicja Domaracka, Thomas Schlathölter, Paola Bolognesi, Sergio Díaz-Tendero, Marta Łabuda, Sanja Tosic, Sylvain Maclot, Per Johnsson, Amanda Steber, et al. "Roadmap on dynamics of molecules and clusters in the gas phase." In: *The European Physical Journal D* 75.5 (2021), p. 152.

[55] John CH Spence. "Approaches to time-resolved diffraction using an XFEL." In: *Faraday Discussions* 171 (2014), pp. 429–438.

[56] Alessandro Colombo and Daniela Rupp. "Imaging clusters and their dynamics with single-shot coherent diffraction." In: (2023).

[57] Ingo Steinke, M Walther, F Lehmkühler, P Wochner, J Valerio, Reinhard Mager, MA Schroer, S Lee, W Roseker, A Jain, et al. "A liquid jet setup for x-ray scattering experiments on complex liquids at free-electron laser sources." In: *Review of Scientific Instruments* 87.6 (2016).

[58] Kristina Djinović Carugo, John R. Helliwell, Heinrich Stuhrmann, and Manfred S. Weiss. "Softer and soft X-rays in macromolecular crystallography." In: *Journal of Synchrotron Radiation* 12.4 (2005), pp. 410–419. DOI: 10.1107/S0909049504025762. URL: https://doi.org/10.1107/S0909049504025762.

[59] Massimo Altarelli, Reinhard Brinkmann, and Majed Chergui. "The European X-ray free-electron laser. Technical design report." In: (2007).

[60] Winfried Decking, S Abeghyan, P Abramian, A Abramsky, A Aguirre, C Albrecht, P Alou, M Altarelli, P Altmann, K Amyan, et al. "A MHz-repetition-rate hard X-ray free-electron laser driven by a superconducting linear accelerator." In: *Nature photonics* 14.6 (2020), pp. 391–397.

[61] T Mazza, H Zhang, and M Meyer. "Scientific instrument SQS." In: *Tech. Des. Rep., December* (2012), pp. 12–7.

[62] Tommaso Mazza et al. "The beam transport system for the Small Quantum Systems instrument at the European XFEL: optical layout and first commissioning results." In: *Journal of Synchrotron Radiation* 30.2 (2023), pp. 457–467. DOI: 10.1107/S1600577522012085. URL: https://doi.org/10.1107/S1600577522012085.

[63] Markus Kuster, Karim Ahmed, K-E Ballak, Cyril Danilevski, Marko Ekmedžić, Bruno Fernandes, Patrick Gessler, Robert Hartmann, Steffen Hauf, Peter Holl, et al. "The 1-Megapixel pnCCD detector for the Small Quantum Systems Instrument at the European XFEL: system and operation aspects." In: *Synchrotron Radiation* 28.2 (2021), pp. 576–587.

[64] J Malka, S Aplin, D Boukhelef, S Dietrich, K Filippakopoulos, M Gasthuber, et al. "Data management infrastructure for European XFEL." In: *Proceedings of ICALEPCS2023; Geneva, Switzerland: JACoW Publishing* (2024), pp. 952–957.

[65] G. Beaucage. "Small-Angle Scattering from Polymeric Mass Fractals of Arbitrary Mass-Fractal Dimension." In: *Journal of Applied Crystallography* 29.2 (1996), pp. 134–146. DOI: 10.1107/S0021889895011605. URL: https://doi.org/10.1107/S0021889895011605.

[66] T. A. Witten and L. M. Sander. "Diffusion-Limited Aggregation, a Kinetic Critical Phenomenon." In: *Phys. Rev. Lett.* 47 (19 1981), pp. 1400–1403. DOI: 10.1103/PhysRevLett.47.1400. URL: https://link.aps.org/doi/10.1103/PhysRevLett.47.1400.

[67] Paul Meakin. "Diffusion-controlled aggregation on two-dimensional square lattices: Results from a new cluster-cluster aggregation model." In: *Phys. Rev. B* 29 (6 1984), pp. 2930–2942. DOI: 10.1103/PhysRevB.29.2930. URL: https://link.aps.org/doi/10.1103/PhysRevB.29.2930.

[68] M. Pergament et al. "Versatile optical laser system for experiments at the European X-ray free-electron laser facility." In: *Opt. Express* 24.26 (2016), pp. 29349–29359. DOI: 10.1364/OE.24.029349. URL: https://opg.optica.org/oe/abstract.cfm?URI=oe-24-26-29349.

[69] James M. Glownia et al. "Time-resolved pump-probe experiments at the LCLS." In: *Opt. Express* 18.17 (2010), pp. 17620–17630. DOI: 10.1364/OE.18.017620. URL: https://opg.optica.org/oe/abstract.cfm?URI=oe-18-17-17620.

ACKNOWLEDGMENTS

This PhD has been incredibly meaningful and important to me. It has allowed me to grow tremendously, both as researcher and as a human being.
I am very thankful to my supervisor and group leader Dr. Michael Meyer, for giving me the opportunity to experience science at the European XFEL, and for all his guidance and help throughout my doctoral studies.
I express my thanks to my PhD advisor Prof. Dr. Alexander Lichtenstein for his advice and assistance during my PhD journey.
To my co-supervisor and guide Dr. Tommaso Mazza, I am forever grateful for all he has taught me, the skills he has imparted to me and his steadfast support and guidance throughout my PhD.
I would also like to thank my co-supervisor Dr. Beata Ziaja-Motyka for her insight and guidance regarding the theoretical aspects of my PhD work.
I thank Dr. Simon Dold for his invaluable advice and assistance in the times when I felt stuck, and for his friendship.
My thanks to Dr. Terry Mullins, Dr. Dirk Raiser, and Dr. Matthew Robinson for their lessons on laser safety and help with the laser experiments.
I express my thanks to Philipp Schmidt, for his invaluable help with the data acquisition and on-line analysis systems.
I also thank Jacobo Montano, Nils Rennhack and all the technical groups at European XFEL for their crucial roles these experiments, and sharing their expert knowledge.
Special thanks to Dr. Paolo Piseri, for his pioneering work on the PMCS, his insights, and expertise which have helped realize these experiments.
I would also like to thank my collaborators and peers from the University of Milan, Elettra Synchrotron and FERMI FEL for all their assistance.
My thanks to the MIN faculty at the University of Hamburg, for their help with completing the academic requirements of this PhD.
I would like to acknowledge the entire SQS group. Thank you all for your support throughout my PhD Journey, and for making

time for me whenever I needed help.
To all of my fellow PhD students who have toiled alongside me, such as Aswan, Zhangatay, Mohammed, Aljoscha, Rene and many more, I thank you all for your friendship, and for the good times and wish you all the best with your own journeys.
To my family who have loved and supported me, I give my thanks for making me who I am today. I love you all.
Lastly, to my best friend and my wife Ashwathi, who has loved and supported me while finishing her own PhD, who puts up with my antics, and whom I will love forevermore, thank you.

DECLARATION ON OATH

I hereby declare and affirm that this doctoral dissertation, titled "FEL studies of Complex Metal Nanoparticles and their Structural Dynamics " is my own work and that I have not used any aids and sources other than those indicated.

If electronic resources based on generative artificial intelligence (gAI) were used in the course of writing this dissertation, I confirm that my own work was the main and value-adding contribution and that complete documentation of all resources used is available in accordance with good scientific practice. I am responsible for any erroneous or distorted content, incorrect references, violations of data protection and copyright law or plagiarism that may have been generated by the gAI.

December 1, 2025

Sharath Sasikumar